THE UNIVERSITY OF CHICAGO

NOVEL METHODS AND TECHNIQUES TO INVESTIGATE VOLTAGE SENSITIVE PROTEINS

A DISSERTATION SUBMITTED TO

THE FACULTY OF THE DIVISION OF THE BIOLOGICAL SCIENCES

AND THE PRITZKER SCHOOL OF MEDICINE

IN CANDIDACY FOR THE DEGREE OF

DOCTOR OF PHILOSOPHY

COMMITTEE ON NEUROBIOLOGY

BY

ELIZABETH ERIN LAILEI LEE

CHICAGO, ILLINOIS

MARCH 2019

List of Abbreviations

ASAP1 – Accelerated sensor of action potentials 1

ASAP-Y – ASAP1 with a tyrosine mutation at L158

CaV – Voltage-gated calcium channel

Ci-VSD - *Ciona intestinalis* voltage sensitive domain

Ci-VSP – *Ciona intestinalis* voltage sensitive phosphatase

COVC – Cut-open voltage clamp

Cryo-EM – Cryogenic electron microscopy

FRET - Förster resonance energy transfer

fUAA – Fluorescent unnatural amino acids

FV – Fluorescence versus voltage

GECI – Genetically encoded calcium indicator

GEVI – Genetically encoded voltage indicator

GFP – Green fluorescent protein

GV – Conductance versus voltage

KcsA – Prokaryotic potassium channel

Kv – voltage-gated potassium channel

MITF - Melanogenesis associated transcription factor

Nav – Voltage-gated sodium channel

qBBr – Monobromo(trimethylammonio)bimane

QV – Gating charge versus voltage

R1, R2, R3, R4 – The gating charges numbered from the N-terminal to the C-terminal

Sh - Shaker voltage-gated potassium channel

SIK – Salt inducible kinase

S4 – The fourth transmembrane helix in the voltage sensor

TauV – Tau versus voltage

TEV – Two electrode voltage clamp

TIRFM – Total internal reflection microscopy

UAA – Unnatural amino acids

VSD – Voltage sensing domain

VSFP – Voltage sensing fluorescent protein

$V_{1/2}$ – Half-activation voltage

WT – Wild type

List of Figures

List of Tables

Acknowledgements

No one achieves anything alone. There are many people who helped me finish graduate school and I am grateful to each and every one of you.

I would like to thank Pancho Bezanilla for picking me up as a 4th year graduate student who was starting over and letting me try to finish my PhD. I have learned so much about electronics and ion channels and voltage sensors, much more than I ever planned on, and that is exciting. I have had many lovely opportunities because of the training and work I have done in this lab. I am a better scientist because of this lab experience. I will be forever grateful.

I am thankful for Nani Correa for always being supportive and encouraging and always being there for a quick chat.

I would like to thank the Bezanilla lab, old and new and returning faces: Tomoya, Joao, Jeremy, Li, Carlos, Bernardo, Ben, and Wenli for training and listening to my crazy ideas and always having alternate experiments to try. Thank you for being a good science family. And also, many thanks to my committee, Eduardo Perozo, Debby Nelson, and Chris Gomez for lots of advice and helpful suggestions.

I am grateful to those who have helped edit these many words: Aya Pusic, Wenli Dai, Carlos Bassetto, Ben Fosque, and Michael Priest. I would sound even less coherent if not for these kind people and thank you.

I need to thank my work wives: Kathryn Lesko, Wenli Dai, and Aya Pusic for their endless support from both near and far. I would have murdered many more people if it was not for you so thank you for keeping me on task and my temper low.

And to my labs away from lab, the Kraig lab and Lisa Won, the Becker lab with Kelly and Britt, the Roux lab Lydia, Matt, and Shelly: thank you all for letting me visit and listening to

my gripes and worries and crazy plans. Thank you to the Ahern lab for UAA training and opportunities to try your fancy techniques and Danny Infield for taking the time to talk me through it all. Thank you to Paul Strieleman for always having a place for me to TA, which for much of grad school was the highlight of my week. Thank you to Ruth Ann Eatock and Peggy Mason for guidance during my lab transition. Thank you to Eric Schwartz for being an advocate for my teaching aspirations.

To the many friends who I've met during this process, fellow grad students and non-grad students alike, thank you for the support during the fun times and the not so fun times.

And to the friends, who are practically family, Mark Mazzone and Mark Czynski who watched me through this insane process and cheerleaded and listened to the very boring details as to why my experiment failed that time, thank you so much for being there for me.

Of course, I would like to give many thanks and love to my family: Elaine Lee, Gilbert Lee, and Pam Lee. Over these many years of school, thank you for always being here for me and fostering a curiosity about the world around me. I need to especially thank my sister Catherine Lee who sat on the phone with me through many experiments, so I could listen to movies. Shortie was always there to keep me grounded when I got too wound up about experiments not working.

And of course, I need to thank Michael Priest for helping train me and edit things and keep me from writing rambling sentences like this one. I am grateful for all the time and encouragement you gave to me as I transitioned to a new lab and helping me to find my way. Your support and love helped finish up this PhD and kept me sane. Mostly anytime I think of something to write here I tear up so just, thank you for everything. Also on a truly superficial

side note, freckles are very fashionable in 2018 and synthetic melanin injections could provide a way to achieve this chic look (Green, 2018). I attribute my finishing in a timely manner to you.

Table of Contents

Abstract

This dissertation focuses on the development of new methods to understand mechanisms of voltage sensing in voltage sensitive proteins. I improved a genetically encoded voltage indicator and developed methods to decrease endogenous fluorescence in *Xenopus laevis* oocytes. To understand voltage sensor movement, I used a small molecule dye to optically track discrete gating charges and unnatural amino acids to study the importance of charge versus structure of gating charges.

Genetically encoded voltage sensors are molecular tools that allow for an optical read out of changes in voltage. I characterized the genetically encoded voltage sensor, ASAP1. I confirmed that is has large fluorescence signal and fast kinetics in response to changes in voltage. However, in the physiological range we found a plateau in the voltage and corresponding fluorescence response. Using a rational design method, I improved ASAP1 and created ASAP-Y. It has an improved response in the physiological range and can follow action potentials in neurons.

Next, *Xenopus laevis* oocytes have variable endogenous fluorescence. The high endogenous fluorescence of the oocytes interferes with the signal to noise ratio, thus complicating the recording of fluorescence signals from them. However, I developed methods that decreased the endogenous background fluorescence of oocytes, thus improving fluorescence recording conditions. One method relies on injection of a SIK-inhibitor which decreases endogenous fluorescence. The other technique is the injection of synthetic melanin which creates a disc of melanin that decreases endogenous fluorescence. Both of these methods result in better oocyte fluorescence recording conditions.

I also investigated the mechanism of voltage sensor movement. To understand the mechanism of voltage sensing, studies have focused on the gating charges. Directly observing the movement of discrete gating charges previously was difficult to achieve. However, through the use of a small positively charged fluorescent dye monobromo(trimethylammonio)bimane (qBBr), we were able to track the first two gating charges of the voltage sensor. Using cut-open voltage clamp fluorimetry, we determined that the voltage sensing domain has a vertical translocation and rotation across the membrane. Moreover, we determined that the path of activation differs from that of deactivation. Further, we have described the physical basis for the Cole-Moore shift. This phenomenon occurs when the initial conditions of the voltage sensor are hyperpolarized before activation, leading to a lag in ion channel opening. This technique, tryptophan-induced quenching, can be applied to understanding other states of the voltage sensor as well as other voltage sensing domains.

Finally, we utilized unnatural amino acids (UAA) in several projects. We attempted to observe voltage sensor movement at the level of single molecules. We successfully incorporated Cy3 in the Shaker voltage sensor; however, we never achieved single molecule resolution. We tried to label more internal gating charges with fluorescent unnatural amino acids (fUAA); however, these fUAA never incorporated. We did substitute citrulline for arginines in the voltage sensor to determine the importance of shape versus polarity of an amino acid and find that the loss of charge impacts the fourth gating charge most, whereas gating charges one and three are largely unaffected.

Overall, I have employed new methods to understand mechanisms of voltage sensing as well as developed new techniques to improve fluorescence recordings.

Chapter 1 - Introduction

Abstract

Voltage sensitive proteins allow for the communication between neurons, the contractions of muscle, and signaling of intracellular pathways. Voltage-gated proteins are a large and diverse group of complex peptides that include ion channels, phosphatases, transporters, pumps, and G-protein coupled receptors (Agnew et al., 1978; Martinez-Pinna et al., 2004; Murata et al., 2005; Skou, 1957). The excitability of cells such as nerves and cardiac and skeletal muscle is due to the presence of voltage sensitive ion channels in cell membranes. The movement of ions across the membrane through these channels allows for the creation of fast signals. Dysfunction in ion channel operation can result in ataxia, myotonia, and epilepsy (Cannon, 1996; Doyle and Stubbs, 1998; Lerche et al., 2013). The opening and closing of these voltage sensitive ion channels is due to voltage sensor regions within the channels. But how do these sensors monitor changes in voltage? Through the development of many specialized tools, researchers have been able to study mechanisms of voltage sensing in great detail at the biophysical and molecular level.

Ion channel and voltage sensor overview

Ion channels are membrane proteins that form pores and allow for the selective movement of ions through these channels. There are several distinct types: ligand-gated, mechanosensitive, and voltage-gated ion channels (Agnew et al., 1978; Gurdon et al., 1971; Ingber, 1997). Opening of ligand-gated channels is dependent on the presence and binding of a ligand. Mechanosensitive channels open and close in response to changes in force due to membrane deformations or changes in osmotic pressures. In contrast, voltage-gated ion channels open and close in response to changes in the membrane potential. These opening and closing

transitions are on the millisecond timescale, leading to fast signal transduction. This work focuses on the voltage sensitivity of voltage-gated ion channels and other S4-based voltage sensitive proteins.

Each subunit of a voltage-gated ion channel is typically composed of six transmembrane helices; four that create the voltage sensing domain (VSD) and two that form the pore domain (Bezanilla, 2008; Catterall, 2010). Depending on which type of ion channel, the number of identical subunits may vary. A potassium ion channel is a homotetramer whereas sodium and calcium ion channels are monomeric channels containing four homologous sequence repeats, also known as pseudo tetramers.

The VSD's fourth helix (S4) contains periodically spaced positively charged residues (arginines or lysines) (Noda et al., 1984) that detect changes in membrane potential which translates into a movement that opens or closes an ion channel or alters the activity of a

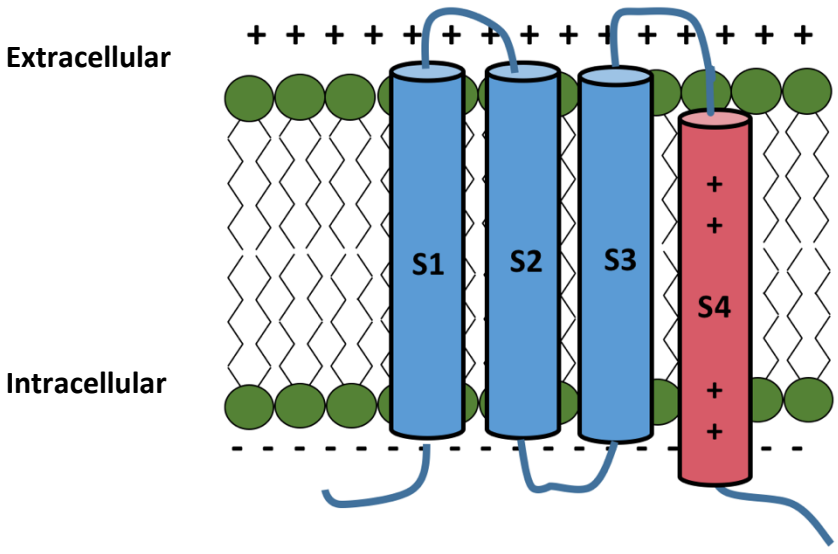

Figure 1.1 - Stereotypic voltage sensor domain structure.
The voltage sensor domain (VSD) within a voltage-sensitive protein consists of four transmembrane helices. Of particular importance is the S4 domain. The VSD shown here is in the resting state as denoted by the downward state of the S4 helix in response to the negative intracellular potential. Note the positive charges in the S4 representing the positively charged amino acids

phosphatase (Aggarwal and MacKinnon, 1996; Armstrong and Bezanilla, 1973; Murata et al., 2005; Okamura et al., 2005; Papazian et al., 1991; Seoh et al., 1996; Stühmer et al., 1989) (Figure 1.1). These charged residues are known as gating charges because they transduce the electric field into the opening and closing of the pore of an ion channel.

The gating charges span the membrane in a transmembrane helix making the upper (most extracellular) charges more solvent accessible than those closer to the inner membrane leaflet when depolarized. This basic structure of S4-based voltage sensors is found in K^+, Na^+, and Ca^{2+} voltage gated channels, proton channels, and voltage sensitive phosphatases (Bezanilla, 2008). The movement of gating charges through a focused electric field (Ahern and Horn, 2005; Bezanilla, 2000; Yang et al., 1996), generated by the membrane potential of a cell, produces a small current, which was named gating current (Armstrong and Bezanilla, 1973). Many studies have focused on understanding the importance of these charges and elucidating the mechanism of voltage sensing using scanning mutagenesis (Chowdhury et al., 2014), pharmacology (Kubota et al., 2017; Ozawa et al., 2015), cross-linking (Campos et al., 2007; Holmgren et al., 1998), and accessibility (Ahern and Horn, 2005; Baker et al., 1998; Larsson et al., 1996; Starace and Bezanilla, 2001; Yang et al., 1996) experiments.

History of studying ion channels

The first observations of biological electrical impulses came from studies of the frog leg. In the 1660s, Jan Swammerdam, a natural scientist, created a neuromuscular preparation from a frog leg (Cobb, 2002). He stimulated the nerve and triggered a muscle contraction. The first discussion of biological electricity is attributed to Luigi Galvani in 1791 when he published his findings using a similar frog preparation. He showed the first demonstration of a propagating action potential. In his preparation, two frog legs with long sciatic nerves still attached were put

in contact with each other. When the nerve from the first frog leg was brought into contact with the nerve or muscle of the second leg, both legs would contract. From this discovery, Galvani postulated a theory of electrically excitable tissue where it exists in a state of "disequilibrium" and is ready to respond to external electrical stimuli. This "animal electricity" theory proposed by Galvani was the beginning of a rich new field of science (Verkhratsky et al., 2006).

While others continued to use the frog neuromuscular preparation, many of the next studies integral to ion channel research were done in the squid giant axon. These neurons had axons that were much larger than other available neurons and had been shown to conduct action potentials (Young, 1938). In the 1930s, Howard J. Curtis and Kenneth S. Cole employed external electrodes to discover that in the squid giant axon, during an action potential, there was a large decrease in membrane impedance (Cole and Curtis, 1939). This was important because the change is in resistance and not capacitance during the action potential (Cole and Curtis, 1939). At about the same time, Alan Hodgkin and Andrew Huxley inserted microelectrodes into the squid giant axon and recorded an action potential (Hodgkin and Huxley, 1939).
Another large experimental step forward occurred with the invention of voltage clamp in 1949 by Cole and Marmont (Cole, 1949; Marmont, 1949). Cole threaded an electrode into the axon allowing for voltage clamp of the entire axon. This new technique allowed the experimenter to control i.e. clamp, the membrane to any desired potential. This led to better characterization of ion permeability as one could simultaneously record current while controlling the membrane potential.

Following this technical development, studies implicated potassium and sodium ions as being the root of the dominant currents in an action potential (Hodgkin and Katz, 1949; Hodgkin et al., 1952; Keynes, 1951). Later, Hodgkin and Huxley performed voltage clamp experiments

with the squid giant axon to investigate the electrical current through the membrane. They combined their experimental data with detailed quantitative modeling to produce a mathematical description of passive ion conductances from the squid giant axon (Hodgkin and Huxley, 1952; Hodgkin et al., 1952). They determined that membrane excitability is due to ion fluxes across the membrane based on their electrochemical gradients. Moreover, they demonstrated that membrane conductance changes were caused by changes in ionic permeability and that these changes were voltage dependent. These findings together laid the ground work for the possibility of some kind of carrier, transporter or pore occurring in the membrane that increases different ions' permeability during an action potential (Hille, 1970).

The field debated what was moderating the voltage-dependent changes in ionic permeability and it was determined that proteins were modulating this permeability. This was shown through enzymatic studies where proteolytic enzymes removed inactivation of sodium conductance (Armstrong and Bezanilla, 1973; Rojas and Armstrong, 1971) and through toxin pharmacology studies where protein binding toxins were observed to block ion conductances (Agnew et al., 1978; Hartshorne and Catterall, 1981; Narahashi et al., 1964)

With the understanding that proteins were the source of these conductances and with pharmacological methods available to delineate the differences in the ionic conductances of sodium and potassium (Armstrong and Binstock, 1965; Narahashi et al., 1964; Tasaki and Hagiwara, 1957), an open question was: what controls the opening and closing of these proteins? Hodgkin and Huxley had postulated that for the conductances to be voltage dependent, there must be charge or a dipole moment within the membrane that responds to changes in voltage (Hodgkin and Huxley, 1952).

Several components were considered when attempting to first measure the movement of

the postulated charge or dipole moment in the membrane. First, all of the ion currents need to be removed. This was done through a combination of solutions with impermeable ions and use of tetrodotoxin (TTX), a blocker of sodium currents. Next, consider the membrane as a capacitor. When a potential is set across the membrane, the capacitor is charged, which results in a large spike in current. Macroscopic ionic currents are larger than this transient and it was possible to resolve them separate from the capacitance. However, if one wanted to resolve much smaller non-linear currents, a method would need to be devised to remove this large spike. This method was the ±P method where, +P pulse were taken in a region where gating charge should move and -P were pulses where the charge does not move but is just the currents of membrane capacitance and leak. Adding these two pulses together should remove the capacitive transient, leaving only the gating current (Bezanilla, 2018).

Using the appropriate solutions and TTX to abolish the sodium current, a low noise recording device, and the ±P method for subtracting the capacitive transient, the first gating currents were recorded from the sodium channel of the squid axon (Armstrong and Bezanilla, 1973). These non-linear recordings were the beginning of many studies to understand the mechanisms of voltage sensing in ion channels.

Next, Neher and Sakmann measured a single acetylcholine channel from a frog skeletal muscle demonstrating the power of the patch clamp technique. The patch clamp allows for the recording of currents from a single ion channel. A recording microelectrode filled with an electrolyte solution was placed on the membrane of the cell with a second ground electrode in the bath. The resulting circuit between the recording electrode and ground electrode can measure currents from the area enclosed by the pipette (Neher and Sakmann, 1976). An improvement to the patch clamp was made with the description of the gigaseal, which was an electrical seal

between the pipette and the membrane with a resistance of gigaohms. This seal can be formed when the pipette surface is kept clean and suction is applied to the pipette itself. This led to improved electrical recordings due to the electrical isolation of the cell membrane patch (Hamill et al., 1981; Neher, 1982; Sigworth and Neher, 1980). The improved patch clamp technique also allowed for whole cell recording of macroscopic currents, which allowed for a wide range of different cell preparations (Findlay, 1984) to be investigated and different parameters such as permeability (Vernino et al., 1992), and selectivity (Hess et al., 1986) to be studied.

Another important breakthrough came with the availability of the full gene sequences for sodium and potassium channels (Noda et al., 1984; Papazian et al., 1987). This knowledge allowed for site-directed mutagenesis, where the genetic manipulation of ion channels allowed for direct alterations to the protein (Papazian et al., 1991).

From there, scientists developed many other configurations of the voltage clamp such as the two electrode voltage clamp for the *Xenopus laevis* oocyte (Baumgartner et al., 1999; Stühmer and Parekh, 1995), and cut-open voltage clamp (Stefani and Bezanilla, 1998), and voltage clamp fluorimetry (Cha and Bezanilla, 1997; Mannuzzu et al., 1996) The cut-open voltage clamp has several advantages such as internal solution control and a faster clamp due to the smaller area that is clamped. This allows for the improved study of faster events such as gating currents. These developments provided the techniques required to investigate the ionic conductances that compose larger electrical signals of the nervous system as well as generate functional data to describe the mechanisms of voltage sensing and ion conductances before a channel structure existed.

In 1998, the first atomic resolution potassium channel structure was determined using X-ray crystallography using bacterial pH sensing channel KcsA (Doyle et al., 1998). Following this

structure, many others have used X-ray crystallography to generate structural models for other channels such as KvAP (Jiang et al., 2003a, 2003b), Kv1.2 (Chen et al., 2010; Long et al., 2005) and NavAP (Zhang et al., 2012). However, due to the lack of true membranes and thus membrane potentials in protein crystals, studying a voltage sensor in a resting state has been a challenge. In some instances mutations have been introduced to try and capture these other states (Li et al., 2014). With recent improvements in cameras and image stabilization algorithms, cryogenic electron microscopy (cryo-EM) has revolutionized the field once again. Cryo-EM has the advantage of not requiring protein crystallization to achieve a structure making it easier to obtain structures of larger complexes (Wang and Wang, 2016). Cryo-EM techniques have produced many new structures including the human Nav1.4-ß1 complex (Pan et al., 2018). However, both X-ray crystallography and cryo-EM only provide snapshots of the ion channel. Thus, it is important to synthesize the structural data with functional data to create a comprehensive understanding of ion channels.

Voltage clamp fluorimetry

Understanding the kinetics of a conformational change in a channel cannot be done solely with electrophysiology. Previous accessibility studies using positively charged adducts such as methanethiosulfonate-ethyltrimethylammonium (MTSET) linked to cysteines placed at gating charges were used to replace the positive charge and characterize discrete gating charges (Ahern and Horn, 2004, 2005; Baker et al., 1998; Larsson et al., 1996). However, these types of adducts cannot be rapidly monitored and thus cannot determine the conformational changes of the VSD's transitions. However, using a fluorescent probe's response to change in the environment, one could now directly study conformational changes of the VSD. The voltage clamp fluorimetry method allows for the simultaneous recording of electrophysiological data as well as an optical

readout of environmental changes around the fluorophore that can be interpreted as conformational changes (Cha and Bezanilla, 1997; Mannuzzu et al., 1996). The data generated allows researchers to directly study conformational changes of the voltage sensor with respect to changes in voltage, instead of relying exclusively on ionic (Timpe et al., 1988) or gating currents (Armstrong and Bezanilla, 1973) as indirect readouts of conformational changes. This technique combines the voltage clamp and accessibility studies where fluorophores are used to investigate local changes in functional protein. When a channel is labeled at a site of interest, the voltage dependent movement of the fluorophore alters the fluorescence emission. This altered emission can be due to the change in environment or proximity to quenching residues (Cha and Bezanilla, 1997). In many instances of voltage clamp fluorimetry, the protein was mutated to have a cysteine at the location of interest and then a dye is conjugated there via a malemide functional group. With the advent of genetically encoded fluorophores, the optical probe is already part of the protein that is to be tracked.

This technique was first implemented in the 1990s to investigate the conformational changes of gating in Shaker (Cha and Bezanilla, 1997; Mannuzzu et al., 1996). Originally implemented with TEV and COVC with *Xenopus laevis* oocytes, other voltage clamp configurations have also adapted the voltage clamp fluorimetry technique. For example, a study using patch clamp with fluorimetry investigated cyclic nucleotide-gated channels (Zheng and Zagotta, 2000). Voltage clamp fluorimetry is a powerful tool for understanding protein conformational changes in real time. However, there can be complications when using traditional dye labeling methods. This includes non-specific background labeling of a dye and residual cysteine locations that greatly increase labeled background fluorescence. When recording fluorescence signals in *Xenopus laevis* oocytes, the endogenous fluorescence of the oocyte

reduces the ability to resolve those signals. To address this issue, I have developed two methods to decrease the oocyte's fluorescence. One uses a salt-inducible kinase (SIK) inhibitor while the other is a direct injection of synthetic melanin to the oocyte. Both of these methods reduce the background fluorescence, improving oocyte fluorescence recording conditions (Chapter 3).

Models of voltage sensor movement

The literature on the VSD describes several competing models of how the VSD moves in response to changes in membrane potential. In the paddle model, part of the S3 and the S4 helices form the 'paddle' (Jiang et al., 2003b). This paddle rests on the inner perimeter of the channel when in the resting state. Upon depolarization the paddle swings, making a large movement through the membrane of approximately 15-28 Å (Jiang et al., 2003a). The sliding helix and helical screw models propose that the main voltage sensor consists of the S4 and has a much smaller movement from the intracellular membrane to the extracellular side, a tilt, and also features a 60° rotation for each turn it makes (Catterall, 1986; Guy and Seetharamulu, 1986; Starace and Bezanilla, 2001; Vargas et al., 2012). Each turn allows a positive gating charge to pair with the next negative charge (Keynes and Elinder, 1999).

Evidence in support of the helical screw model has been demonstrated through site-directed mutagenesis (Grabe et al., 2006), crystallography (Li et al., 2014), accessibility (Tombola et al., 2006), modeling (Lecar et al., 2003), and site-directed fluorimetry voltage clamp in Ci-VSP and Shaker (Cha and Bezanilla, 1997). A significant feature of many VSDs is the hydrophobic plug, a set of hydrophobic residues that form a region that electrically divides the membrane (Lacroix and Bezanilla, 2011; Tao et al., 2010a). The S4 slides through this 'plug' when it moves. In Shaker, residue F290 interacts with the last gating charge, R371, and controls the transfer of this gating charge across the focused electric field (Lacroix and Bezanilla, 2011).

However, these models focus on the secondary structure of the helix; none of them are based solely on the gating charges which are arguably a central part of the VSD's mechanism. The study of conformational changes in the VSD cannot be done with electrophysiology alone, because the electrical changes are not directly correlated to conformational changes. Thus, many studies have made use of voltage clamp fluorimetry to probe conformational changes of the VSD in response to voltage. Thus, an approach to understanding the mechanism of the VSD is to study specific gating charge movement correlated with structural changes via fluorescence. Previous studies of the gating charges that make up the VSD focus on the neutralization of these charges (Aggarwal and MacKinnon, 1996), positively charged adducts which are hard to track (Ahern and Horn, 2004; Baker et al., 1998; Larsson et al., 1996), histidine mutations to control the charge (Starace and Bezanilla, 2001) or the generation of cross-linked mutants, thus making it difficult to trace the exact path of these charges (Campos et al., 2007).

However, through the mutation of gating charges to cysteines and conjugation of a small positively charged dye, we can preserve their positive valence and more accurately track details of the gating charge path. Monobromo(trimethylammonio)bimane (qBBr) is a small dye that can mimic gating charge, whose fluorescence is quenched in the presence of tryptophans. This technique, tryptophan induced quenching (TrIQ) can give more detailed information of an individual gating charge's location in a functioning protein (Mansoor et al., 2002, 2010).

As the mutated and labeled gating charge moves, the dye's interaction with tryptophans will quench with closer proximity and unquench as it moves further away, thus generating an optical measure of conformational changes (Semenova et al., 2009). By tracking both the gating and the fluorescence, we can study a functional protein and relate that function to its structure. These changes can be compiled to determine a path for a VSD (Chapter 4).

Optically tracking voltage

Since the advent of the voltage clamp, scientists have been able to electrically interrogate cells. While these technologies are powerful, a disadvantage is that cells need to be patched individually. This is feasible for a small scale experiment and has been done with up to 8-12 cells simultaneously (Jiang et al., 2013; Perin et al., 2011), but it is impractical when studying neuronal population dynamics. In contrast, an optical read-out of voltage significantly increases throughput. Indeed, calcium imaging using dyes or genetically encoded indicators has been employed to study network activity with great success (Lin and Schnitzer, 2016; Lock et al., 2015). Here I discuss methods that allow for optical tracking of voltage changes.

Voltage sensitive dyes

The first popular method to optically observe changes in voltage were small organic dyes in squid giant axon (Davila et al., 1973). The most successful of these early dyes was merocyanine 540 which had a fluorescence signal of 0.1% when tracking an action potential and has sub-millisecond kinetics (Salzberg et al., 1993). This was much larger than other previously attempted dyes. These dyes were used to monitor single neuron changes (Grinvald and Hildesheim, 2004) as well as larger neuronal populations (Baker et al., 2005). Di-8-ANEPPS, a dye in the in the styryl family, is one of the fastest of the voltage-sensitive dyes (Bedlack et al., 1994) and has a large $\Delta F/F$ of 15% per 100 mV signal (Rohr and Salzberg, 1994). Unfortunately, this dye has a tendency to photobleach, limiting its lifetime use (Pucihar et al., 2009).

To interrogate cells deep within a tissue, some smaller molecular weight dyes when coupled with two-photon excitation allow for deeper brain imaging (Fisher et al., 2008; Kuhn et al., 2008). However, voltage sensitive dyes are not without drawbacks, such as limited specificity in labeling. Moreover, when used in heterogeneous cell populations the lack of specificity results

in the labeling of neuronal and non-neuronal cells alike, complicating the optical signals recorded (Konnerth et al., 1987). Furthermore, many of these dyes are toxic which lead to limited usage in live preparations (Preuss and Stein, 2013). These types of complications led to the development of alternative methods of optically recording voltage.

Genetically encoded voltage indicators

An additional research tool that complements voltage clamp fluorimetry, is genetically encoded voltage indicators (GEVIs). GEVIs can be used to detect changes in membrane potential in cells. Unlike traditional cysteine mutagenesis where there are drawbacks such as the lack of specificity when labeling samples with dye and residual cysteine labeling, GEVIs have reduced non-specific labeling due to the genetic encoding. GEVIs can be expressed specifically in target cell types and compartments. Even still, recording changes in voltage presents unique challenges. This requires not only a significant signal to noise ratio, but also the temporal resolution for this tool needs to be on a sub-millisecond time scale.

There are two main designs for GEVIs; voltage sensing domain-based designs and opsin-based designs. Arch, based on Archaerhodopsin 3, was the first iteration of an opsin-based design. Arch is a modified light-modulated outward proton pump from *Halorubrum sodomense* (Kralj et al., 2011) (Figure 1.2D). Its voltage sensitivity originates from the Schiff base protonation, in which depolarization increases the protonation, leading to an increase in rhodopsin absorption and fluorescence emission. The D95N mutation blocks the pumping of protons, thus preventing a photocurrent, while still allowing for protonation of the Schiff base, keeping it voltage sensitive (Kralj et al., 2011). While Arch has fast kinetics, many of the early opsin-based designs had problems with the amount of laser power needed to observe fluorescence output. The latest versions of the opsin based GEVIs, known as FRET-opsin, use a

combination of genetic encoding and bright fluorescent proteins or photostable dyes. An example of this is Voltron, a rhodopsin (Ace2) fused to a self-labeling tag domain (HaloTag) (Figure 1.2E). The HaloTag can covalently bind a small molecule fluorophore. Membrane depolarization reversibly decreases the fluorescence of the small molecule fluorophore via increased FRET to the rhodopsin domain (Abdelfattah et al., 2018). This allows for specific *in vivo* cell type labeling, and the use of bright photostable dyes.

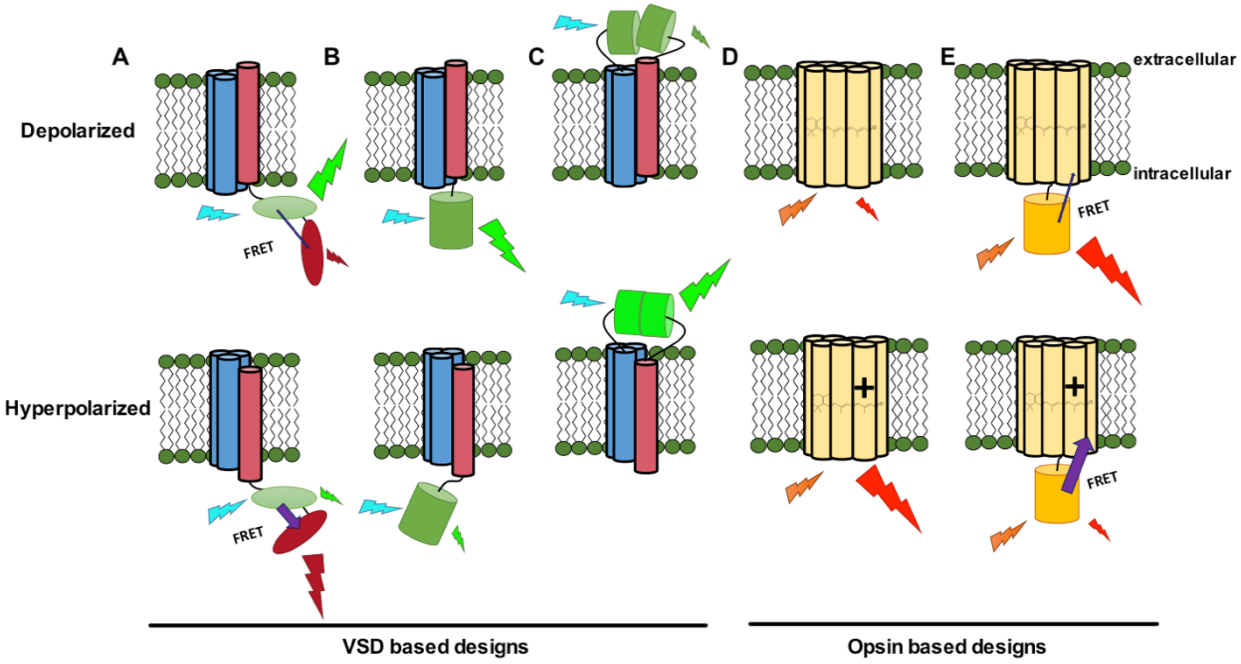

Figure 1.2 - Genetically encoded voltage indicators.
A cartoon compilation of different types of GEVIs. The top row shows GEVIs' responses in depolarized conditions. The bottom row has GEVIs' response in hyperpolarized conditions. **A)** VSFP – this design fused fluorescent protein pairs that have FRET with each other. When the VSD moves in response to voltage changes this causes a conformational change in the FRET pairs with decreased donor emission and increased acceptor emission. **B)** Arclight – this design adds a mutant of a pHluorin to a CiVSP VSD **C)** ASAP1 – this design attaches a circularly permuted GFP to the S3-S4 Linker of a *Gallus gallus* VSD. As the membrane depolarizes the fluorescence decreases. **D)** Arch – this design utilizes a modified rhodopsin, where voltage sensitivity comes from Schiff base protonation. With depolarization, protonation increases, leading to increase rhodopsin absorption and fluorescence emission. **E)** FRET-opsin – this design uses opsin bound to a fluorescent protein or tag domain which can bind a fluorophore. This fluorescent protein or fluorophore bound by a tag domain is a FRET donor to the rhodopsin FRET acceptor. With depolarization, the fluorescence of the small molecule decreases, thus increasing the FRET to the rhodopsin domain. Adapted from Gong, 2015.

In the first voltage sensing domain based design, FLaSH, a GFP is inserted into the C-terminus of the S6 helix of Shaker (Siegel and Isacoff, 1997). This GEVI was slow due to the fact that the fluorescence response was determined by the kinetics of C-type inactivation. Other attempts added Förster resonance energy transfer (FRET) pairs to VSDs (Sakai et al., 2001). When the voltage sensor moves in response to a change in the membrane potential, the relative orientation of the FRET pair is altered, generating an observable change in FRET efficiency from the donor to the acceptor fluorophore (Figure 1.2A). Many of these GEVIs had problems with mammalian cell membrane localization and small signal (Baker et al., 2007) which led to the creation of ArcLight which attaches a super ecliptic pHluorin GFP, a pH sensitive GFP, to the end of a *Ciona intestinalis* VSD (CiVSD) (Jin et al., 2012) (Figure 1.2B). However, Arclight has relatively slow temporal resolution in the range of 10 ms. ASAP1 is a newer GEVI that relies on a truncated *Gallus* g*allus* voltage sensitive phosphatase with a circularly permuted GFP added to the S3-S4 linker (St-Pierre et al., 2014) (Figure 1.2C). This GEVI has the ability to follow action potentials with high fidelity up to 100 Hz.

Because this GEVI was based on a different species' VSD, we wanted to characterize ASAP1. While we confirmed its ability to track action potentials and uncovered a sub-millisecond fluorescence lag, we also found a plateau in the fluorescence response in the physiological range. This drawback limits ASAP1's response in the voltage range most likely to be targeted in experiments. Using a rational design method we improved ASAP1, generating a new GEVI, ASAP-Y (Lee and Bezanilla, 2017) (Chapter 2). Continuing to study the VSD can aid in the development of better GEVIs (Jin et al., 2012; Treger et al., 2015; Yang and St-Pierre, 2016). Not only is the creation of new sensors useful, but the characterization of existing ones

can increase their effectiveness as an experimental tool as evidenced by improvements on Arclight (Treger et al., 2015) and ASAP1 (Lee and Bezanilla, 2017).

Unnatural amino acids

Another useful technique for understanding ion channel function is the incorporation of unnatural amino acids (UAAs). This method relies on an *in vivo* nonsense suppression approach that uses the amber stop codon (TAG) placed at the site of interest in a gene and the corresponding orthogonal tRNA. This tRNA carries a UAA of our choosing (Pless and Ahern, 2013; Ryu and Schultz, 2006). The co-injection of these tRNA and mRNA with the TAG stop codon at the residue of interest, places the UAA at the site of interest. This specific method of labeling allows for directly labeling a residue of interest with a chosen unnatural amino acid. UAAs have the advantages of labeling residues that are inaccessible to traditional labeling methods and allow for non-traditional amino acid residues to be placed such as fluorinated phenylalanines or citrulline (Infield et al., 2018; Pless et al., 2011) or fluorescent dyes (Kalstrup and Blunck, 2013; Leisle et al., 2016). To delineate the difference in importance of charge versus shape of an amino acid we replaced arginines in the S4 of Shaker with the neutral amino acid citrulline (Infield et al., 2018) (Chapter 5). Moreover, incorporation of fUAA can improve signal to noise ratios by decreasing non-specific labeling. However, it should be noted that expression of UAA constructs are lower. We attempted to employ these methods to optically track less accessible gating charges in Shaker using fUAA-qBBr (Chapter 5).

Single molecule experiments

Prior to single channel patch clamp, only macroscopic current from the collective movement of ions through a population of channels (Figure 1.3) could be measured. Studies were limited to lipid bilayer experiments where they observed the permeability and voltage

dependence conductance of different ions using lipid bilayer experiments with excitability-inducing material (Latorre et al., 1972). With the development of the patch clamp, ion channel function could now be studied for what it is: stochastic events. This unitary analysis of ion channels could quantify the flow of ions through a single channel and calculate open and closed times. When studied at different voltages, we can obtain precise kinetic data from ion channel opening and closing probabilities. With this new technique, scientists obtained single channel recordings of voltage-gated ion channels (Miller, 1978; Sigworth and Neher, 1980). Moreover, this technical development allowed for the distinguishing between different types of channels based on differences in ion selectivity and voltage dependence (Fox et al., 1987).

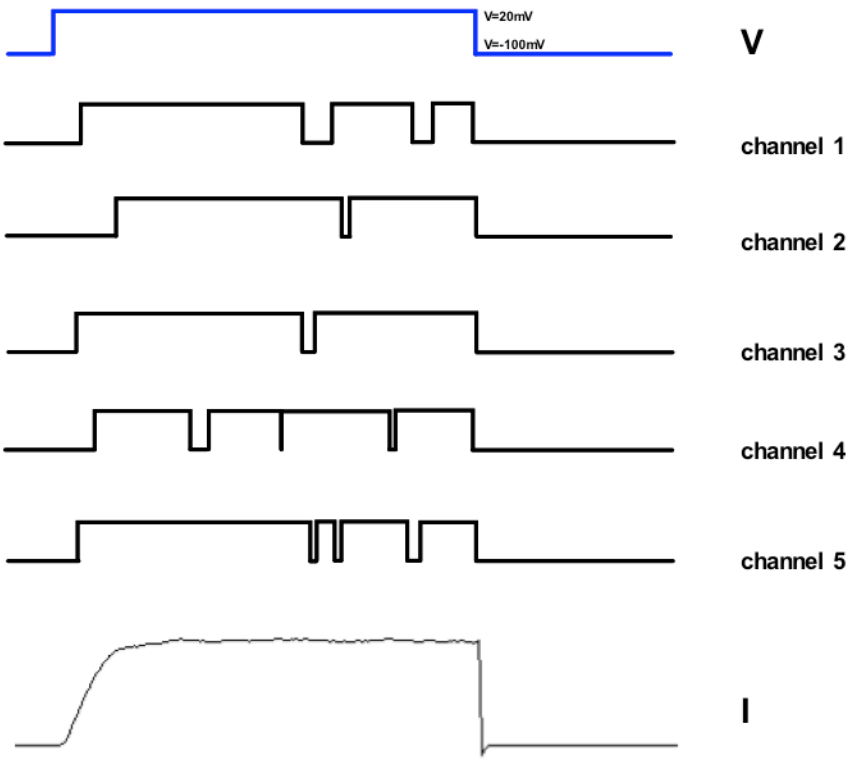

Figure 1.3 - Generation of macroscopic current from single channel recordings
Simulated single channel data for a potassium voltage-gated ion channel at 20 mV. The top trace is the voltage pulse. The consecutive traces are single channel opening events. The bottom trace is the ensemble average of the single channel traces for a macroscopic current.

Unfortunately, we are unable to use electrophysiological methods to study the VSD at the single molecule magnitude, for there are some challenges. Unlike ionic flux, which produces large currents due to the number of charges moved, the movement from the gating charges produces very small currents. In fact, the currents we can obtain from an individual voltage sensor are far too small and too fast to resolve them electrically although their properties can be inferred by noise analysis (Bezanilla, 2005; Conti and Stühmer, 1989; Sigg et al., 1994). However, several alternatives for investigating single molecules have been developed, such as employing optical methods. These types of studies can lead to new insights about the kinetics of voltage sensor movement and lead to a fuller description of the VSD mechanism of action (Treger et al., 2015). We have attempted single molecule fluorescence recordings with incorporation of fUAA-Cy3 but were unable to resolve single molecules. Alternative methods such as lowering expression of the construct with the fUAA could lead to improved results (Chapter 5).

While the VSD itself has been the subject of intense study, much about how it functions is still unknown. Through creative new technologies, we now have the ability to more thoroughly investigate the VSD and apply that knowledge to creating innovative biophysical tools.

Chapter 2 - Biophysical Characterization of Genetically Encoded Voltage Sensor ASAP1: Dynamic Range Improvement

Note: The following section is reproduced verbatim, with the exception of figure renumbering, reference reformatting, and combining of supplemental information into the main text, from Lee, E.E.L., and Bezanilla, F. (2017). Biophysical Characterization of Genetically Encoded Voltage Sensor ASAP1: Dynamic Range Improvement. Biophys. J. *113*, 2178–2181. It is reproduced here under the Elsevier user license

Abstract

Recent work has introduced a new fluorescent voltage sensor, ASAP1, which can monitor rapid trains of action potentials in cultured neurons. This indicator is based on the *Gallus gallus* voltage-sensitive phosphatase with the phosphatase domain removed and a circularly permuted GFP placed in the S3-S4 linker. However, many of the biophysical details of this indicator remain unknown. In this work, we study the biophysical properties of ASAP1. Using the cut-open voltage clamp technique, we have simultaneously recorded fluorescence signals and gating currents from *Xenopus laevis* oocytes expressing ASAP1. Gating charge movement and fluorescence kinetics track closely with each other, although ASAP1 gating currents are significantly faster than those of *Ciona intestinalis* voltage-sensitive phosphatase. Altering the residue before the first gating charge removes a split in the ASAP1 QV curve but preserves the accelerated kinetics that allow for the faithful tracking of action potentials in neurons.

The hunt for a robust, genetically encoded voltage indicator (GEVI) has been ongoing for the last several decades (Baker et al., 2008). Although some rely on rhodopsin constructs (Hochbaum et al., 2014), alternative GEVI designs capitalize on modifications of stereotypical

S4-type voltage sensors like ArcLight and VSFP2.3 (Jin et al., 2012; Lundby et al., 2010). Accelerated sensor of action potentials 1 (ASAP1) (St-Pierre et al., 2014), is based on a mutated voltage-sensing domain of Gallus gallus (GgVSD) voltage-sensitive phosphatase, where a circularly permuted GFP (cpGFP) (Pédelacq et al., 2006) is added in the S3-S4 linker, making the fluorophore extracellular. The first arginine of GgVSD is mutated to a glutamine (R153Q), shifting the voltage dependence. Previous studies have demonstrated the ability of ASAP1 and its subsequent versions to follow action potentials in neurons in vitro (St-Pierre et al., 2014) and in vivo (Yang et al., 2016). Yet, a deeper understanding of the mechanism of ASAP1 could generate a more versatile GEVI. By incorporating rationally chosen mutations, we can evaluate the degree to which this voltage-sensitive phosphatase resembles, functionally and structurally,

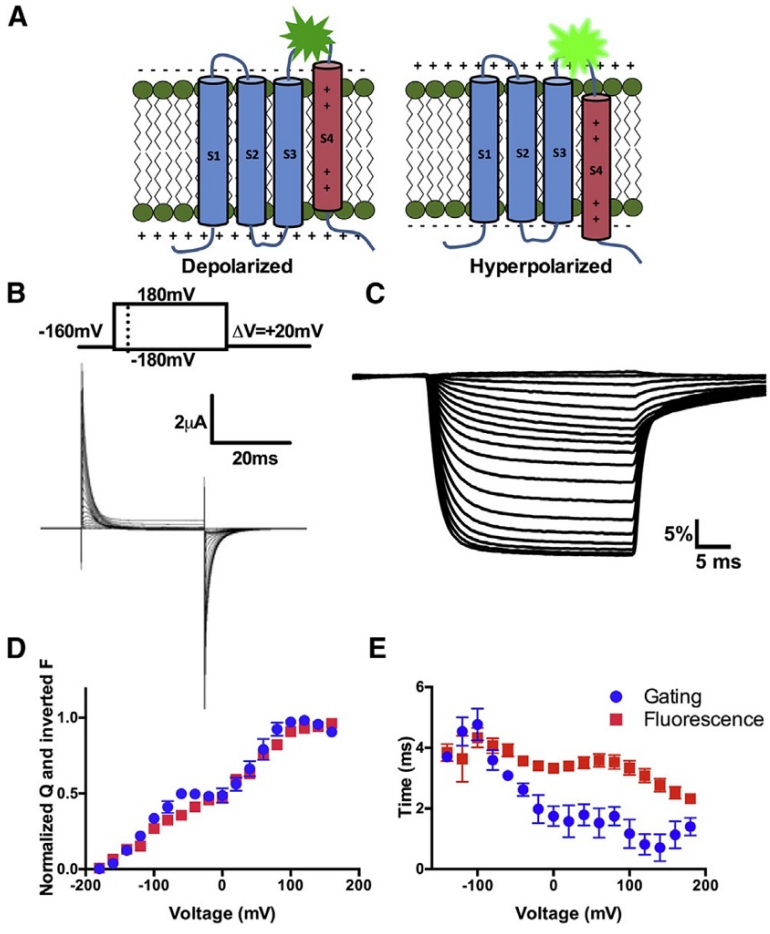

FIGURE 2.1 Biophysical characterization of ASAP1. (A) A cartoon representation of the design of ASAP1. (B) Representative gating current recordings of ASAP1. The inset describes the pulse protocol. From a holding potential of 60 mV, a 50 ms prepulse to 160 mV is followed by a 30 ms variable voltage pulse from 180 to 180 mV in increments of 20 mV, with a 50 ms postpulse at 160 mV. (C) Representative traces of ASAP1 fluorescence, with the same pulse procedure. (D) Normalized QV and 1-$FV_{normalized}$ (inverted fluorescence) curves for ASAP1. (E) A comparison of the activation τ_{fast} of the gating charge and the fluorescence of ASAP1. Gating as circles and fluorescence as squares; n = 11.

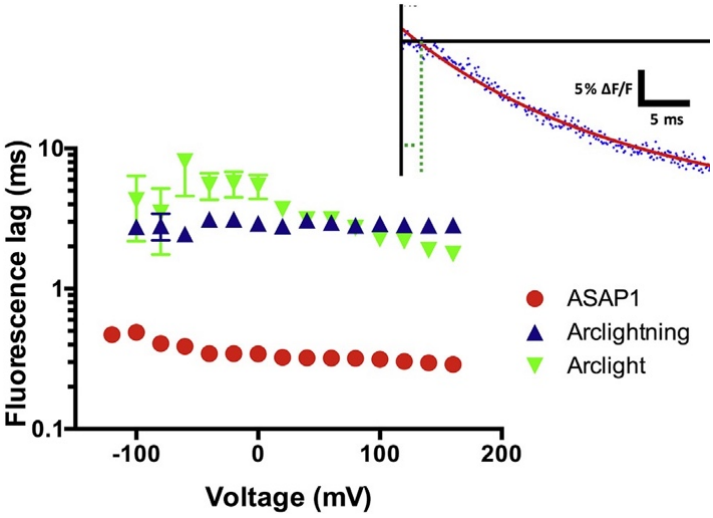

FIGURE 2.2 Small fluorescence lag in ASAP1. A comparison of fluorescence lags, calculated from double exponential fits (see inset), of different GEVIs as a function voltage with ASAP1 as circles, ArcLight as inverted triangles, and ArcLightning in triangles shows a very short lag for ASAP1. Inset: Data are the small dots, the fitted curve is the solid line, and the fluorescence lag is measured as the distance from the intersection of the fitted curve to the x axis, as shown with the dashed line. ASAP1: n = 11; ArcLight: n = 5; ArcLightning: n = 5.

the extensively investigated Ciona intestinalis voltage sensitive phosphatase (CiVSP). This way we can determine the nature of its accelerated kinetics, and engineer faster and more robust voltage indicators. We expressed ASAP1 in Xenopus laevis oocytes and simultaneously recorded gating currents (Figure 2.1A) and fluorescence signals (Figure 2.1B) using the cut-open voltage clamp method (Stefani and Bezanilla, 1998). ASAP1 displays a striking split in both electrophysiological and optical signals, indicating the presence of an intermediate state (Figure 2.1C). The fluorescence signal shows high fidelity to the movement of the gating charge. Both the kinetics of fluorescence and gating charge movement have a slow and a fast component, where the majority of the kinetics is determined by the fast component (Table 2.1). The

		Gating charge	Fluorescence
ASAP1	τ_{fast} (ms)	1.52±0.49	3.59±0.22
	τ_{slow} (ms)	52.1±3.22	72.01±8.2
	Percentage fast	74.5±2.63	73.4±2.6
ASAP-Y	τ_{fast} (ms)	1.95±0.29	1.74±0.23
	τ_{slow} (ms)	6.86±1.39	22.79±2.7
	Percentage fast	76.1±4.5	85.6±1.9

Table 2.1 - Activation Kinetics of ASAP1 and ASAP-Y.
A comparison of activation kinetics of gating charge and fluorescence of ASAP1 and ASAP-Y at 60 mV. Data are presented as mean±S.E.M. ASAP1, n=8, ASAP-Y, n=6.

component of the gating charge time constants (τ_{fast}) and the fluorescence signal are in the 1–4 ms range (Figure 2.1D). Another important metric for all GEVIs is the time it takes for the fluorescence to change in response to a change in voltage, called the fluorescence lag. For ASAP1, this lag is in the submillisecond range and represents a large improvement compared with other GEVIs (Figure 2.2).

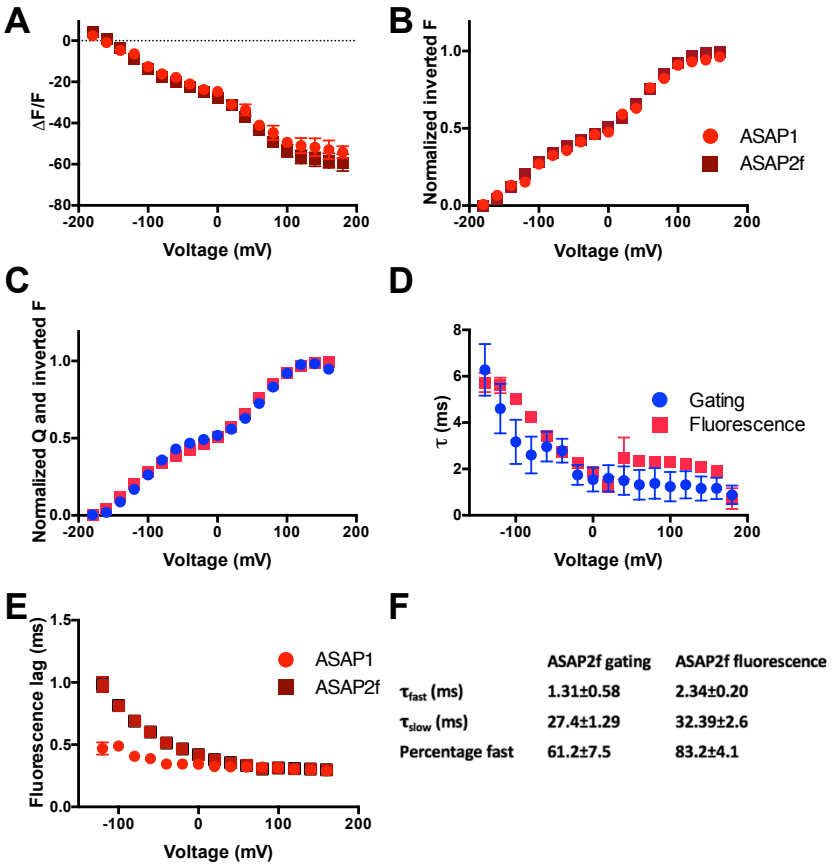

Figure 2.3 Biophysical characterization of ASAP2f. **A)** Comparison of the ΔF/F of ASAP1(bright red, circles) to ASAP2f (dark red, squares). **B)** Comparison of the QV curves of ASAP1(bright red, circles) to ASAP2f (dark red, squares). **C)** Comparison of $QV_{normalized}$ and $1\text{-}FV_{normalized}$ (inverted fluorescence) of ASAP2f gating (blue, circles) and fluorescence (red, squares). **D)** The weighted **τ**'s of ASAP2f activation gating (blue, circles) and fluorescence (red, squares). **E)** A comparison of fluorescence lag of ASAP1 (bright red, circles) vs ASAP2f (dark red, squares). **F)** Table of activation τ at 60mV of ASAP2f (ASAP1 n=8, ASAP2f n = 6).

The split in the QV creates a plateau between 100 and 0 mV, which occurs in both the QV and FV and points to a stable intermediate state. This clearly limits the dynamic potential of ASAP1 and subsequent versions like ASAP2f by limiting the fluorescence read-out in the

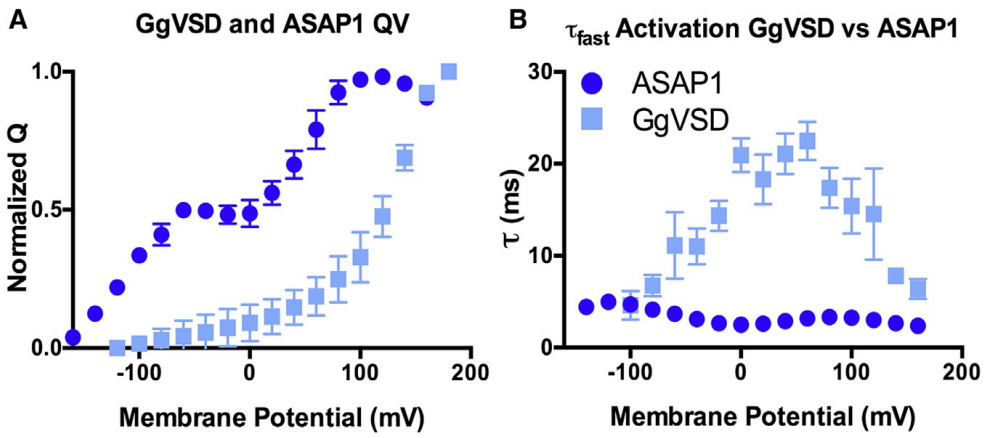

FIGURE 2.4 Biophysical characterization of GgVSD. (A) A comparison of the QV curves of GgVSD (square) versus ASAP1 (circle). (B) A comparison of the fast activation t of GgVSD and ASAP1. Error bars are within the symbols. ASAP1: n = 11; GgVSD: n = 6.

physiological voltage range (Figure 2.3). A large split in the QV is not a property shared by other voltage-sensitive phosphatases (Murata et al., 2005), thus we hypothesized that this phenomenon might be related to the addition of the GFP in the S3-S4 linker. Indeed, removal of the cpGFP from ASAP1, also known as GgVSD R153Q, leads to a sensor with a QV curve fitted by a two-state model (a single Boltzmann). Figure 2.4 shows that the kinetics and steady-state features of GgVSD and ASAP1 are drastically different from one another as a result of the

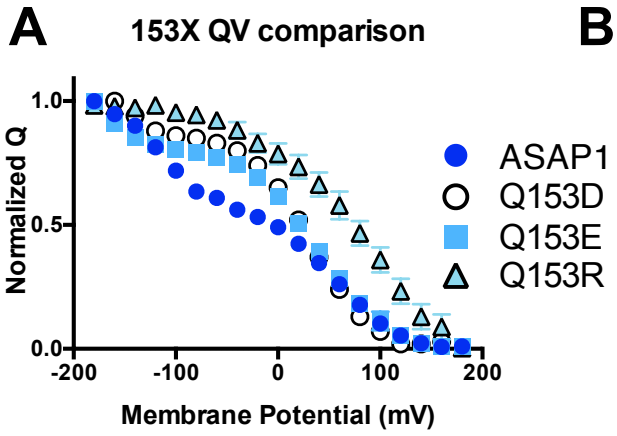

B

Construct	$V_{1/2}$ (mV)
ASAP1	-5.52
Q153D	27.73
Q153E	33.12
Q153R	92.93

Figure 2.5 CiVSP-R217X-motivated mutation in ASAP1.
A) A comparison of the QV_{off} with several residues at position 153 ASAP1 (blue, circle), Q153D (white, circle), Q153E (light blue, square), Q153R (light blue ,triangle). **B)** $V_{1/2}$ of ASAP1 153X constructs. (ASAP1 n=11, Q153D n=5 , Q153E n=4, Q153R n=5) (Villalba-Galea et al., 2008)(Villalba-Galea et al., 2008)

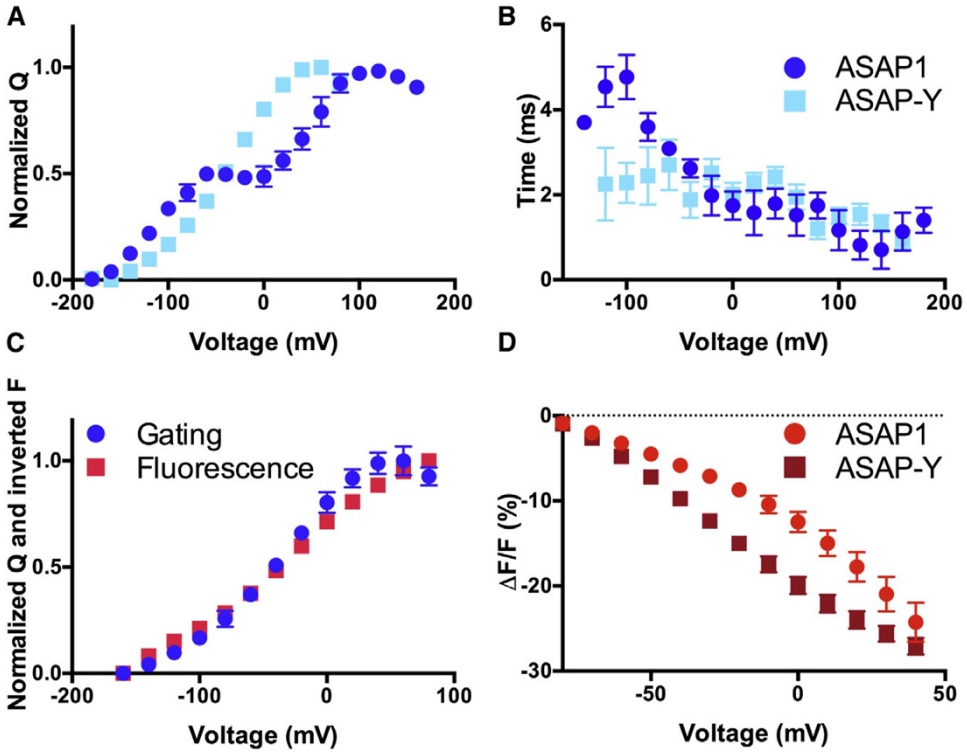

FIGURE 2.6 Biophysical characterization of ASAP-Y and comparison to ASAP1. (A) Normalized QV curves for ASAP1 (circle) and ASAP-Y (square). (B) A comparison of the activation τ_{fast} of the gating charge for ASAP1 and ASAP-Y. (C) Normalized QV (circle) and 1-$FV_{normalized}$ (square) curves for ASAP-Y. (D) A comparison of the ΔF/F % in a physiological range of ASAP1 (circle) and ASAP-Y (square). (ASAP1: n = 8; ASAP-Y: n = 6).

addition of a cpGFP to the S3-S4 linker. We reasoned that addition of the cpGFP led to an acceleration in gating current kinetics not seen in other voltage-sensitive phosphatases (Murata et al., 2005; Villalba-Galea et al., 2009).

Residues in the hydrophobic plug of ASAP1 are similar to those in CiVSP, such as I126 (Lacroix and Bezanilla, 2012). Moreover, gating and fluorescence kinetics in ASAP1 are very similar to each other. Therefore, we hypothesized that alterations of these similar hydrophobic plug residues in ASAP1 would result in accelerated gating. However, although some of the mutations effectively altered the biophysical properties of ASAP1 (Figure 2.5 and Appendix Table 2.2), the analogous mutations in CiVSP did not improve the fluorescence signal or accelerate sensing kinetics.

This may be due to the cpGFP in the linker. Recent work (Carvalho-de-Souza and Bezanilla, 2017) in the voltage-gated potassium channel Shaker has demonstrated the importance of nonsensing residues in position 361 for tuning the voltage dependence of the voltage-sensing domain, and we have used this knowledge to further improve on ASAP1. Changing leucine 158 to a tyrosine removed the intermediate state in the QV curve but preserved the accelerated kinetics and large signal (Figure 2.4A–C). The τ_{fast} of the gating charge and the fluorescence were 1.95 ± 0.29 and 1.74 ± 0.23 ms (mean±S.E.M) at 60 mV, respectively. Change of this magnitude in the QV and FV curves within the physiological range generates a larger dynamic range than ASAP1 (Figure 2.6 D). We named this new variant of ASAP1, ASAP-Y. To determine the effectiveness of our new tool, we transfected rat dorsal root ganglion neurons with ASAP1 and ASAP-Y and recorded action potentials using whole-cell patch clamp. ASAP-Y has comparable transfection efficiency and photobleaching properties to ASAP1 (Figure 2.7).

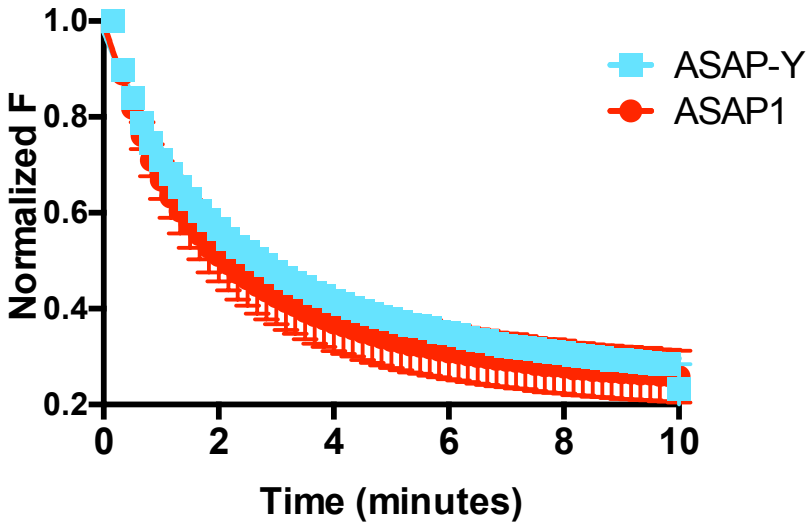

Figure 2.7 Photobleaching properties of ASAP1 and ASAP-Y. Cultured DRG neurons expressing ASAP1(red, circles) or ASAP-Y (light blue, squares) were illuminated continuously with 488nm light at 1.5W/cm^2. Each neuron was imaged every 10 seconds for 10 minutes. Fluorescence was normalized to 1.0 at t =0. Photobleaching time constants (τ) were estimated from single exponential fits with ASAP1 1.852 min and ASAP-Y 2.282min. ASAP1, n=7, ASAP-Y, n=8

We observed fluorescence read-outs of action potentials with both ASAP1 and ASAP-Y and demonstrated increased signal amplitude with ASAP-Y, even though the voltage range spanned by the action potentials in both cases was similar (Figure 2.8A). This result is expected when comparing the FV curves of ASAP1 and ASAP-Y (Figure 2.1D and 2.6C). Furthermore, ASAP-Y displayed faster kinetics on the return to baseline than ASAP1 (Figure 2.8B). We found that the fast kinetics of ASAP1 and ASAP-Y are due to the addition of the cpGFP in the S3-S4 loop. This observation is in line with the reported crystal structures of CiVSP in the resting and activated states (Li et al., 2014), where it was found that the position of this loop changes drastically during activation.

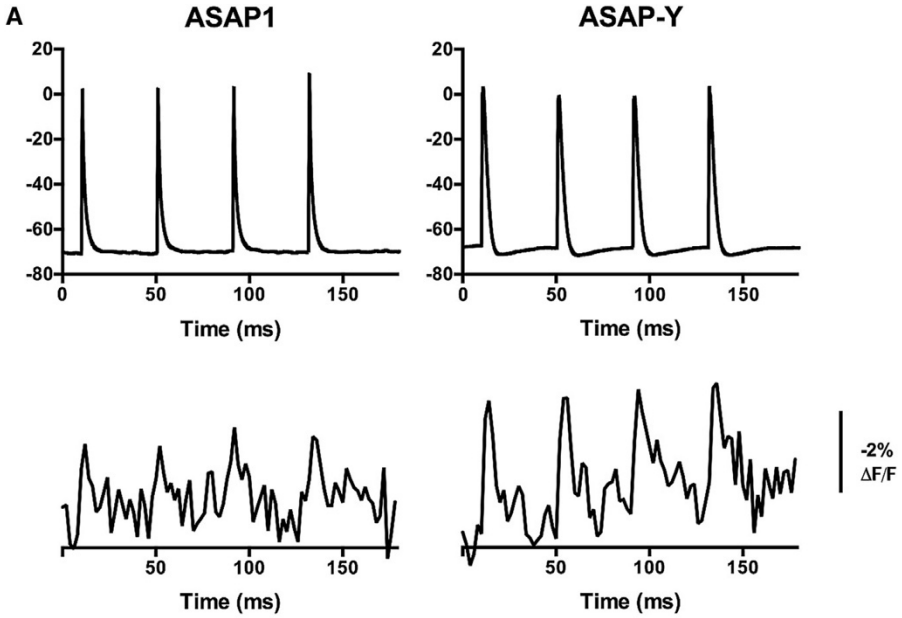

B

	ASAP1	ASAP-Y
ΔF/F per 100 mV (%)	-7.45±0.80	-9.49±0.77
Deactivation τ (ms)	6.52±0.51	4.63±0.44

FIGURE 2.8 ASAP-Y can follow action potentials in rat dorsal root ganglion neurons. (A) Representative traces of action potentials from dorsal root ganglion neurons transfected with ASAP1 (left) and ASAP-Y (right). Corresponding fluorescence traces are shown below as ΔF/F (%). (B) A table comparing the ΔF/F per 100 mV and deactivation t of ASAP1 and ASAP-Y fluorescence. ASAP1: n = 11; ASAP-Y: n = 13.

In conclusion, a rational design method has allowed us to improve upon an existing GEVI to create ASAP-Y. This is, to our knowledge, a novel optical voltage probe with a steeper fluorescence response in the physiological range of voltage changes.

AUTHOR CONTRIBUTIONS

F.B. and E.E.L.L. designed research, analyzed data, and wrote the manuscript. E.E.L.L. performed research. F.B. contributed analytic tools.

ACKNOWLEDGMENTS

We thank Li Tang for culturing rat dorsal root ganglion neurons and Dr. Michael Priest and Dr. Eduardo Perozo for editing. We give special thanks to Dr. João Carvalho-de-Souza for patch clamp training E.E.L.L.

This work was supported by the National Institutes of Health grants R01GM030376 and U54GM087519.

Methods

Cell culture

Glass-bottomed culture dishes (Cellvis, Mountain View, CA) were thoroughly cleaned, rinsed with water, dried, and sterilized with UV light. They were then incubated with poly-L-lysine (PLL, Thermo Fischer Scientific) for 15 min at room temperature, after which they were rinsed with sterile water several times and stored until use.

Dorsal root ganglia were isolated from P1-P3 Sprague-Dawley rats following decapitation and were immediately placed in DMEM medium (Thermo Fisher Scientific) on ice. Ganglia were rinsed multiple times with Earle's Balanced Salt Solution (EBSS, Thermo Fisher Scientific) then digested with EBSS + 0.25% trypsin (Thermo Fisher Scientific) for 20 min at 37 C with shaking. Following digestion, the cells were centrifuged, and the supernatant removed and replaced with EBSS + 10% Fetal bovine serum (FBS, Thermo Fisher Scientific) to inhibit remaining trypsin. The digested ganglia were then extruded through three glass pipettes of decreasing size to mechanically disperse the cells. The cells were centrifuged a final time and the supernatant replaced with DMEM + 5% FBS. Cells were seeded into the previously prepared PLL-treated culture dishes and allowed to sit undisturbed for 30 min to facilitate DRG cell adhesion to the PLL-treated glass. Finally, the dishes were flooded with DMEM + 5% FBS + 100 U/ml penicillin (Thermo Fisher Scientific) + 100 μg/ml streptomycin (DRG media) and incubated at 37° C with 5% CO_2 until use.

Molecular biology

ASAP1 for Xenopus laevis expression was created from the pcDNA3.1/Puro-CAG-ASAP1 which was a gift from Michael Lin (Addgene plasmid # 52519) (St-Pierre et al., 2014). ASAP-Y was identical to ASAP1 with an additional point mutation at L158Y. Using site-directed

mutagenesis by polymerase chain reaction, we added L158Y to this construct and verified it via sequencing. ASAP2f for Xenopus laevis expression was created from ASAP1 with the removal of A146 and the change of residue 147 from an alanine to a serine as described previously (Yang et al., 2016).

For oocyte expression, DNA was prepared using the NucleoSpin Plasmid kit (Macherey-Nagel, Bethlehem, PA) and linearized with XbaI (New England Biolabs, Ipswich, MA). Linearized cDNA was transcribed to RNA with the mMESSAGE mMACHINE Sp6 kit (Life Technologies, Carlsbad, CA). Oocytes were injected with 50 ng of RNA and incubated at 18°C in solution containing (in mM) 96 NaCl, 2 KCl, 1.8 $CaCl_2$, 1 $MgCl_2$, 10 HEPES, at pH 7.4 with 10 mg/L of gentamicin. Recordings were made 1-2 days following injection.

For neuronal mammalian cell expression, DNA was prepared using the NucleoBond Xtra Midi Plus kit (Macherey-Nagel). DNA was then transfected into rat DRG neurons had been previously plated on glass coverslips at low density, using Lipofectamine 2000 reagent (Thermo Fisher Scientific, Waltham, MA). To transfect, each dish had mixture of OptiMem (Thermo Fisher Scientific), Lipofectatmine 2000, and 6 ug of DNA added drop-wise. After five hours, the cells were gently rinsed with DRG media and incubated at 37°C with 5% CO_2, 24-48 hours prior to recording.

Electrophysiology

For oocytes, simultaneous recordings of ASAP1 gating currents and fluorescence responses were performed using the cut-open oocyte voltage-clamp technique (Stefani and Bezanilla, 1998) in combination with a photodiode to measure temporal changes in fluorescence emission (Cha and Bezanilla, 1998). Gpatch, an in-house program, controlled an SB6711 digital signal processor-

based board (Innovative Integration, Simi Valley, CA) with an A4D4 board (Innovative Integration, Simi Valley, CA). Oocytes were held under voltage-clamp with a Dagan CA-1B amplifier (Minneapolis, MN) and current was filtered at 5 kHz. ASAP1 was sampled at 50 kHz and subsequent constructs' fluorescence emissions were collected through an Olympus LUMPlan FL N 40X/0.8 NA water-immersion objective by a PIN-020A photodiode (UDT Technologies, Torrance, CA), amplified by a patch clamp amplifier L/M-EPC-7 by LIST Medical Electronic (Darmstadt, West Germany) with a filter of 10 kHz, and then integrated over each sampling period using a home-built integrator circuit. ASAP1 and subsequent constructs were excited via a ThorLabs LED controller triggering a 470 nm LED (ThorLabs, Newton, New Jersey) that was passed through a filter cube housing a 480/40 excitation filter, a 505 long-pass dichroic, and a 535/50 emission filter (Chroma, Bellows Falls, VT). All recordings were performed at around 18°C, with an external solution containing (in mM) 115 N-methyl-D-glucamine/methanesulfonic acid (NMG/MES), 10 HEPES, and 2 $Ca(OH)_2$ and an internal solution containing (in mM) 115 NMG-MES, 10 HEPES, and 2 EGTA. Both solutions were set to pH 7.5. Microelectrodes were pulled on a Flaming/Brown micropipette puller (Sutter Instruments, Novato, CA, model P-87) and were filled with 3 M $CsCl_2$ and had a resistance of ~0.2–0.8 MΩ.

For neuronal mammalian cell expression, ASAP1 and ASAP-Y fluorescence from dorsal root ganglion neurons was recorded by an Evolve 128 EMCCD camera (Photometrics, Tucson, Arizona) attached to an Olympus IX71 inverted microscope (Center Valley, Pennsylvania) with a 40X/0.6 NA microscope objective (Olympus). Excitation was provided by a 473 nm DPSS laser (Shanghai Dream Lasers Technology Co., Ltd., Shanghai, China). Typical excitation intensities were around 1.5W/cm^2 through the 40X objective listed above. Fluorescence was

observed through a T495lpxt dichroic and ET500lp emission filter (Chroma Technology Corp., Bellows Falls, VT).

Patch clamp was performed with an Axopatch 200A integrating patch clamp amplifier (Molecular Devices, Sunnyvale, CA). Both the electrophysiological and optical equipment were controlled using in-house software. Recordings were performed at around 18ºC, in a solution containing (in mM) 132 NaCl, 4 KCl, 1.2 $MgCl_2$, 1.8 $CaCl_2$, 10 HEPES, 5.5 Glucose, pH 7.4 with NaOH. Patch pipettes pulled on Sutter model P-2000 (Sutter Instrument Co., Novato, CA) were filled with a solution containing (in mM) 10 NaCl, 130 KF, 4.5 $MgCl_2$, 10 HEPES, 9 EGTA, 2 ATP, pH 7.3.

Data analysis

Data analysis was performed in MATLAB (The MathWorks, Inc., Natick, MA), as well as in-house software. The time constants of gating charge were taken using double exponential fits to the rising phase of the integration of the gating current. Kinetics of fluorescence traces were first taken from double exponential fits to the trace; when fit with two exponentials, fluorescence traces obtained from off pulses in oocytes only had one meaningful time constant, and thus were refit with one exponential. For the DRGs, time constants of the fluorescence deactivation were taken using an exponential fit to the decay of the fluorescence signal from the action potential. For clarity of comparison, all kinetics were reported as τ_{fast}, which denotes the faster and larger amplitude component of the fluorescence traces. Q-V curves were calculated by normalizing the integral of the gating current following a sloped baseline subtraction to remove leak current. (Villalba-Galea et al., 2008)

Chapter 3 - Methodological Improvements for Fluorescence Recordings in *Xenopus laevis* Oocytes.

Note: The following section is reproduced verbatim, with the exception of figure renumbering, reference reformatting, and combining of supplemental information into the main text, from Lee, E.E.L., and Bezanilla, F. (2018). Methodological improvements for fluorescence recordings in Xenopus laevis oocytes. *J. Gen Physio*.

Abstract

Xenopus laevis oocytes are a widely used model system because of their capacity to translate exogenous mRNA, but their high intrinsic background fluorescence is a disadvantage for fluorescence recordings. Here we develop two distinct methods for improving fluorescence recordings from oocytes. One is a pharmacological method in which a small molecule salt-inducible kinase (SIK) inhibitor is co-injected with the mRNA of interest to stimulate melanin production. We interrogated the oocytes using cut-open voltage clamp and found that by increasing the amount of light-absorbing melanin in these oocytes, we decrease their intrinsic background fluorescence. The treated oocytes produce fluorescence signals that are ~4x larger. The second method consists of direct injection of synthetic melanin. This method also significantly improves (doubles) fluorescence signals and allows any oocyte to be used for fluorescence recording. These two methods provide significant improvements of the signal quality for fluorescent oocyte recordings and allow all healthy oocytes to be used for high-sensitivity recordings.

Introduction

Xenopus laevis oocytes are a model *in vitro* system for development, pharmacology, and

electrophysiology (Gurdon et al., 1971). In particular, oocytes have been established as an important system to study membrane proteins and ion channels (Kusano et al., 1977). When voltage clamp fluorimetry for oocytes was first introduced twenty years ago (Cha and Bezanilla, 1997)(Mannuzzu et al., 1996), it paved the way for novel optical interrogations of membrane proteins with simultaneous electrophysiology. However, optical measurements are currently limited in sensitivity by the oocyte's high intrinsic background fluorescence in the 300-500 nm wavelength range, thus decreasing the signal-to-noise ratio of recordings in this range.

Recent developments have allowed us to decrease the intrinsic fluorescence of the oocyte through melanin. Melanin is a general name for a group of small light absorbing polymers. This dark pigmented molecule plays a role in protection from UV radiation (Costin and Hearing, 2007). Melanin is a useful molecule for suppressing background fluorescence due to its wide range of absorbance (Figure 3.4A). It is well known that the wildtype expression of melanin in oocytes causes the animal pole to be darker visually and more light absorbent, and thus have less fluorescent background compared to the lighter colored vegetal pole. Thus, we sought to artificially increase the melanin content of the oocyte to further decrease the endogenous fluorescence signal in our recordings.

We demonstrate a novel drug-based method to decrease the endogenous background fluorescence of injected oocytes. A recent study found that the addition of a salt-inducible kinase (SIK) inhibitor increases melanin production in human melanocytes and *in vivo* in mice (Mujahid et al., 2017). This drug, HG 9-91-01 inhibits salt-inducible kinase 2 (SIK2) which in turn stimulates melanogenesis associated transcription factor (MITF), resulting in melanin production by melanosomes. *Xenopus* have homologs for both enzymes and transcription factors, and melanin production can be similarly regulated with HG 9-91-01.

We next demonstrate a second method to decrease endogenous background fluorescence through a direct injection of melanin. For this specific study we have chosen to use neuromelanin, which is melanin created from the oxidation of dopamine (Zeise et al., 1992). A recent study employing synthetic dopamine generated melanin as a photothermal method for treating cancer *in vivo* (Liu Yanlan et al., 2012). We used this method of synthesizing melanin, but with the aim of reducing the fluorescence background to improve oocyte recordings. These methodological improvements offer many opportunities for better fluorescence recordings in oocytes.

Results

Oocytes are variable in endogenous background fluorescence at different wavelengths

We first sought to quantify the endogenous fluorescence of oocytes prior to RNA injection, uninjected oocytes, at two different wavelengths of excitation and emission. We excited oocytes with 420 nm and 470 nm LEDs and measured emissions from a 475 nm long-pass and a 535/50 nm emission filter, respectively (Figure 3.1B and C). Oocytes' endogenous fluorescence varies by batch and wavelength (Figure 3.1). This variability can limit opportunities to do fluorescence recordings if the oocytes have an intrinsically light animal pole (high fluorescence background) color. In the extreme case, the variability may exclude some batches of oocytes from use for fluorescence recordings. We thus aimed to develop several methods to attenuate the fluorescence variability of oocytes.

Addition of injected HG-9-91-01 decreases endogenous background oocyte fluorescence.

We recorded fluorescence from the animal pole of the *Xenopus laevis* oocyte, exciting at 420 nm and collecting the emission with a 475nm long pass filter.

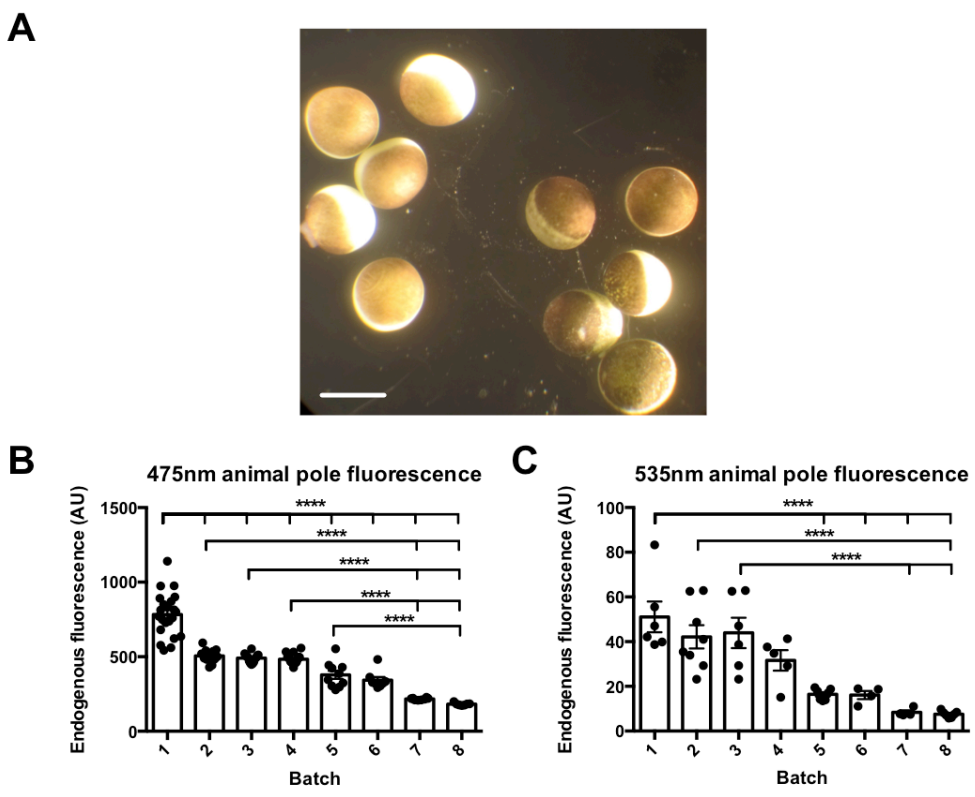

Figure 3.1 Oocytes are variable in endogenous background fluorescence at multiple wavelengths **A)** *Xenopus laevis* oocytes from different batches of oocytes, scale bar 1 mm. **B)** Endogenous background fluorescence of the animal pole exciting with a 420 nm LED reflected onto the oocytes by a 455 nm long-pass dichroic through a 40X water-immersion objective, where the emission was collected through the dichroic and a 475 nm long-pass filter. Batches are placed in order of most endogenous background to least. Batch 1 n=22, batch 2 n=11, batch 3 n=14, batch 4 n=20, batch 5 n=10, batch 6 n=8, batch 7 n=8, batch 8 n=7. A one-way analysis of variance (ANOVA) together with a *post hoc* Tukey multiple comparison's test. Only P<0.0001 (****) noted here. For further information see supplemental statistics table appendix. **C)** Endogenous background fluorescence of the animal pole exciting with a 470 nm LED that was passed through a filter cube housing a 480/40 nm excitation filter, a 505 nm long-pass dichroic, and a 535/50 nm emission filter. Batches are placed in order of most endogenous background to least. Batch 1 n=6, batch 2 n=8, batch 3 n=6, batch 4 n=5, batch 5 n=7, batch 6 n=4, batch 7 n=4, batch 8 n=7. A one-way analysis of variance (ANOVA) together with a *post hoc* Tukey multiple comparison's test. Only P<0.0001 (****) noted here. For further information see supplemental statistics table appendix. The batch numbers in B and C do not correspond and are different batches of oocytes. The measurements are in comparable optical conditions.

A genetic sequence analysis revealed homologs to both SIK2 and MITF in *Xenopus laevis* both of which are in the pathway affected by HG 9-91-01 (Figure 3.2A) (Mujahid et al., 2017). To ensure that the DMSO that HG 9-91-01 was solubilized in was not having an effect, we checked several batches and found no difference between these two groups (Figure 3.2B). Since in the original study the inhibitor was topically applied, we first attempted bath applying this drug, which did not improve oocyte endogenous fluorescence (Figure 3.2C and D). We then

performed a dose response injection of the drug into the oocyte and found that 100 µM of HG 9-91-01 decreases endogenous oocyte fluorescence (Figure 3.2C and D). Interestingly, there was a limit to how much the signal could be improved. In intrinsically dark oocytes (200-400 AU of fluorescence at 475nm) we did not observe as large of a change in endogenous fluorescence (Figure 3.2E), however in "lighter" oocytes (>500 AU of fluorescence at 475 nm), there is an improvement (Figure 3.2F).

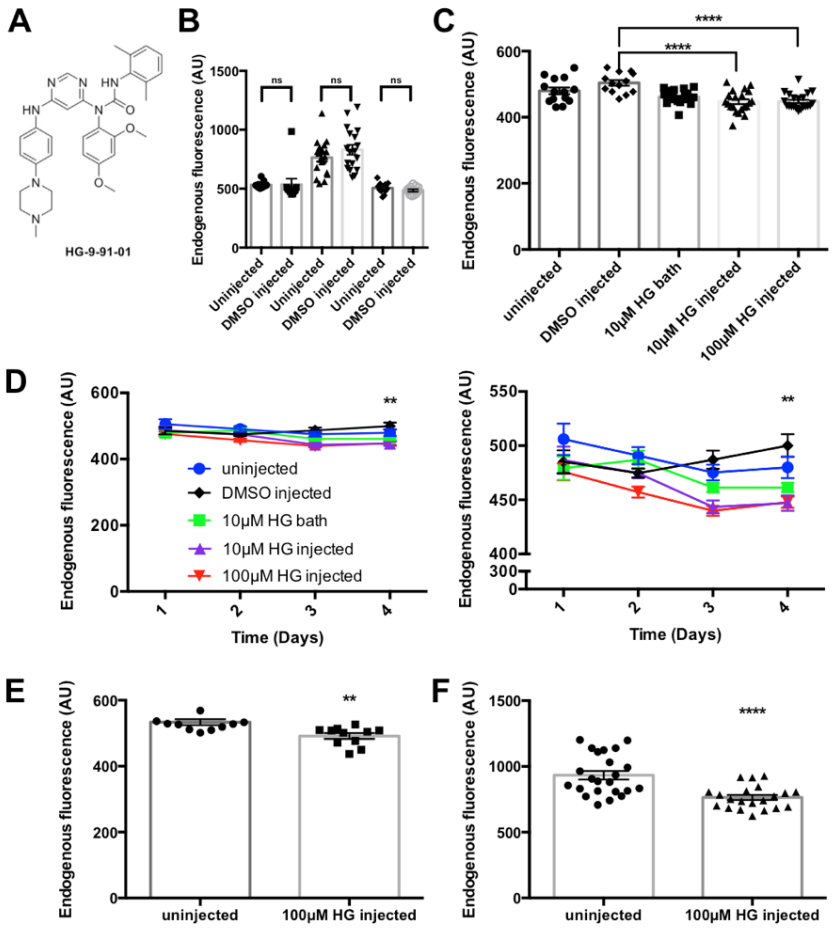

Figure 3.2 Addition of SIK inhibitor decreases background fluorescence. **A)** Chemical structure of small molecule SIK-inhibitor HG-9-91-01. **B)** Comparison of endogenous fluorescence between several batches of uninjected and 0.5% DMSO injected oocytes. One-way ANOVA with a *post hoc* Holm-Sidak's multiple comparisons test, find no significant difference with comparison to uninjected oocytes (Uninjected n= 11, 19, 11, DMSO n=10, 18, 11) **C)** Effect of HG-9-91-01 endogenous fluorescence under different conditions: uninjected (blue, circle, n=14), 0.1% DMSO injected (black, diamond, n=9), 10 µM HG 9-91-01 bath (green, square, n=22), 10 µM HG 9-91-01 injected (purple, triangle, n=21), 100 µM HG 9-91-01 injected (red, upside-down triangle, n=21) measured on day 4. One-way ANOVA with a *post hoc* Holm-Sidak's multiple comparisons test, indicate P<0.0001 (****) with comparison to uninjected oocytes. **D)** The endogenous fluorescence under different conditions measured over time as described in B. Panel on the right is a zoom in to demonstrate the effect of the different conditions described in B. Two-way ANOVA with a *post hoc* Dunnett's multiple comparisons test where 10µM HG injected and 100 µM HG injected on day 4 both have a P < 0.001 (**) **E)** Results from a darker batch of oocytes where HG-9-91-01 was tested, uninjected n=11, 100 µM HG 9-91-01 injected n=11. Unpaired two-tail t-test, P = 0.0031 (**) **F)** Results from a lighter batch of oocytes where HG-9-91-01 was tested, uninjected n=22, 100 µM HG 9-91-01 injected n=14. Unpaired two-tail t-test, P <0.0001 (****)

To determine if this method would improve the signal-to-noise ratio of fluorescence recordings in an experimental setting, we utilized dye labelled non-conductive Shaker mutants. We measured the fluorescence signal of ATTO 425 (Kubota et al., 2014) a dye that when oocytes are labeled with it causes an increase in the measured background fluorescence. We first looked at the effects of dye labeling on uninjected and 100 μM HG 9-91-01 injected oocytes (Figure 3.3A) and see that labeling with ATTO 425 greatly increases the background labeled fluorescence of both groups of oocytes (Figure 3.3B). This increase in fluorescence could be due to partitioning of dye into the membrane or even penetration of some dye into the oocyte itself (Hughes et al., 2014; Toseland, 2013). The important result here is that, after dye labeling we observe a lower intensity of fluorescence in HG 9-91-01 injected oocytes due to the increased internal melanin, which blocks the signal of internalized dye molecules, in comparison to uninjected dye labeled oocytes (Figure 3.3B).

We conjugated this dye via cysteine to a mutant of a nonconductive Shaker mutant M356C in the S3-S4 linker region (Cha and Bezanilla, 1997). This dye gives a robust voltage-dependent signal at this location (Figure 3.3C and D). We chose a batch of "lighter" oocytes to demonstrate the effect of HG 9-91-01 (Figure 3.3E). The co-injection of HG 9-91-01 does not alter the expression of the Shaker construct as we compared total gating charge in both conditions as a measure of expression (Figure 3.3F). We did not observe an alteration in the currents recorded with HG 9-91-01 co-injection. Following a labeling step with ATTO 425 and a wash, we observe a much lower intensity of fluorescence from oocytes co-injected with HG 9-91-01, despite a comparable amount of charge measured with Sh WF M356C injected oocytes (Figure 3.3G). With the labeling, the large labeled background fluorescence, masks the size of the voltage induced fluorescence signal even when expression is high.

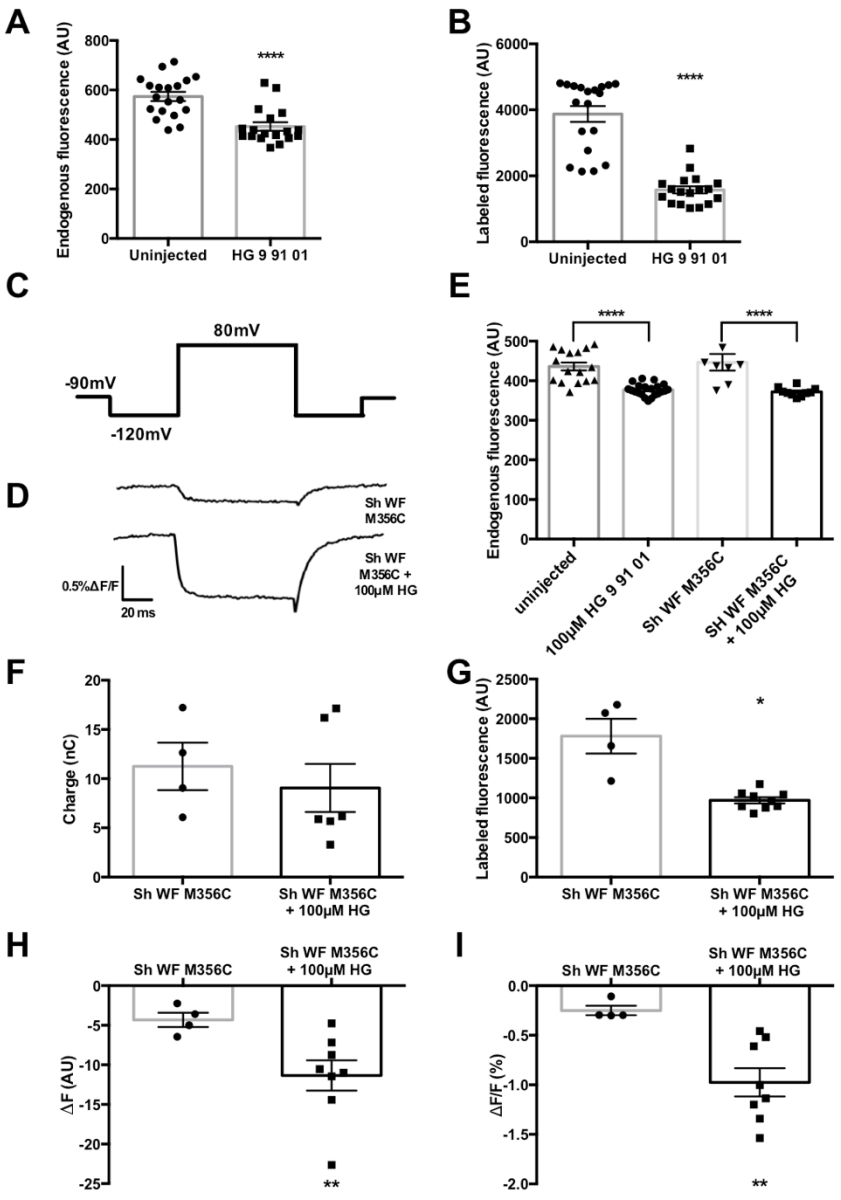

Figure 3.3. Addition of SIK inhibitor improves ATTO 425 signal. A) A comparison of uninjected (n=19) and 100 µM HG 9-91-01 injected (n=18) oocytes on day 4 before labeling with ATTO 425 **B)** After labeling with ATTO 425 n= Unpaired two-tailed t tests showed P<0.0001 (****) **C)** Pulse protocol for ATTO 425 fluorescence, where the oocytes were held at -90 mV and pre-pulsed to -120 mV for 60 ms, followed by a 80 ms pulse to 80 mV, with a post pulse of 120 mV for 60 ms before returning to the holding potential **D)** Representative trace of fluorescence data of ATTO 425 labeled Shaker W434F M356C (top) and ATTO 425 labeled Shaker W434F M356C + 100 µM HG 9-91-01 (bottom) oocytes with the pulse protocol from A. **E)** Endogenous oocyte fluorescence on day 3 was checked for several conditions (uninjected n=16, construct n=8, HG 9-91-01, n=21, construct + HG 9-91-01 n=10). Ordinary one-way ANOVA with a *post hoc* Bonferroni's multiple comparisons test, P<0.0001 (****) **F)** Comparisons of levels of expressions in Shaker W434F M356C (n=4) and Shaker W434F M356C + HG 9-91-01 (n=6) injected oocytes. Unpaired two-tailed t test showed no statistical significance P=0.5414 **G)** Comparison of background fluorescence of ATTO 425 labeled oocytes Shaker W434F M356C (n=4) and Shaker W434F M356C + HG 9-91-01 (n=8). Unpaired two-tailed t test showed P=0.0324 (*). **H)** Comparisons of fluorescence signal in Shaker W434F M356C (n=4) and Shaker W434F M356C + HG 9-91-01 (n=8) co-injected oocytes. Unpaired two-tailed t test showed P=0.0085 (**). **I)** Comparison of ΔF/F % in Shaker W434F M356C (n=4) and Shaker W434F M356C + HG 9-91-01 (n=8) co-injected oocytes.) Unpaired two-tailed t test showed P=0.0011 (**). For further information, see supplemental statistical table appendix.

To investigate if the voltage dependent signal was improved, the oocytes were depolarized to 80 mV for 80 ms. Based on previous experiments, the largest signal is generated at 80 mV and could best demonstrate the effect of HG 9-91-01 on signal size (Figure 3.3H). There is a ~0.25% ΔF/F in oocytes only injected with Sh WF M356C, however in HG 9-91-01 treated oocytes we saw ~1% ΔF/F, a fourfold increase in ΔF/F (Figure 3.3I). Thus, the voltage dependent fluorescence signal was larger mainly due to the decrease in background fluorescence by the effect of SIK inhibitor.

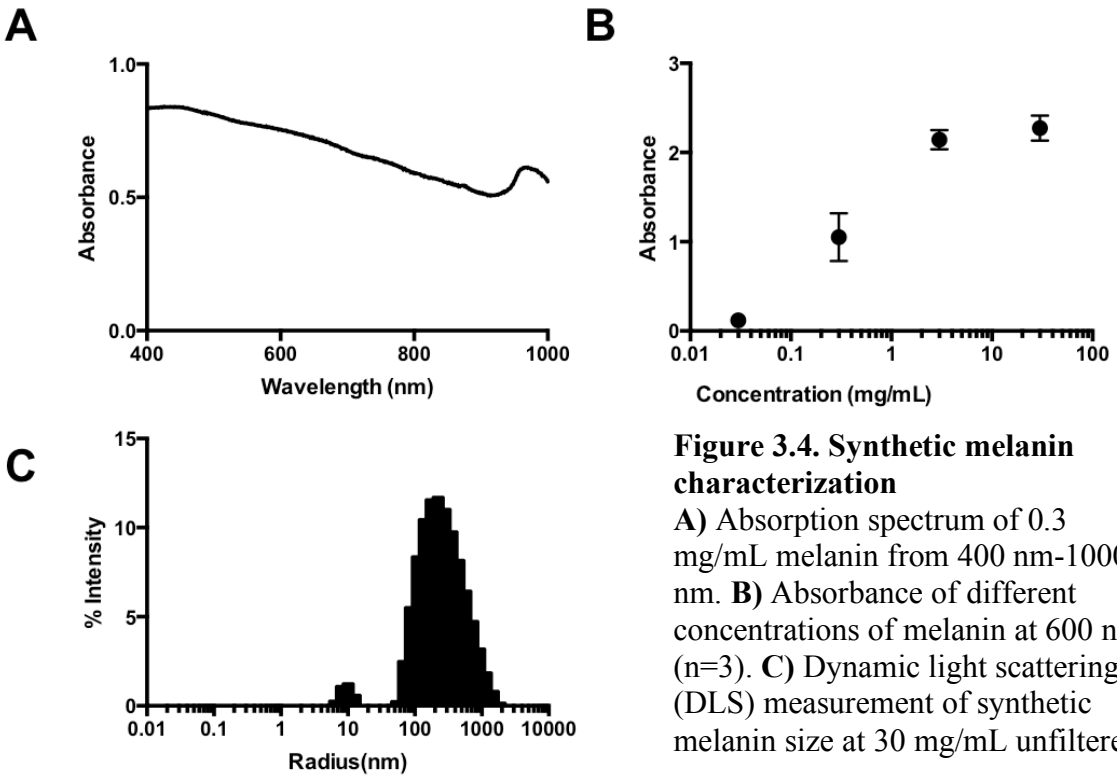

Figure 3.4. Synthetic melanin characterization
A) Absorption spectrum of 0.3 mg/mL melanin from 400 nm-1000 nm. **B)** Absorbance of different concentrations of melanin at 600 nm (n=3). **C)** Dynamic light scattering (DLS) measurement of synthetic melanin size at 30 mg/mL unfiltered,

Synthetic melanin injections significantly improve signal-to-noise ratio

The reduced endogenous fluorescence by HG 9-91-01 treatment to increase endogenous production of melanin led us to ask if a direct injection of synthetic melanin could further

improve the signal-to-noise ratio even more dramatically. While Liu *et al.* focuses on the photothermal effects of melanin for cancer treatments, we used their technique of synthesizing melanin and applied it as a methodological improvement of endogenous oocyte fluorescence. Melanin is a useful molecule due to its wide range of absorbance as well as its linear relationship to log of the concentration (Figure 3.4A and 3.4B). Using their method, we synthesized two sizes of melanin averaging 220 nm and 500 nm as determined by dynamic light scattering (Figure 3.4C). We used the 220 nm melanin particles because at larger sizes, injection is not possible as the injection pipette clogs.

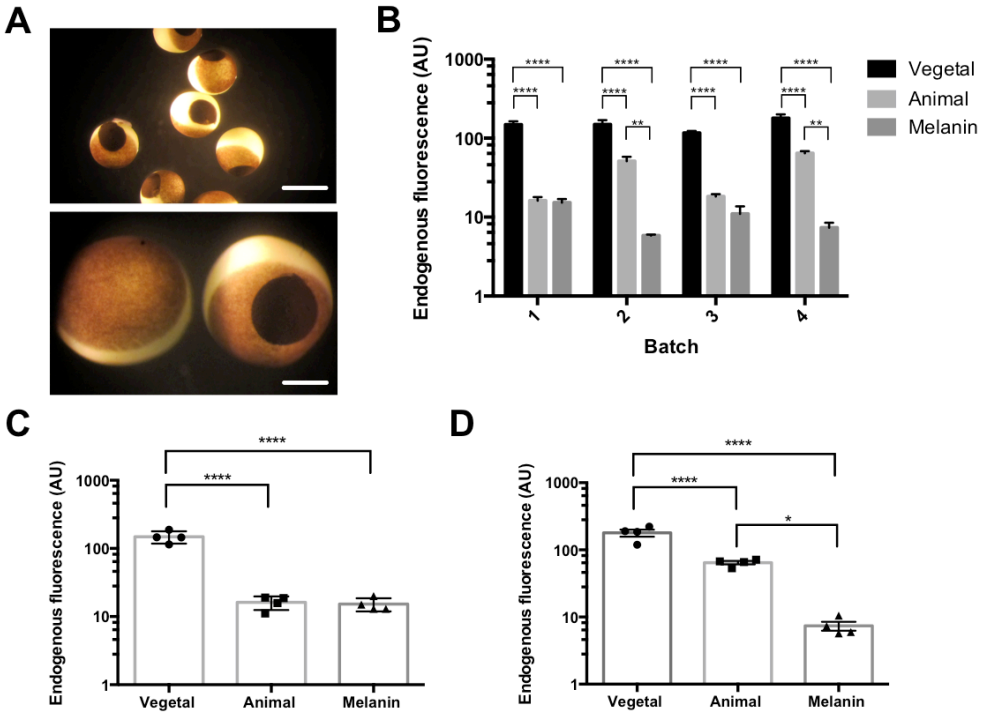

Figure 3.5. Synthetic melanin injections significantly improve fluorescence recording conditions **A)** Representative *Xenopus laevis* oocytes injected with 50.1nl of 30 mg/mL melanin. Scale bars: top 1 mm, bottom 0.3 mm **B)** Improvement of endogenous background fluorescence of four separate batches of oocytes at 535 nm. Batch 1: n=4, Batch 2: n=6, Batch 3: n=10, Batch 4: n=4. A two-way ANOVA with a *post hoc* Tukey's multiple comparisons' test (*) $P < 0.05$, (**) $P < 0.01$, (***) $P < 0.001$, (****) $P < 0.0001$. **C)** The improvement in endogenous background fluorescence in "dark" oocytes, <20 AU at 535 nm (vegetal n=4, animal n=4, and melanin-injected n=4). An ordinary one-way ANOVA with a *post hoc* Tukey's multiple comparisons' test, $P<0.0001$ (****), no statistically significant difference found between animal pole and melanin. **D)** The improvement in endogenous background fluorescence in "light" oocytes, >20 AU at 535 nm (vegetal n=4, animal n=4, and melanin-injected n=4). An ordinary one-way ANOVA with a *post hoc* Tukey's multiple comparisons' test, $P < 0.0001$ (****), and $P < 0.05$ (*). For further statistical information see supplemental statistics table appendix.

We injected each oocyte with 30 mg/mL of melanin in 50.1 nL per oocyte in various regions. The injection of melanin is done superficially, creating a disc of melanin, approximately 0.5 mm in diameter near the surface of the oocyte (Figure 3.5A bottom). Injecting melanin at either the vegetal or animal pole reduces the endogenous fluorescence. For the remaining experiments, we injected the melanin specifically on the animal pole (Figure 3.5B). We find that depending on the intrinsic absorbance of oocytes, injecting the melanin into the animal pole can decrease the endogenous fluorescence. In the darker batches of oocytes, the melanin disc has comparable or slightly decreased fluorescence with reference to the fluorescence of the animal pole (Figure 3.5C). In lighter batches, (Figure 3.5D) the fluorescence of the melanin was significantly lower than that of the animal pole. Therefore, across all batches of oocytes, we can inject synthetic melanin to make fluorescence recordings feasible. To see how this method affects the oocytes in an experimental scheme, we co-injected the melanin in a lighter batch of oocytes (Figure 3.5D) with mRNA for ASAP-Y (Lee and Bezanilla, 2017), a genetically encoded voltage indicator (GEVI) (Figure 3.6). We chose to attempt these experiments in lighter oocytes to see how well the melanin improves the signal. To investigate if the voltage dependent signal was improved, the oocytes were depolarized to 160 mV for 80 ms (Figure 3.6A). Based on previous experiments, the largest signal is generated at 160 mV and could best demonstrate the effect of melanin on signal size (Figure 3.6B).

The melanin does not alter the expression of the GEVI as we see no change in the amount of charge or statistically significant change in the amount of fluorescence when at a holding potential of -60 mV (Figure 3.6C and D), but we see a large optical improvement of approximately twice as large for the $\Delta F/F$ (Figure 3.6E and F). This indicates that by decreasing the endogenous fluorescence, we were able to achieve an overall larger ASAP-Y signal.

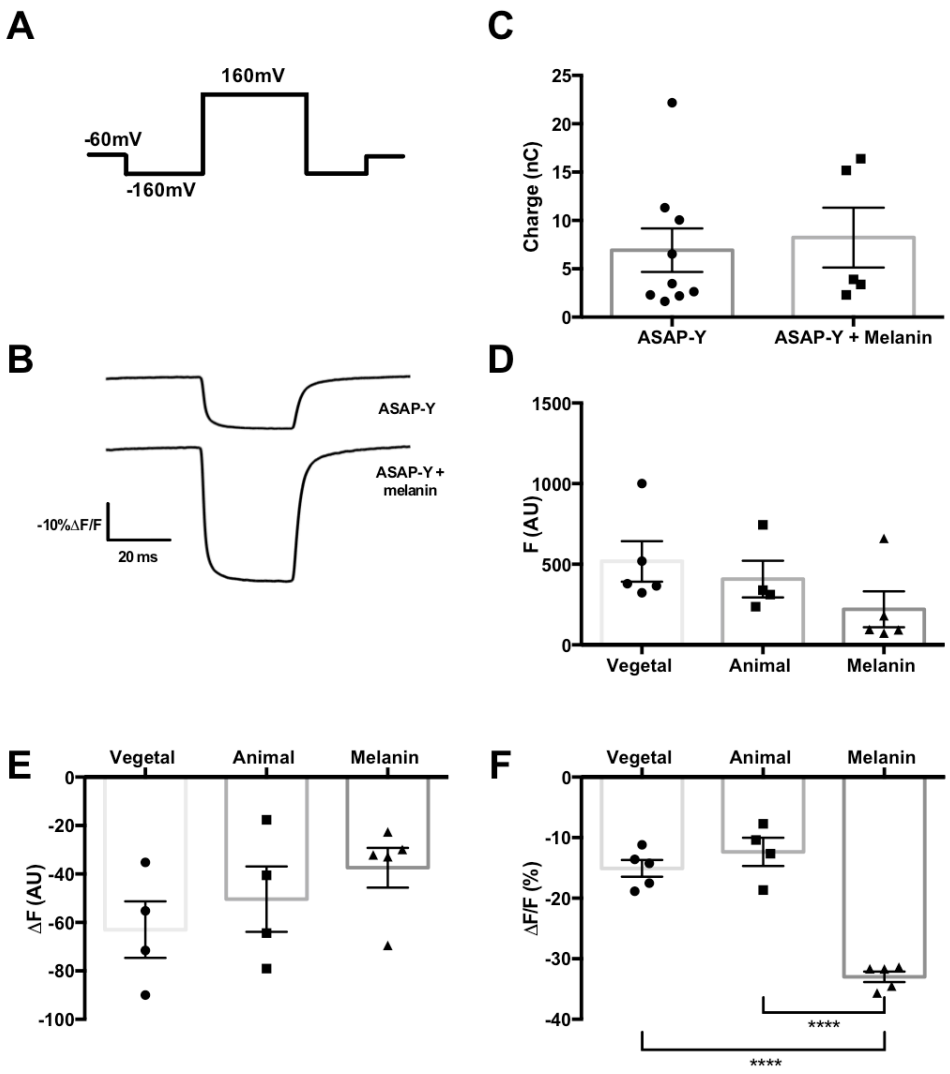

Figure 3.6. Synthetic melanin injections improve the signal of ASAP-Y
A) Pulse protocol for ASAP-Y fluorescence, where the oocytes were held at -60 mV with a 50 ms pre-pulse to -160 mV, a 30 ms pulse to 160 mV and a post-pulse back to -160 mV for 50 ms before returning to holding **B)** A representative trace of fluorescence data of ASAP-Y (top) and ASAP-Y and melanin (bottom) with the pulse protocol from A) **C)** Comparisons of levels of expressions in ASAP-Y (n=9) and ASAP-Y and melanin (n=5) injected oocytes. Unpaired two-tailed t test showed no statistical significance P=0.7365 **D)** Comparison of background fluorescence at a holding potential of -60 mV in ASAP-Y (vegetal n=5, animal n=4) and ASAP-Y and melanin (n=5). Ordinary one-way ANOVA with a *post hoc* Tukey's multiple comparison test finds no statistically significance difference between the three conditions. **E)** Comparisons of fluorescence signal in ASAP-Y (vegetal n=5, animal n=8) and ASAP-Y and melanin (n=5) co-injected oocytes. Ordinary one-way ANOVA with a *post hoc* Tukey's multiple comparison test finds no statistically significance difference between the three conditions. **F)** Comparisons of ASAP-Y injected oocytes ΔF/F % (vegetal n=5, animal n=4, and melanin-injected n=5). Ordinary one-way ANOVA with a *post hoc* Tukey's multiple comparison test find P<0.0001 (****). For further statistical information see supplemental statistics table appendix.

Discussion

The melanin layer located under the plasma membrane acts as barrier for the endogenous fluorescence when doing fluorescence recordings from the animal pole in *Xenopus* oocytes. This endogenous fluorescence varies by batch due to variability in the intrinsic production of melanin (Figure 3.1). This variability can limit opportunities to perform fluorescence recordings if the oocytes have too high endogenous background fluorescence. The studies presented here introduce two different methods to improve fluorescence recording conditions. One method increases production of the endogenous melanin whereas the second method injects synthetic melanin directly into the oocyte. Both methods significantly decrease in the background fluorescence and thus improve conditions to acquire fluorescence recordings in batches of lighter oocytes. We have also found that this extra melanin helps in reducing the increased background fluorescence resulting from staining an oocyte with a fluorophore intended to be conjugated to a particular site in an expressed membrane protein. This effect is shown when we stained the oocyte with ATTO 425 and found that the increase in background fluorescence induced by the dye was 3.8 times larger than the intrinsic fluorescence while, in contrast, the observed increase after HG 9-91-01 injection was only 2.8 times larger (Figure 3.3E and G). Many dyes partition in the membrane and remain there even after extensive wash and this is the case for ATTO 425. In principle, if the dye is only in the membrane one would not expect that an increase in melanin would be advantageous. However, there are at least three possible scenarios where the increase in melanin would help in decreasing the extra fluorescence of stained oocytes. First, some dye may penetrate, second, there might be energy transfer from the membrane to the endogenous fluorophores and third, the extra fluorescence from the dye in the membrane may be reflected (scattered) by the cytoplasm.

As the treatments presented here do not affect the expression of the protein under study, the improved recording conditions allows for significant increases in the efficacy and efficiency of oocyte experiments. Future studies may be needed to see possible effects of either HG 9-91-01 or melanin on internal second messengers such as but not limited to calcium or cAMP. These treatments eliminate the need to discard batches of oocytes if they have high endogenous fluorescence. Furthermore, it demonstrates the feasibility of improving signal-to-noise ratio in fluorescence recordings by a pharmacologic method and argues for the investigation of other pharmacologic methods with the potential to lower endogenous background. These methods could allow for the resolving of signals that were too small to be previously seen as well as permit an exploration of kinetics. The method of injecting melanin could potentially also improve the study of proteins that preferentially express in the vegetal pole, such as GIRK5 and IP_3R in unfertilized oocytes. (Díaz-Bello et al., 2013; Kume et al., 1993; Sindelka et al., 2018). Moreover, it is possible for this method to be applied to other experimental systems where endogenous fluorescence is a systematic problem such as total internal reflection microscopy, single-molecule tracking, and fluorescence resonance energy transfer studies.

Methods

Oocyte Preparation

Oocytes were harvested from *Xenopus laevis* in accordance with experimental protocols approved by the University of Chicago Animal Care and Use Committee. Following collagenase digestion of the follicular membrane, oocytes are stored at 18°C in standard oocyte solution, 96 NaCl, 2 KCl, 1.8 $CaCl_2$, 1 $MgCl_2$, 10 HEPES, at pH 7.4 with 10 mg/L of gentamicin. Oocytes were typically injected 1-2 days post digestion.

Molecular biology

ASAP1 for *Xenopus laevis* expression was created from the pcDNA3.1/Puro-CAG-ASAP1 which was a gift from Michael Lin (Addgene plasmid # 52519) (St-Pierre et al., 2014). ASAP-Y was identical to ASAP1 with an additional point mutation at L158Y (Lee and Bezanilla, 2017). Using site-directed mutagenesis by polymerase chain reaction, we added L158Y to this construct and verified it via sequencing.

Shaker cRNA that had been previously synthesized using the mMESSAGE mMACHINE T7 transcription kit (Life Technologies). Shaker W434F M356C was made on the Shaker Δ6-46 W434F background (Perozo et al., 1993) using the QuikChange II site directed mutagenesis kit (Agilent) with primers purchased from Integrated DNA Technologies. DNA was linearized using NotI (New England Biolabs).

For oocyte expression, DNA was prepared using the NucleoSpin Plasmid kit (Macherey-Nagel, Bethlehem, PA) and linearized with XbaI (New England Biolabs, Ipswich, MA). Linearized cDNA was transcribed to RNA with the mMESSAGE mMACHINE Sp6 kit (Life Technologies, Carlsbad, CA). Oocytes were injected with 50 ng of RNA and incubated at 18°C

in solution containing (in mM) 96 NaCl, 2 KCl, 1.8 $CaCl_2$, 1 $MgCl_2$, 10 HEPES, at pH 7.4 with 10 mg/L of gentamicin. Recordings were made 1-2 days following injection.

Electrophysiology and fluorescence

Simultaneous recordings of gating currents and fluorescence responses were performed using the cut-open oocyte voltage-clamp technique (Stefani and Bezanilla, 1998) in combination with a photodiode to measure temporal changes in fluorescence emission (Cha and Bezanilla, 1998). Gpatch, an in-house program, controlled an SB6711 digital signal processor-based board (Innovative Integration, Simi Valley, CA) with an A4D4 board (Innovative Integration, Simi Valley, CA). Oocytes were held under voltage-clamp with a Dagan CA-1B amplifier (Minneapolis, MN) and current was filtered at 5 kHz. ASAP-Y was sampled at 50 kHz and fluorescence emissions were collected through an Olympus LUMPlan FL N 40X/0.8 NA water-immersion objective by a PIN-020A photodiode (UDT Technologies, Torrance, CA), amplified by a patch clamp amplifier L/M-EPC-7 by LIST Medical Electronic (Darmstadt, West Germany) with a filter of 10 kHz, and then integrated over each sampling period using a home-built integrator circuit. ASAP-Y was excited via a ThorLabs LED controller powering a 470 nm LED (ThorLabs, Newton, New Jersey) that was passed through a filter cube housing a 480/40 excitation filter, a 505 long-pass dichroic, and a 535/50 emission filter (Chroma, Bellows Falls, VT). For oocytes stained with ATTO-425 excitation was performed with a mounted 420 nm LED (ThorLabs) reflected by a 455 nm long-pass dichroic (Chroma) through a 40X water-immersion objective (LUMPlan FL N, Olympus); emission was collected through the dichroic and a 475 nm long-pass filter (Chroma). All recordings were performed at around 18°C, with an external solution containing (in mM) 115 N-methyl-D-glucamine neutralized with methanesulfonic acid (NMG/MES), 10 HEPES, and 2 $Ca(OH)_2$ and an internal solution

containing (in mM) 115 NMG-MES, 10 HEPES, and 2 EGTA. Both solutions were set to pH 7.5. Microelectrodes were pulled on a Flaming/Brown micropipette puller (Sutter Instruments, Novato, CA, model P-87) and were filled with 3 M $CsCl_2$ and had a resistance of ~0.2–0.8 MΩ.

The labeling solution consisted of depolarizing solution comprised of 120 mM KCl, 2 mM $CaCl_2$ and 10 mM HEPES at pH 7.4 with 20 μM ATTO 425 maleimide (ATTO-TEC, Siegen, Germany) . Oocytes were maintained in the solution on ice for at least fifteen minutes and removed and washed in standard oocyte solution 5-20 minutes before recordings were performed.

Chemical biology

HG 9-91-01 (MedChem Express) was dissolved in DMSO to create a stock solution of 200 mM. Then with 200 µM aliquots diluted with RNAse free water (Ambion), HG 9-91-01 was injected at stated concentrations in the paper. When used with cRNA, HG 9-91-01 was mixed and co-injected. For example, the 200 µM HG 9-91-01 was mix 1:1 with 2000 ng/µl cRNA of non-conductive Shaker constructs for injecting 100 µM. DMSO concentration when injected into the oocyte was less than 0.1%. Since the volume of an oocyte is approximately 1uL and we inject 50.1nl, the final concentration of HG 9-91-01 inside the oocyte is approximately 4.7 µM.

For synthesis of synthetic melanin with an average of diameter of 200 nm, 3 mL of ammonia aqueous solution (NH_4OH, 28-30%, Sigma) was mixed with 40 mL of 200 proof ethanol (Decon Laboratories, Inc.) and 90mL of milliQ water with mild stirring at 30°C for 30 minutes. 0.5 g of dopamine hydrochloride (Sigma) was dissolved in 10 mL of milliQ water and injected into the above solution. The color of the solution immediately turns pale yellow and quickly darkens to a brown. The reaction was left at room temperature for 24 hours. The melanin mixture was centrifuged and rinsed with copious amounts of MillQ water. To create different

concentrations the melanin was dried and weighted and resuspended in RNAase free water (Ambion) before injection.

Melanin Characterization

Absorbance measurements was measured on Cary 60 UV-Vis (Agilent technologies, Wood dale IL). Dynamic light scattering (DLS) was done on a Dynapro Nanostar (Wyatt Technology, Santa Barbara, CA) of an unfiltered 30 mg/mL sample of synthetic melanin. We took 10ul aliquots of synthetic melanin and measured in ten 5-s acquisitions. We used the globular proteins model for calculating the radius with a Rg Model of Sphere.

Statistical analysis.

See Appendix. Tables A-S, refer to the results from the indicated statistical tests performed on data presented in Figure 1B, 1C, 2B, 2C, 2D, 3A, 3B, 3E, 3F, 3G, 3H, 3I, 4B, 5C, 5D, 6C, 6D, 6E, 6F of the main text, respectively. Statistical significance of oocyte endogenous fluorescence by batch variance was established by ordinary one-way ANOVA with a *post hoc* Tukey's multiple comparisons test (A-B). To establish a lack of statistical significance between uninjected and DMSO injected oocytes we used an ordinary one-way ANOVA with a post-hoc Holm-Sidak multiple comparison test. Within batches there was no significant difference (C). To establish the statistical significance of the effect of HG 9-91-01 on background fluorescence of the oocyte, we used an ordinary one-way ANOVA with a *post hoc* Holm-Sidak (D), Dunnett (E), and Bonferroni (H) multiple comparison test. To establish the effect of HG 9-91-01 on the labeling of oocytes we first showed that HG 9-91-01 significantly decreases the endogenous fluorescence using an unpaired two-tailed t test (F). Then also using an unpaired two-tailed t test showed the difference post ATTO 425 labeling in uninjected and HG 9-91-01 injected oocytes (G). Statistical significance of the effect of HG 9-91-01 on gating charge (I), labelled background

fluorescence (J), ΔF (K), and ΔF/F% (L) was established using an unpaired two-tailed t test. Statistical significance of the effect of melanin injection on background fluorescence was established by an ordinary two-way ANOVA with a *post hoc* Tukey's multiple comparison test in several batches (M). Statistical significance of the effect of melanin injections on background fluorescence was established an ordinary one-way ANOVA with a *post hoc* Tukey's multiple comparison test for batches of darker oocytes (N) and lighter oocytes (O). Statistical insignificance of melanin injection on the amount of gating charge was demonstrated by an unpaired two-tailed t test (P). Statistical significance of the effect of melanin injection on F (Q), and ΔF (R), and ΔF/F% (S) of ASAP-Y was established with an ordinary one-way ANOVA with a *post hoc* Tukey's multiple comparison test. DoF refers to degrees of freedom, n is the number of oocytes. ns indicates a not statistically significant P value. (*) $P < 0.05$, (**) $P < 0.01$, (***) $P < 0.001$, (****) $P < 0.0001$.

Data Analysis and Figures

Data analysis and figures were made with Prism 6.0 (GraphPad Software, La Jolla, CA, USA) and Analysis (in-house program)

Chapter 4 - The Trajectory of Discrete Gating Charges During Activation and Deactivation in a Voltage-Gated Potassium Channel

Note: The following section is excerpted from 'The trajectory of discrete gating charges during activation and deactivation in a voltage-gated potassium channel', a manuscript in preparation by Michael F. Priest, Elizabeth E.L. Lee, and Francisco Bezanilla, with figure renumbering, reference reformatting, and combining of supplemental information into the main text. E.E.L. Lee and M.F. Priest contributed equally to this manuscript in preparation.

Abstract

Voltage sensor movement in voltage-gated ion channels remains debated, and studies of the motions of discrete gating charges in the voltage sensor have proven difficult. To overcome these challenges, we optically tracked the movement of charged residues using a positively-charged bimane derivative (qBBr) that is strongly quenched by tryptophan. Through the addition of tryptophans along the potential activation pathway, we have mapped a vertical translocation and rotation of gating charges R1 and R2. This method maps transitions from the active or relaxed state to the resting state and we have observed a difference in the path of activation from deactivation. Further, qBBr interactions suggest that a crucial component of the hydrophobic plug is linked to the Cole-Moore shift by its interaction with R1. This approach appears readily extendable to additional voltage-gated membrane proteins, such as the *Ciona intestinalis* voltage sensitive phosphatase (CiVSP).

Introduction

The nature of the motion of the voltage sensor in voltage-gated ion channels has been a subject of intensive research. This motion is largely driven by the individual positively-charged amino

acids, typically arginines, that are found on the fourth transmembrane segment (S4) of each monomer of the tetrameric channel. The number of charged amino acids driving this motion varies from channel to channel, but has been shown to consist of the four most extracellular arginines in the canonical voltage-gated Shaker potassium channel(Aggarwal and MacKinnon, 1996; Seoh et al., 1996). However, research into the motion of these individual gating charges has suffered from experimental limitations. Cross-linking studies replace residues with cysteines or histidines to see which residues interact with each other in different conformational states, necessarily abrogating the positive charge of any gating charge if they are examined directly (Broomand et al., 2003; Henrion et al., 2012; Lainé et al., 2003). Similarly, site directed fluorometric approaches typically replace a residue with a cysteine and then attach a neutrally-charged fluorescent dye, providing the additional advantage of being able to monitor conformational changes in real-time (Cha and Bezanilla, 1997; Mannuzzu et al., 1996; Priest and Bezanilla, 2015). Positively charged adducts such as methanethiosulfonate-ethyltrimethylammonium (MTSET) linked to cysteines placed at gating charges can be used to replace the positive charge and characterize discrete gating charges (Ahern and Horn, 2004, 2005; Baker et al., 1998; Larsson et al., 1996). However, these replacement charges cannot be rapidly monitored, limiting their use for examining conformational changes.

Ideally, one would like to follow the movement in real time of individual gating charges as they respond to changes in the electric field. To this end one would require a fluorophore that is comparable to the gating arginines. We used monobromo(trimethylammonio)bimane (qBBr), a small molecule fluorescent dye with a permanent positive charge (Figure 4.1A). While bulkier than an arginine (MW≈295 versus 101) (Figure 4.1B), modelling the conjugation of qBBr to a cysteine substituted into the two most extracellular gating charges in a Shaker-type voltage-gated

potassium channel (R362/R1 and R365/R2) (Chen et al., 2010; Pettersen et al., 2004) provided a distance between the carbon backbone and the positive charge of qBBr of ~5.5 Å, very close to the analogous distance of ~5.3 to 6.5 Å for arginine. Therefore, qBBr attached to a cysteine at the endogenous position of the gating charge may mimic the positive gating charge. In addition to being positively charged, qBBr has useful fluorescence quenching properties. Tryptophan has been shown to strongly quench qBBr fluorescence, with weak quenching by tyrosine, and no quenching from various other amino acids including histidine, phenylalanine, methionine, aspartate, or arginine (Mansoor et al., 2010). This phenomenon of 'tryptophan-induced quenching' in bimane dyes generally (Mansoor et al., 2002), together with their remarkable environmental insensitivity (Mansoor et al., 1999), has been taken advantage of to measure conformational rearrangements of various membrane proteins, including the β2-adrenergic G protein-coupled receptor (Yao et al., 2006), a cyclic nucleotide-gated ion channel (Islas and Zagotta, 2006), the BK channel (Semenova et al., 2009), a bacterial proton-gated ion channel (Menny et al., 2017), and a bacterial lactose permease (Smirnova et al., 2014). In general, these studies use the fluorescent quenching produced by an interaction between bimane and a particular tryptophan, whether native or engineered into the protein, to provide insight into how the protein moves during conformational transitions.

Here, we perform site-directed voltage-clamp fluorimetry on qBBr-bound Shaker voltage-gated potassium channels expressed in *Xenopus laevis* oocytes. By substituting a cysteine for a native gating charge and then covalently attaching qBBr to this site, we produce a fluorescent mimic of a discrete charge in the voltage sensor of the channel. Individual native or engineered tryptophans in the channel are then used to quench the fluorescence of the charged qBBr as it moves in response to changes in membrane potential. We used this system to

investigate the pathway taken by the two most extracellular-facing arginines during activation and deactivation, as well as to examine the effect of the relaxed state (Lacroix et al., 2011; Villalba-Galea et al., 2008) on these individual gating charges. In general, the movement of R1C-qBBr followed a translation and rotation, while R2C-qBBr followed a translation, giving new information on the trajectories that have been inferred from recent consensus models on the motion of the voltage sensor (Li et al., 2014; Vargas et al., 2011, 2012). Of particular interest, during channel activation R1C-qBBr does not appear to interact with F290W, the most intracellular residue of the hydrophobic plug (Chen et al., 2010; Lacroix and Bezanilla, 2011) and putative gating charge transfer center (Tao et al., 2010b), suggesting that R1 does not normally move past the hydrophobic plug and may provide the basis of the Cole-Moore shift because R1 only interacts with F290W at extremely negative potentials. This technique should also be transferrable to other voltage-sensing membrane proteins; as a proof of principle, we demonstrate its use in the voltage-sensitive phosphatase CiVSP.

Results

The basic principles of qBBr gating charge tracking in time

The idea of the present approach is to study the trajectory and kinetics of translocation of the gating charge (now a fluorophore, qBBr) as the membrane potential is changed by taking advantage of the specific quenching of qBBr by a tryptophan (W) that is positioned nearby or in the path of qBBr.

If we were tracking fluorescence at the single molecule level, the fluorescence signal we would observe would depend on the position of the W with respect to the moving qBBr. Let us assume that we are applying a positive voltage to activate the voltage sensor that moves between two discrete positions. We can distinguish three extreme cases schematically (Figure 4.1C, left

panel). If the W is near the resting position of the qBBr, we would see a sudden increase in fluorescence when the qBBr moves away from it and the time lag before that increase corresponds to the waiting time of the sensor before it jumps across the energy barrier (Figure 4.1C, left panel, top trace). On the other hand, if the W is in the path of qBBr (Figure 4.1C, left panel, middle trace), we would see an extremely brief decrease of fluorescence as the qBBr passes by the quenching group. Finally, if the W is near the final position of the qBBr (Figure 4.1C, left panel, bottom trace) we would see a sudden decrease in fluorescence that would be maintained when the qBBr reaches that point. The duration of the high fluorescence period is the waiting time before the sensor crosses the energy barrier.

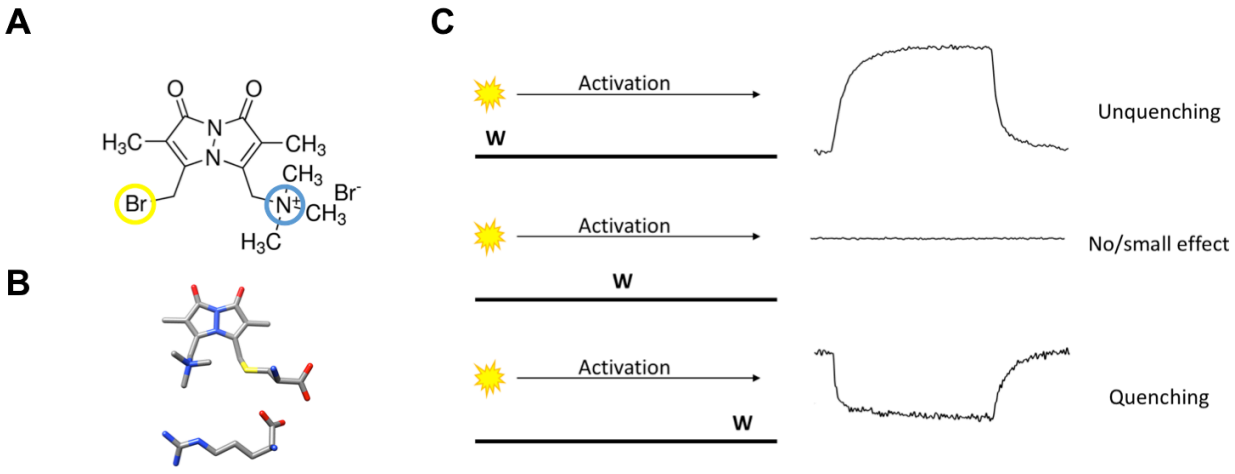

Figure 4.1 Experimental setup using qBBr
A) Chemical structure of monobromo(trimethylammonio)bimane, a small positively charged (blue) fluorophore with the ability to conjugate to cysteine (yellow). **B)** Size comparison of qBBr-Cys (top) to an arginine (bottom). Nitrogen (blue), oxygen (red), sulfur (yellow), carbon (grey). **C)** Cartoon schematic of qBBr mechanism with representative fluorescence data for unquenching (top), no effect (center), and quenching (bottom).

However, since we are looking at a large ensemble of molecules the macroscopic fluorescence signals we see are the result of an ensemble of VSDs moving, each one at a different time according to its first latency duration, generating a continuous change in

fluorescence. The fast event for the case of a W in the middle of the qBBr path would not be visible in the ensemble because the crossing of the VSDs is unsynchronized and if it is exactly in the middle no signal will be seen (Figure 4.1C, right panel, middle trace). The other two extreme cases will generate a continuous quenching or unquenching depending on the placement of the tryptophan (Figure 4.1C, right panel, top and bottom traces).

A simple model of quenching of qBBr by W is

$$F(t) = F_0\left[1 - \exp\left(-\frac{d}{\lambda}\right)\right]$$

where $F(t)$ is qBBr fluorescence, F_0 is the maximum qBBr fluorescence (no quenching), d is the distance from qBBr to W and λ is the characteristic distance for quenching, Now, we assume that qBBr moves in a trajectory represented by x between the initial position, x_0, and the final position, x_f, and W is located somewhere in the x axis, x_W. Let us consider first that qBBr moves between two states and define $P_0(t)$ and $P_f(t)$ as the probabilities that qBBr is in x_0 and x_f respectively. Then, $P_0(t) + P_f(t)=1$ and we can write the time course of the fluorescence as

$$\frac{F(t)}{F_0} = P_0(t)\left[\exp\left(-\frac{|x_W - x_f|}{\lambda}\right) - \exp\left(-\frac{|x_W - x_0|}{\lambda}\right)\right] + 1 - \exp\left(-\frac{|x_W - x_f|}{\lambda}\right)$$

This means that the time course of fluorescence will have the time course of $P_0(t)$ and will not depend on the position of W in the trajectory.

If we now assume that the number of states is more than 2, say i=1,2,3,… n, we can write a general solution for the fluorescence

$$\frac{F(t)}{F_0} = \sum_{i=1}^{n} P_i\,(t)\left[1 - exp\left(-\frac{|x_i - x_W|}{\lambda}\right)\right]$$

$P_i(t)$ will have *n-1* eigenvalues, so the time course of fluorescence will now depend on the position of W in the trajectory, because $P_i(t)$ will be weighted by the exponential term that includes the distance to each position. In fact, when one simulates this case with 3 or more states, the time course of the fluorescence is generally biphasic (shows increases and decreases) during the depolarization, as might be expected because as it traverses its trajectory the qBBr will go through periods that it will be closer to the W and others when it will be further away. This is a prediction that will be important in interpreting the experimental results.

qBBr mimics a native gating charge

While qBBr crucially contains a permanent charge (Figure 4.2A) like the arginines that constitute the gating charges in the Shaker voltage-gated potassium channel, this is not a guarantee that the voltage sensor will continue to behave normally with a fluorescent dye substituted for a gating charge. To test whether this was the case, we first separately mutated the first and second most extracellular gating charges (R362/R1 and R365/R2) in a non-conducting (W434F), non-fast inactivating (Δ6-46) Shaker channel to cysteines. Following expression of these constructs in *Xenopus laevis* oocytes, qBBr was conjugated to either of these charges by incubation of the oocytes in a depolarizing solution containing qBBr. Oocytes containing qBBr conjugated to R1C or R2C were then simultaneously recorded optically and electrophysiologically using the cut-open oocyte voltage clamp technique. In both cases, the observed gating currents are likely a combination of voltage sensors that have been labeled with qBBr and unlabeled voltage sensors that retain a bare cysteine. For R1C-qBBr, gating currents appeared to be faster than those of the wild type channel but still comparable in voltage sensitivity (Figure 4.2A, 4.2B). With R2C-qBBr, gating currents were also more rapid,

with voltage sensor movement beginning at more hyperpolarized potentials than in the wild-type channel and producing a very shallow Q-V curve (Figure 4.2A, 4.2B). The gating currents here reflects both labeled and unlabeled channels. Unlabeled R2C produces a split Q-V curve, which may represent a small part of the gating currents we observe. These findings suggest that the additional bulk of qBBr may destabilize the resting state of the voltage sensor when it is conjugated to the more intracellular R2C, but not when it is conjugated to the more extracellular R1C. This is in good agreement with numerous computational models of the resting state of the voltage-gated potassium channel that suggest that R1 is less sterically inhibited in the resting state than R2 (Vargas et al., 2012). They also suggest that qBBr would act as a faithful mimic of the movement of the gating charge of R1, and should also mimic the movement of R2, albeit with energetic differences.

Upon depolarization, the fluorescence signal of R1C-qBBr decreased dramatically (Figure 4.2C, top), while the corresponding fluorescence signal of R2C-qBBr did not (Figure 4.2C, bottom). A reduction in qBBr fluorescence is likely due to the presence of a tryptophan, or possibly a tyrosine. Since the fluorescence signal is lower when the R1C-qBBr is in the active state than when it is in the resting state, the quenching residue should be near the active state of R1. Based on a homology model of a voltage-gated potassium channel crystal structure in the relaxed state (Chen et al., 2010), R1 should reside near an endogenous tryptophan (W454) at the extracellular side of S6 (Figure 4.2D). Additionally, it has been reported that R1 comes into close proximity to this region of the channel (Lainé et al., 2003).

Mutation of this tryptophan to a non-quenching alanine residue abolished the fluorescence reduction that we observed during activation (Figure 4.2E, top). Additionally, the mutation of this tryptophan to a phenylalanine also abolished the endogenous voltage-dependent

fluorescence (Figure 4.2E, bottom). However, as this mutation reduced expression, we proceeded with a W454A background. Therefore, our optical data supports the idea that upon activation R1C-qBBr comes near the pore domain, where its fluorescence is quenched by W454, while R2C-qBBr does not. These results are expected given prior combination of crystallographic and functional data and suggest that R2C-qBBr and R1C-qBBr may mimic crucial properties and the motion of the native gating charges.

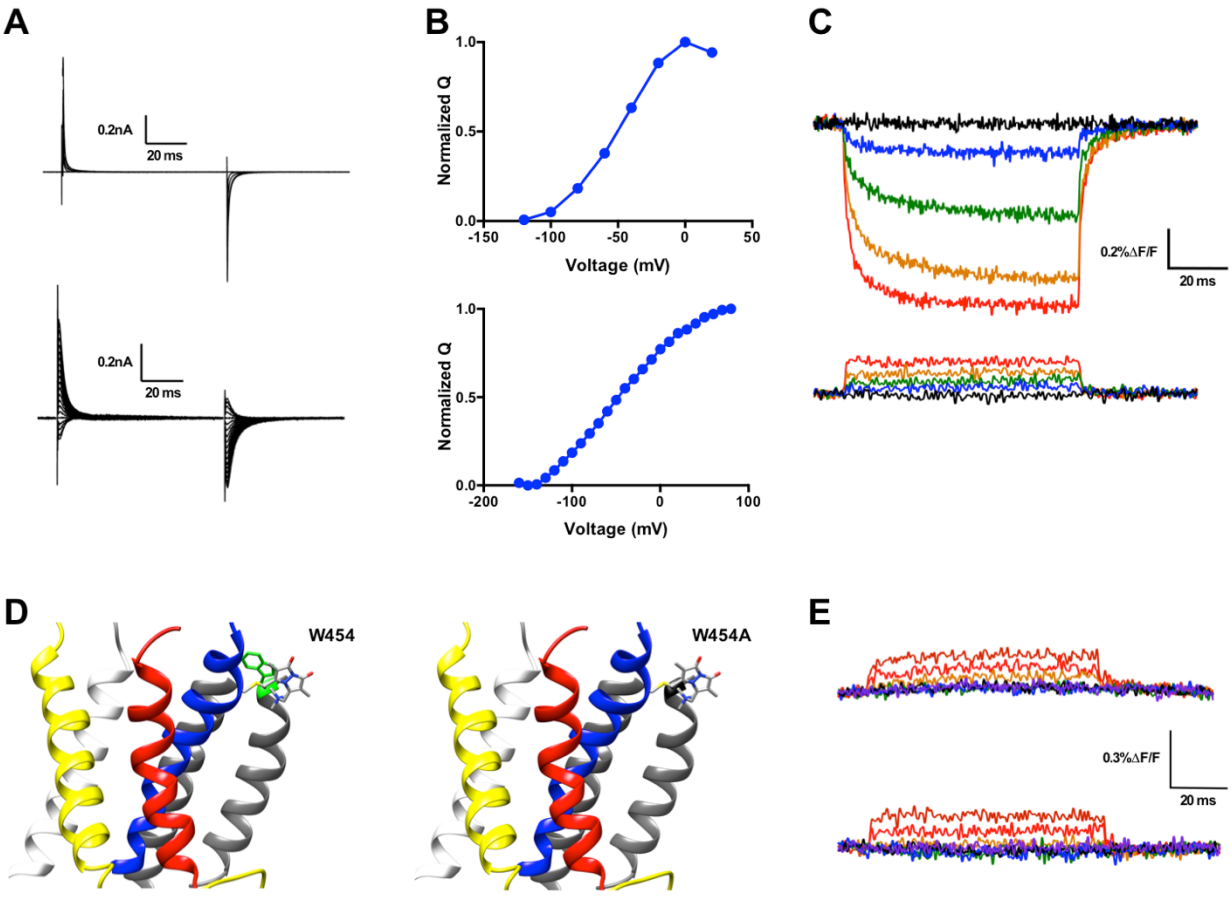

Figure 4.2 Characterization of Shaker qBBr constructs
A) Representative gating current traces of Shaker R1C-qBBr (top) and R2C-qBBr (bottom). **B)** Normalized QV curves of R1C-qBBr (top, n=2) and R2C-qBBr (bottom, n=2). **C)** Representative fluorescence traces of qBBr labeled R1C-qBBr (top) and R2C-qBBr (bottom). Here and elsewhere, membrane potentials pulsed to are as follows: brown: +80 mV, red: +40 mV, orange: 0 mV, green: -40 mV, blue: -80 mV, black: -120 mV, purple: -160 mV. **D)** Cartoon structure showing the position of the mutation 454 from a tryptophan (left) to an alanine (right) (PDB: 3LUT). **E)** Representative fluorescence traces for R1C-qBBr:W454A (top) and R1C-qBBr:W454F (bottom).

Activation pathway mapped by qBBr and tryptophan-induced fluorescence quenching

To fully map the trajectory of R1 and R2 using qBBr, we created a series of constructs based on the R1C:W454A and the R2C backgrounds. We used these two constructs as backgrounds because they showed very small and almost time-independent depolarization-induced fluorescent signals (Figure 4.2E) which we were unable to link to any endogenous tyrosine or tryptophan. This suggested that the small observed fluorescence change may come from a change in environmental state or be a readout of the changing electric field through a

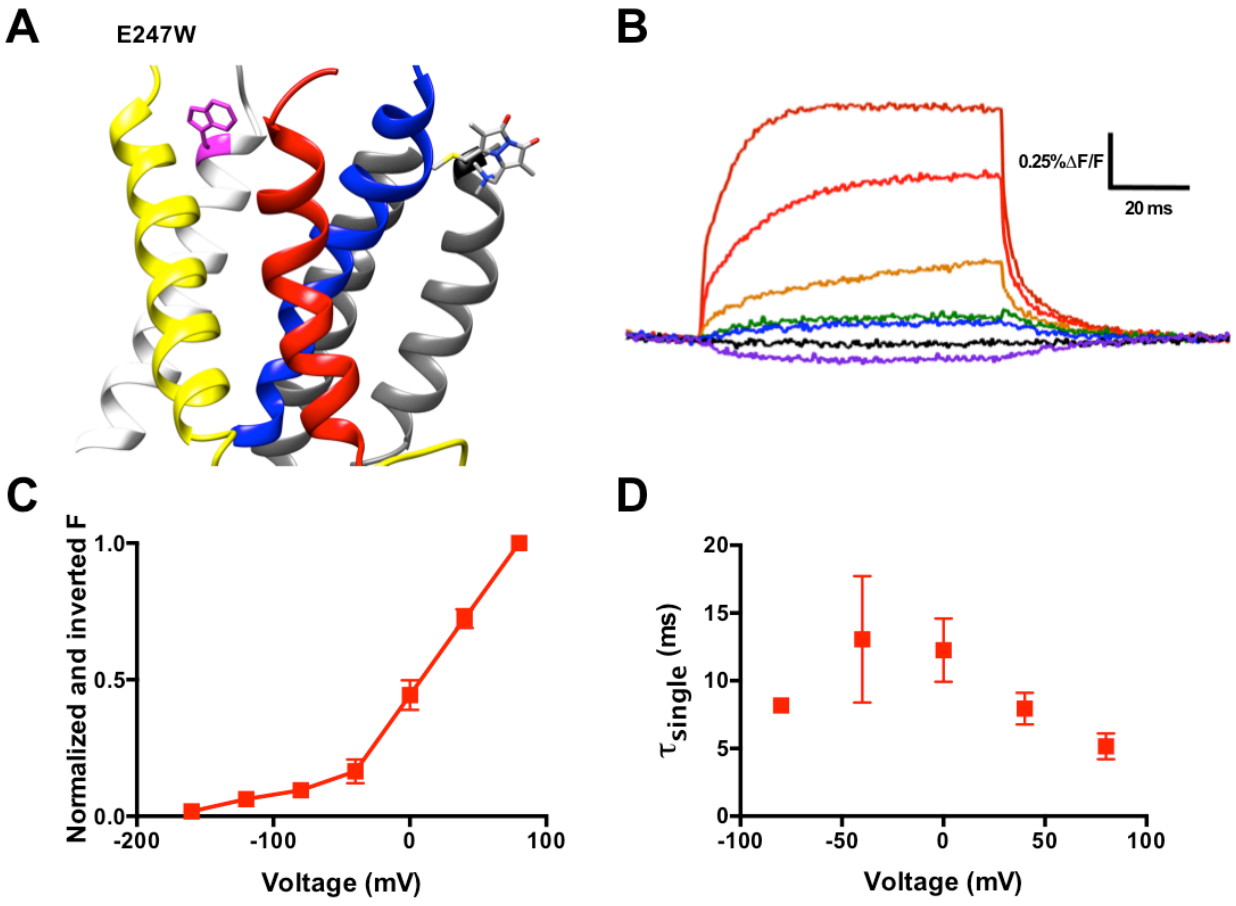

Figure 4.3 qBBr optical tracking in a Shaker construct, R1C-qBBr:W454A;E247W
A) An example Shaker construct, R1C-qBBr:W454A;E247W demonstrating the tryptophan placement within the protein (top, PDB: 3LUT) **B)** A representative activation family of fluorescence traces. **C)** A normalized and inverted FV curve **D)** A single exponential **τ** of fluorescence upon activation (n=3)

possible electrochromic effect. Because this residual fluorescence change was wholly unobservable in the presence of tryptophan-induced quenching in the R1C-qBBr:W454W construct, we hypothesized that substituting a tryptophan elsewhere into the channel would similarly alter the qBBr fluorescence signal in a way that would dominate over the residual fluorescence signal.

As an example of one of several insertions we did, Fig 4.3 shows the analysis of qBBr fluorescence signals when we inserted a tryptophan in position 247 of the R1C-W454A construct (Figure 4.3A, top). In response to changes in membrane potential, the exogenous, substituted tryptophan produced voltage-induced fluorescence changes (Figure 4.3A, bottom) that were markedly different from the background fluorescence changes of R1C-qBBr:W454A (Figure 4.2E, top)

If R1C-qBBr is closer to the tryptophan at 247 in the resting state than in the active state, we should observe an increase in fluorescence upon activation (Figure 4.3A). The experiment shows that during activation, E247W produces a clear unquenching, or increase in fluorescence, of R1C-qBBr (Figure 4.3B) . Therefore, R1C-qBBr moves away from position 247 upon activation.

Examining the fluorescence signal more closely, we see that it has many properties reflecting movement of the voltage sensor. Just as the gating currents produced by the voltage sensor are voltage-sensitive, the fluorescence signal of R1C-qBBr:W454A:E247W has a voltage-sensitive response. From our family of fluorescence traces (Figure 4.3B) we can generate a FV curve and observe the amount of fluorescence quenching or unquenching due to changes in voltage (Figure 4.3C). Moreover, the voltage-sensitivity of the fluorescence is also seen in the

kinetics of the fluorescence traces. As shown in Figure 4.3D the fluorescence has different kinetics as the voltage of the pulse is changed.

We generated numerous constructs with an exogenous, substituted tryptophan that produced voltage-induced fluorescence changes in R1C-qBBr:W454A or R2C-qBBr that were distinct from the background fluorescence changes and from each other (Figure 4.3B, 4.3C, 4.4A, 4.4B). A decrease in fluorescence upon depolarization suggests that the R1C- or R2C-qBBr comes closer to that residue during the transition from the resting to the active state, while an increase in fluorescence upon depolarization suggests that the gating charge moves away from that residue during activation (Figure 4.1B). Therefore, by pooling the data from numerous constructs, each with a single tryptophan, we can map the activation pathway of R1 and R2 (Figure 4.4A and Figure 4.5A).

Movement of R1

In response to a depolarizing pulse, R1C-qBBr fluorescence was quenched in response to the endogenous tryptophan at residue 454, as well as to a tryptophan substituted for the phenylalanine at the extracellular side of the S5 at position 416. R1C-qBBr moved away from tryptophans inserted at F244W, E247W, 320W, and T326W (Figure 4.4A, 4.4B). Interestingly, we found no appreciable changes in the fluorescence signal of F290W or L294W (Figure 4.4A, 4.4B). The small fast fluorescence signal seen for these two constructs is reminiscent of that of R1C-qBBr:W454A. In some of these recordings, we observe two-component fluorescence potentially due to the addition of the W mutation. Together, these findings map out a pathway that consists of both an intracellular to extracellular translation and a rotation (Figure 4.4B). Specifically, R1C-qBBr seems to reside near the pore domain in the active state, as observed in

the crystal structure (Chen et al., 2010). It reaches this position from a resting position that seems to reside approximately one helix turn extracellular to F290, as it shows movement away from I320W, but not from W289W, F290W, or L294W.

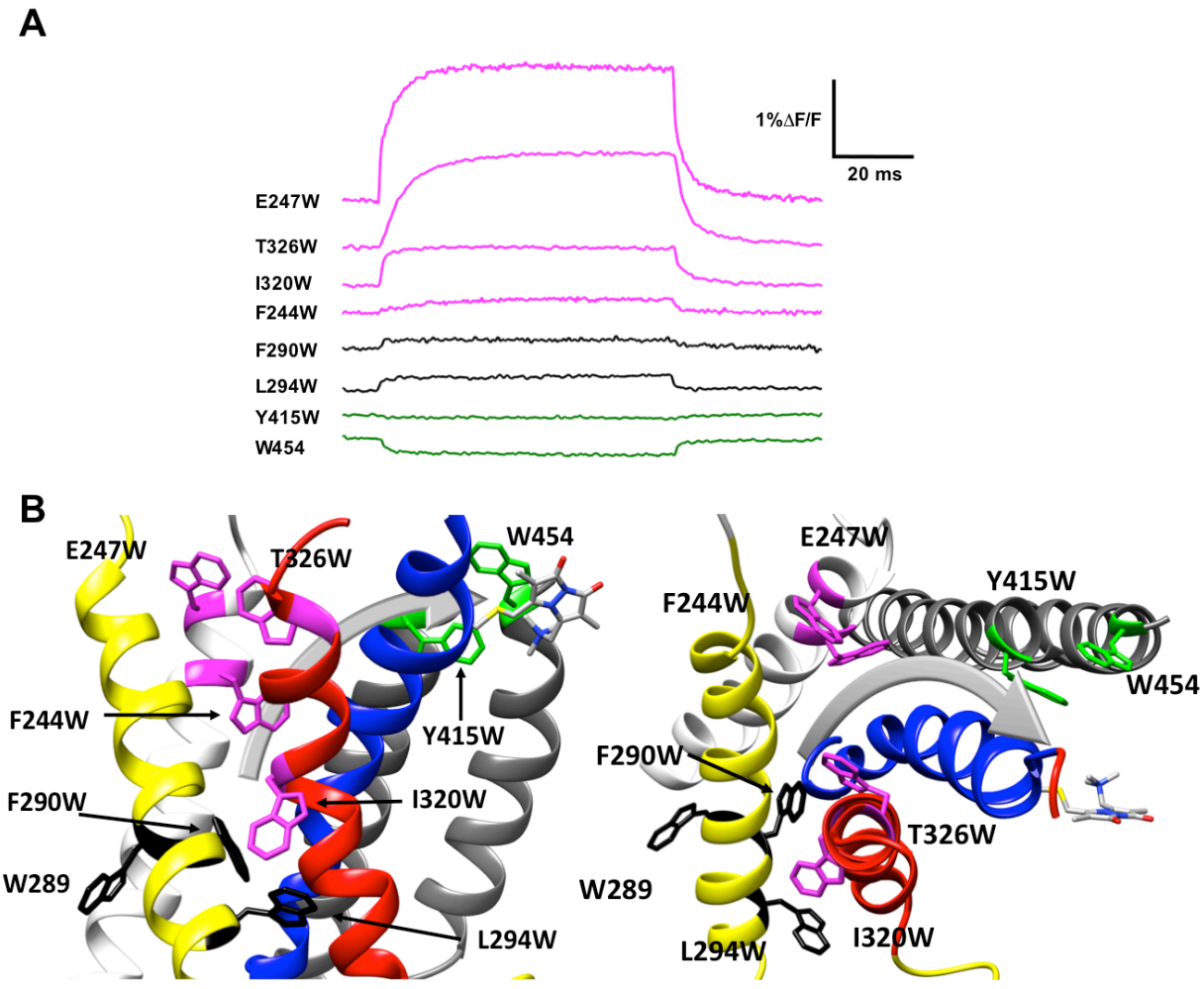

Figure 4.4 A summary of tryptophan (W) mutations used to describe the activation pathway of R1C in Shaker

A) Representative qBBr traces at +80mV. As qBBr moves closer to a W, the W quenches (green) the qBBr fluorescence (Y415W, W454). When it moves further away from a W, the qBBr fluorescence is unquenched (pink, F244W, E247W, I320W, T326W). Some W mutations have no effect (black, 289W, L294W, F290W) **B) A** summary structure of activation of R1C-qBBr. S1- white, S2 – yellow, S3 – red, S4 – blue, S5 and S6 – grey. (left). A top down view of the VSD (right). In both a path based on the tryptophan quenching/unquenching for R1C-qBBr is marked with a grey arrow (PDB: 3LUT).

Movement of R2

Substitution of W residues along the pathway of R2 reveals that upon activation R2C-qBBr moves closer to Y415W, F416W, and T326W, while moving away from I241W, F244W, I287W, and L294W (Figure 4.5A and B). Therefore, in the active state, R2C-qBBr resides between the extracellular side of the S3 and S5 segments, as quenching is observed from T326W, Y415W, and F416W. As opposed to R1C-qBBr, R2C-qBBr does not encounter the S6 segment upon activation. In the resting state, the fluorescence results suggest that R2C-qBBr is stable near F290, unquenching from a cluster of tryptophans inserted at L294, I287, and I241. As seen in R1, there is similarly a rotation in the movement of R2; however, the rotation of R2 is less evident.

Interestingly, the fluorescence responses differ qualitatively between the two gating charges for tryptophans substituted at L294, T326, and W454. Thus, qBBr mapping reveals that R1 and R2 travel distinct paths in relationship to the voltage-sensing domain during activation. Notable exceptions to this include Y415, W289, and F244, which produce similar responses from both R1C and R2C-qBBr. As it faces the lipid membrane, it is unsurprising that W289 does not quench either R1C or R2C-qBBr; however, this suggests that the S2 in which it resides is unlikely to undergo any large rotations that would expose this residue to the gating charges. Y415W quenches both R1 and R2, underscoring the activated position of both these residues near the extracellular surface of the membrane. The neighboring residue F416W quenched R2C-qBBr and did not express with R1C-qBBr. F416 has previously been shown to bridge to R1 (Conti et al., 2016; Lainé et al., 2003; Phillips and Swartz, 2010) and R2 (Conti et al., 2016).

Finally, F244 has been shown to interact with both R1 and R2 (Lacroix et al., 2012), and has been proposed to act as a critical stabilizer of the active state of the voltage sensor (Lacroix et al., 2014). Taken together, our fluorescence data shows that upon activation both R1 and R2 undergo a translation from the intracellular to the extracellular side of the membrane, together with a

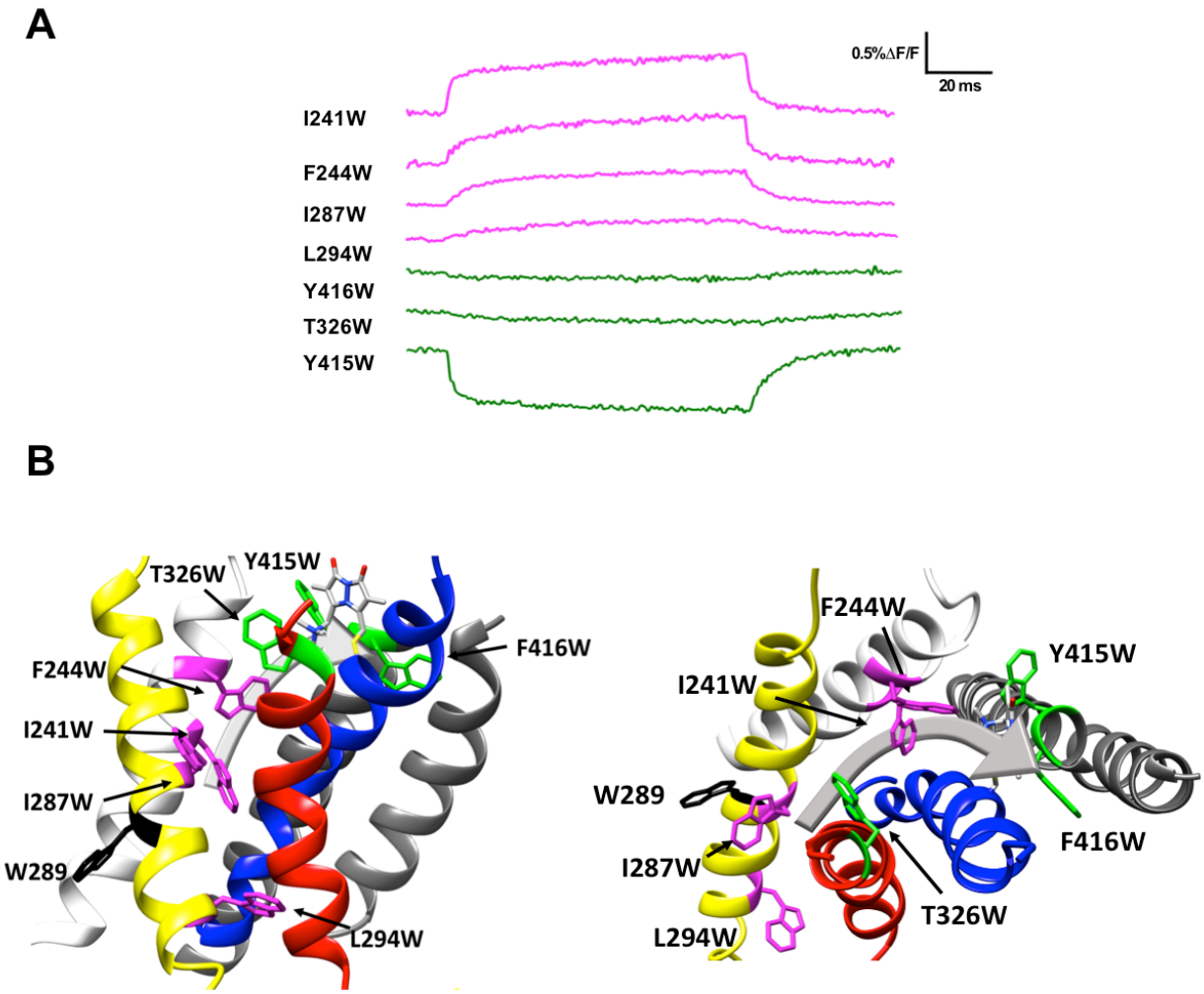

Figure 4.5 Characterization of R2C-qBBr activation
A) Representative qBBr traces at +80 mV. As qBBr moves closer to a W, the W quenches (green) the qBBr fluorescence (Y415W, T326W, Y416W). When it moves further away from a W, the qBBr fluorescence is unquenched (pink, I241W, F244W, I287W, L294W). **B)** A summary structure of activation of Sh R2C-qBBr (left). A top down view of the VSD (right) In both an approximate path that follows the W-induced quenching/unquenching for R2C-qBBr is marked with a grey arrow (PDB: 3LUT).

rotation (Figure 4.4B and 4.5B). The discrete and unique pathways mapped out by these charges provide new levels of clarity into how these charges move distinctly from each other.

The VSD path of deactivation differs from that of activation

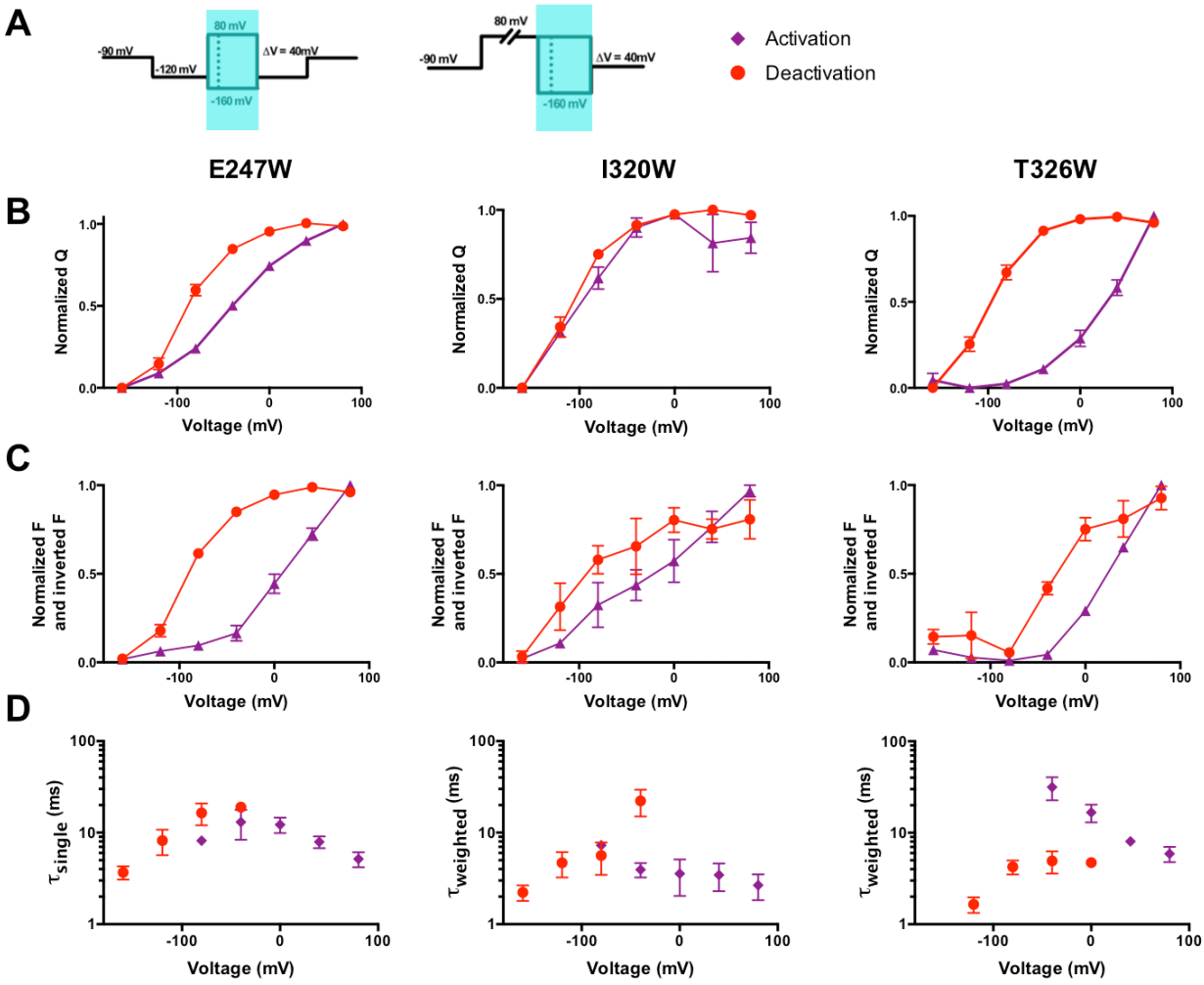

Figure 4.6 Comparisons of qBBr QVs, FVs, and fluorescence τ_{act} to τ_{deact} in R1 Shaker mutants. **A)** A comparison of activation and deactivation protocols. The light cyan panel indicates where fluorescence was measured for **B-D**. **B)** Comparison of activation (purple) and deactivation (80 ms, red) QVs for R1C-qBBr:W454A;E247W (left, n=8), R1C-qBBr:W454A;I320W (center, n=5), and R1C-qBBr:W454A;T326W (right, n=7). **C)** As in **B**, but a comparison of activation and deactivation FVs, rather than QVs. **D)** Comparison of single exponential τ_{act} (n=3) to τ_{dea} (n=4) of R1C-qBBr:W454A;E247W (left), weighted τ_{act} (n=3) to τ_{dea} (n=5) of R1C-qBBr:W454A;I320W (center), and weighted τ_{act} (n=3) to τ_{dea} (n=3) of R1C-qBBr:W454A;T326W (right). Activation time constants are in purple and deactivation time constants are in red.

Previous studies have discussed the asymmetry in activation and deactivation currents, with deactivation currents being slower than those of activation (Labro et al., 2012; Lacroix and Bezanilla, 2012; Lacroix et al., 2011). Specifically, deactivation currents are slowed down in a voltage-dependent manner and correspond with pore opening (McCormack et al., 1994; Perozo et al., 1993).(Perozo et al., 1993) Moreover, the speed of these currents can be greatly altered with single mutations of the VSD (Lacroix and Bezanilla, 2012). Therefore, tracking the movement of the individual gating charges should give further insight to explain these

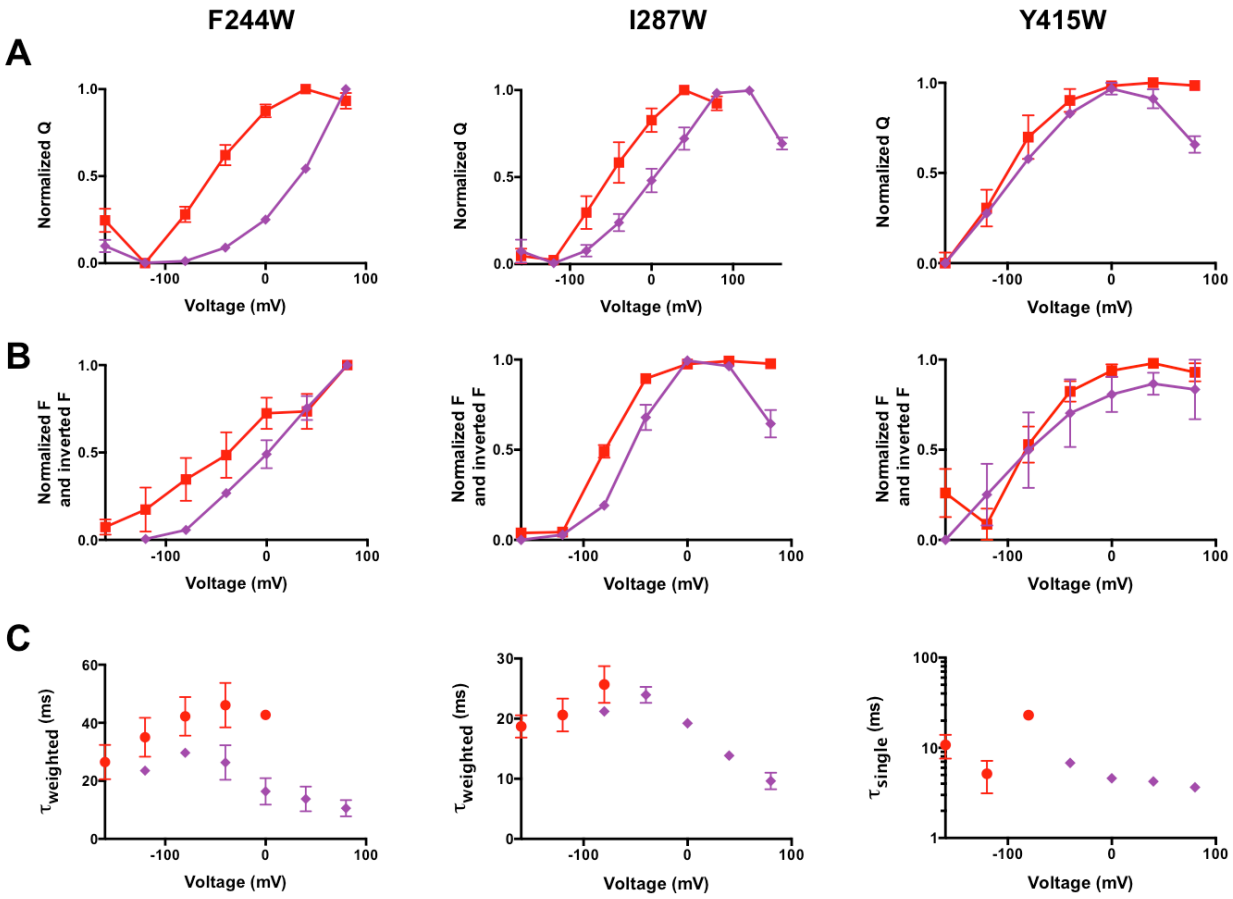

Figure 4.7 Comparisons of qBBr QVs, FVs, and fluorescence τ_{act} to τ_{deact} in R2C Shaker mutants. A**)** Comparison of activation (purple) and deactivation (80 ms, red) QVs for R2C-qBBr:F244W (left, n=4), R2C-qBBr:I287W (center, n=4), and R2-qBBr:Y415W (right, n=3). **C)** As in **B**, but a comparison of activation and deactivation FVs, rather than QVs. **D)** Comparison of single exponential τ_{act} (n=4) to τ_{dea} (n=3) of R2C-qBBr:F244W (left), weighted τ_{act} (n=4) to τ_{dea} (n=4) of R2C-qBBr:I287W (center), and weighted τ_{act} (n=3) to τ_{dea} (n=3) of R2-qBBr:Y415W (right). Activation time constants are in purple and deactivation time constants are in red.

differences, so we compared in detail the path of activation with deactivation. If the path of deactivation is the same as that of activation, we would expect to observe that activation and deactivation have similar voltage dependence and conformational changes as indicated by fluorescence. In Figure 4.6A the pulse procedures used to study activation (left) vs deactivation (right) are indicated. The comparison of the activation QVs and FVs to the deactivation QVs and FVs show that during deactivation there are leftward shifts in several constructs: R1C-qBBr:W454A;E247Q, R1C-qBBr:W454A;I320W, and R1C-qBBr:W454A;T326W (Figure 4.6B and C). We see similar shifts in R2-qBBr constructs (Figure 4.7A and B). The shifts in QV and FV curves indicate that the VSD has a different energetic path from the active to the resting state than from the resting state to the active state. This is also reflected in the speed of the fluorescence traces, where we do not see exact overlap in the kinetics of activation and deactivation fluorescence (Figure 4.6D and 4.7C). In two of our constructs, R1C-qBBr:W454A;E247Q and R1C-qBBr:W454A;I320W, the kinetics of the deactivation fluorescence are slower than that of activation. However, we detect the opposite for the fluorescence kinetics of R1C-qBBr:W454A;T326W (Figure 7.6D, right) where activation fluorescence kinetics are slower than those of deactivation. Others have observed that with the T326W mutation, both activation and deactivation are slowed, but activation much more strongly (Hong and Miller, 2000). Despite the opposite effect on fluorescence kinetics, we have strong evidence, the differing kinetics and the leftward shifts in Q and FVs, demonstrating a different path in activation verses deactivation.

The relaxed state is identified by qBBr tracking

The voltage sensor has three major conformational states: resting, active, and relaxed. The voltage sensor enters the relaxed state after prolonged depolarization (Bezanilla et al.,

1982a; Lacroix et al., 2011; Villalba-Galea et al., 2008). This state has been observed in most S4-based voltage sensors, including Kv channels as well as Nav, HCN, and CiVSP (Bezanilla et al., 1982a; Bruening-Wright and Larsson, 2007; Villalba-Galea et al., 2008). Even though there is no charge moved during the transition from the active state to the relaxed state, the relaxed state can

be detected through a slowing of the gating kinetics as well as a left-shifted QV curve in R1C-qBBr:W454A;E247W (Figure 4.8B, left) and R1C-qBBr:W454A;T326W (Figure 4.8C, left). As with deactivation, qBBr fluorescence can be used to visualize the relaxed state. Notably, voltage dependent qBBr fluorescence changes were also left-shifted upon a return to the resting state following prolonged depolarizations (Figure 4.8B and C, right).

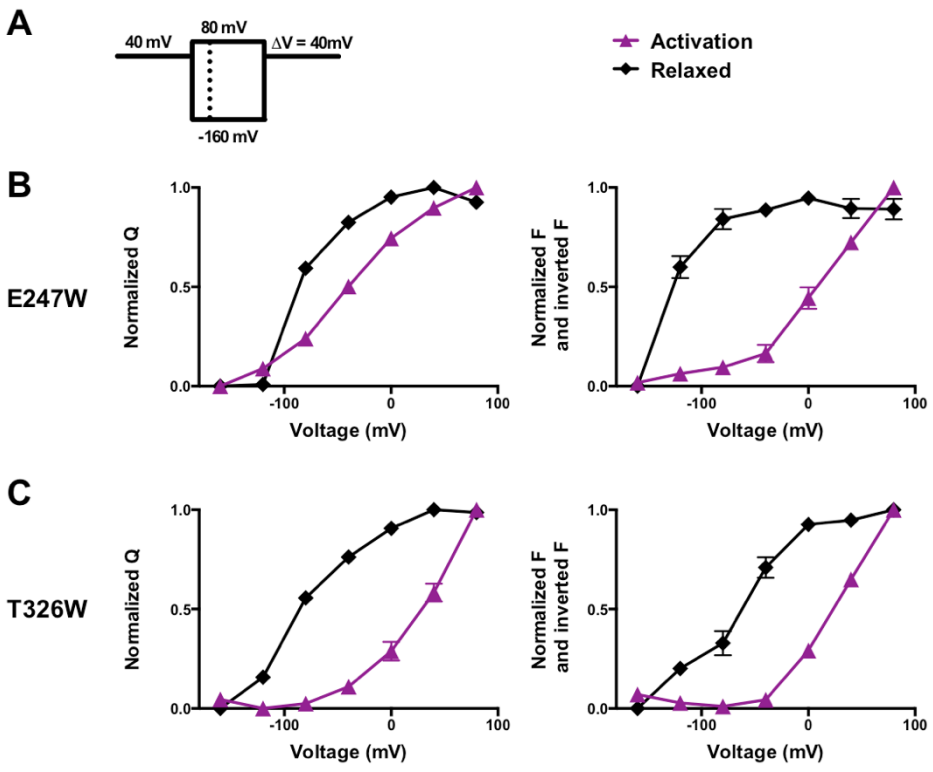

Figure 4.8 Comparisons of QVs and FVs as the voltage sensors enters the relaxed state in several Shaker R1C-qBBr mutants. A) A relaxation pulse protocol. **B)** R1C-qBBr:W454A;E247W $QV_{normalized}$ for activation (purple, n=4) and relaxed (black, n=4). **B)** Sh WF R1C W454A E247W 1-$FV_{normalized}$ and $FV_{normalized}$ for activation (purple, n=8) and relaxed (black, n=6). **C)** R1C-qBBr:W454A;T326W $QV_{normalized}$ for several activation (purple, n=4) and relaxed (black, n=4). **D)** R1C-qBBr:W454A; T326W 1-$FV_{normalized}$ and $FV_{normalized}$ for activation (purple, n=5) and relaxed (black, n=6).

R1C's interaction with F290 may provide the basis of the Cole-Moore shift

In addition to uncovering information about transitions to and from the resting, active, and relaxed states, we believe qBBr tracking provides novel insight into the Cole-Moore shift. The Cole-Moore shift describes a phenomenon where following a prolonged hyperpolarizing prepulse, a depolarizing pulse would elicit a conductance that had a longer time lag, or delay before beginning, as the prepulse is made more negative (Cole and Moore, 1960; Hoshi and Armstrong, 2015). The Cole-Moore shift is also seen in the gating currents underlying the conductance (Bezanilla et al., 1982b, 1994). The Cole-Moore shift can be elicited in several ways; typically, it is measured following a prepulse of increasing hyperpolarized voltage before a

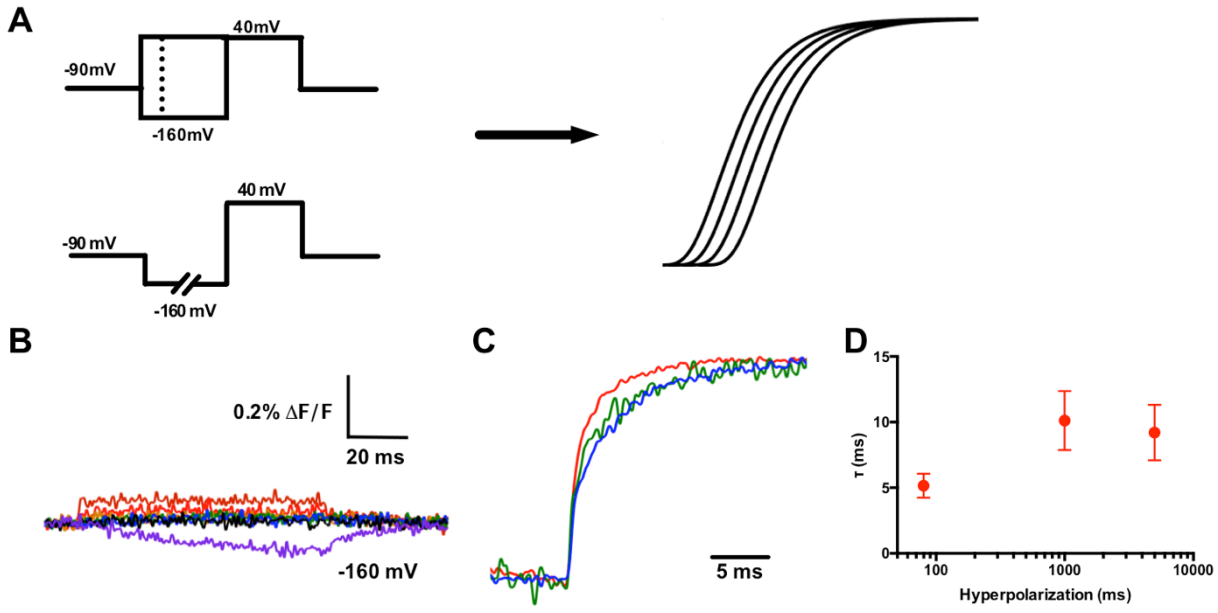

Figure 4.9 A physical basis of the Cole-Moore Shift as revealed by qBBr.
A) Two pulse protocols that produce a Cole-Moore shift, a variable voltage pulse before a depolarization (top) or a prolonged hyperpolarization pulse before depolarization (bottom) and an example of the resulting Cole-Moore shift. **B)** A family of fluorescence traces for R1C-qBBr:W454A:F290W, note the slow fluorescence response when hyperpolarized to -160 mV **C)** Representative fluorescence traces using the pulse protocol from panel A bottom, with -160 mV pulse for 80 ms (red), 1 s (blue) and 5 s (green). **D)** Comparison of the $\tau_{weighted}$ of the change in qBBr fluorescence produced by a 40 mV depolarizing pulse following hyperpolarizations of varying durations to -160 mV (as in the bottom pulse protocol in **A**). For 80 ms pulses, n=4; for 1 s pulses, n=5; for 5 s pulses, n=4.

depolarization (Figure 4.9A, left top) or increasingly long hyperpolarizing prepulses (Figure 4.9A left, bottom). The classical explanation for the Cole-Moore shift is that a hyperpolarization populates closed states that are further removed from the open state, thus delaying the opening as the channel has to traverse more states before opening (Cole and Moore, 1960). However, the molecular basis of the Cole-Moore shift remains unknown (Hoshi and Armstrong, 2015).

While measuring R1C-qBBr:W454A;F290W fluorescence, we observed no appreciable fluorescence signal in response to depolarizing pulses from -120 mV (Figure 4.3A). In response to hyperpolarizing pulses from -120 mV, we observed a small markedly slow reduction in fluorescence (Figure 4.9B). This fluorescence change did not correspond well to measurable gating currents either in terms of kinetics or thermodynamics. In response to a protocol used to induce and measure a Cole-Moore shift (Figure 4.9C, top, or 4.8A, left, bottom), the fluorescence change became slower as the duration of the hyperpolarizing pulse increased (Fig. 9C), as expected if this fluorescence is associated with the Cole-Moore shift of the channel.

Previous studies have shown that at negative potentials (closed state) R1C can spontaneously link to I287C, which is a full turn above F290 (Campos et al., 2007). Here, we observe at extreme hyperpolarizing potentials that R1C-qBBr moves near F290W, producing a slow quenching of fluorescence. We explain this as a result of moving the VSD with a strong hyperpolarization to such an extreme intracellular position, that we have populated other closed states of the voltage sensor that are responsible for the Cole-Moore shift. These closed states are tracked by the fluorescence change produced by an interaction between F290W and R1C-qBBr. A similar rarely observed closed state predicted by metal-ion bridges, in which R1 transitions from a position extracellular to F290 to a position intracellular to F290, was also suggested to provide a potential explanation of the Cole-Moore shift (Henrion et al., 2012).

Other voltage-sensitive membrane proteins can be investigated with qBBr

Our new technique allows for the interrogation of other VSD movements. For example, CiVSP is an excellent candidate for qBBr mapping. With the recent publication of a crystal structure (Li et al., 2014), we were able to begin the mapping of this VSD (Figure 4.10A). Due to labeling complications, we used the R217Q mutant as a background and found that CiVSP R217Q did not have endogenous qBBr signal when labeled.

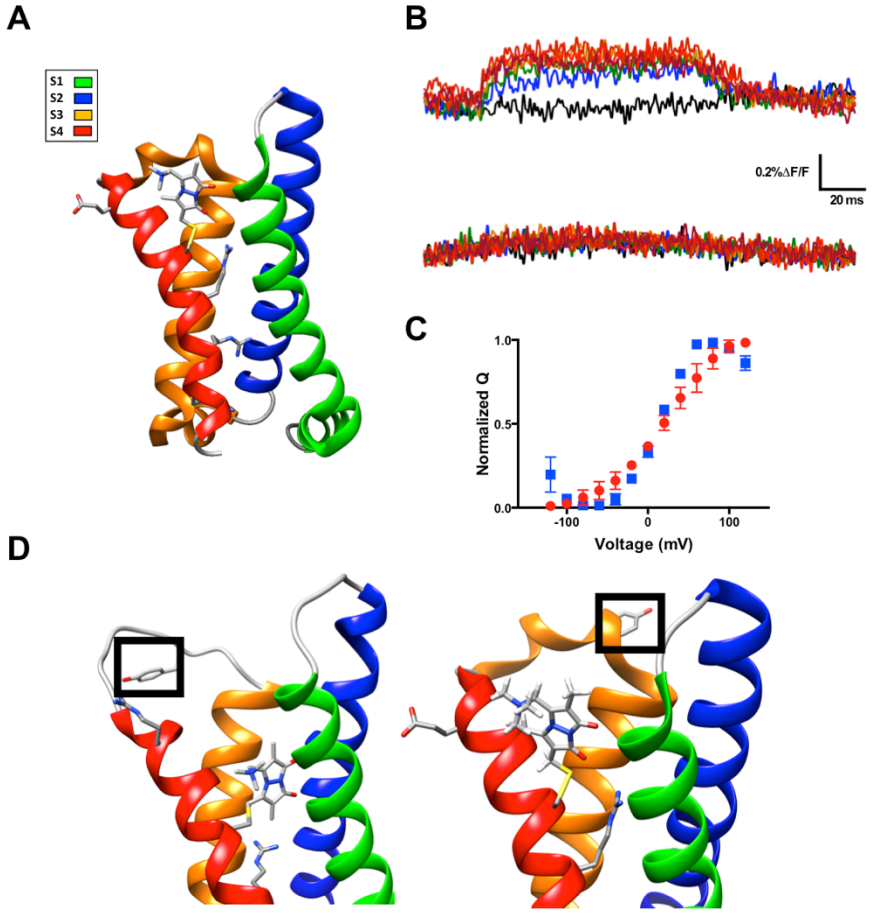

Figure 4.10 Application of qBBr to CiVSP A) CiVSP structure with qBBr attached at R1C and highlighting residue Y206 (PDB: 4G7V). **B)** Representative fluorescence traces of CiVSP R217Q R1C-qBBr (top) and CiVSP R217Q R1C-qBBr:Y206A (bottom) **C)** Normalized QV curves comparing CiVSP R217Q R1C-qBBr (n=4) and CiVSP R217Q R1C-qBBr:Y206A (n=4) **D)** CiVSP structure comparing the location of Y206 in the resting state (left, PDB: 4G80) and active state (right, PDB: 4G7V).

However, when we mutated the first gating charge, R223, to a cysteine and labeled with qBBr we found voltage-dependent endogenous fluorescence (Figure 4.10B). Much like with Shaker R1C we were able to identify and abolish the source of the endogenous signal. In this case it was a tyrosine, Y206. When mutated to an alanine, we no longer see voltage dependent fluorescence (Figure 4.10B). The voltage dependence of CiVSP is not altered by the mutation of

Y206A. This result is a starting point for investigating the movement of the gating charges of this VSD.

Discussion

In this paper we have demonstrated a technique that allows tracking a gating charge surrogate in the pathway of a voltage sensor using qBBr. We propose that this is a flexible tool that should prove readily applicable to other voltage-sensitive proteins. We have obtained new information on the trajectories of the first two gating charges in Shaker that are summarized in Figures 4.4 and 4.5. As we discuss the details of the trajectories, we will point out some of the limitations of the technique.

Spatial resolution.

In principle, one would expect that qBBr mapping is limited in its spatial resolution. Tryptophan-induced quenching (TrIQ) and tyrosine induced quenching (TyrIQ) of bimane dyes have been proposed as methods for measuring molecular distances (Brunette and Farrens, 2014; Mansoor et al., 2002, 2010). However, the maximum alpha carbon to alpha carbon distance over which TrIQ occurs with qBBr has been found to be around 10 to 11 Å (Mansoor et al., 2010), or possibly as high as 15 Å (Brunette and Farrens, 2014). It is clear that if one wish to measure static distances with this method it would suffer of poor spatial resolution and it would seem that with quenching occurring at such long distances it would be very difficult to trace any detailed pathway of qBBr. However, the fact that we are measuring a change in fluorescence as a function of time as the qBBr evolves in its pathway gives us much more resolution than measuring static fluorescence quenching in two positions. This is because we can detect very small changes in relative fluorescence as the qBBr approaches or recedes from the quencher, which is observed as a time course. For example, if qBBr moves a total distance of say 7 Å away

from the quencher during a depolarization, although that distance is always shorter than the 10 Å found to be a quenching distance, the degree of quenching will vary from extremely high when qBBr is close to W to less as it evolves to its final position. The change in fluorescence may only by 1 to 2% but it shows that qBBr is getting away from the quencher. In other words, we infer that it moved away even though we do not know the exact distance because we cannot calibrate absolutely the degree of quenching, mainly because of spurious background fluorescence. The technique then takes full advantage of the fact that we introduced a quencher in the putative path and when we see a change during a voltage pulse we can infer that is moving with respect to that quencher and if the signal does not change, it means that, either that quencher is far away from the path or that there is no movement with respect to that quencher. Therefore, qBBr mapping can be used not only to highly constrain the activated and resting positions of a particular gating charge but also by virtue of collecting data from so many locations it is possible to generate a trajectory for each of these charges.

Kinetics of trajectories are different for each charge and depend on initial conditions.

As discussed in the paragraph on the principles of the technique, a two-state model predicts that the kinetics of the fluorescence is independent of the position of qBBr with respect to the quencher. If qBBr moves between several discrete positions, then kinetics is affected by the relative distance with respect to the quencher but in that case the model predicts a time course of fluorescence with increases and decreases during the voltage pulse that moves the charge. In all our studies we have not seen increases and decreases of fluorescence during the pulse, instead there are always in the same direction (increase or decrease) albeit with different kinetics. We must assume, then that each gating charge is moving between two discrete states, which does not preclude that the sensor as a whole may have more than two states. The different

kinetics observed between different constructs, therefore, are most likely due to the introduction of a W mutation, which may alter the underlying gating current kinetics. This means that, although it would be ideal to be able to compare kinetics of one construct to another and thus make kinetic conclusions on the individual trajectories, the differences produced by the W mutations preclude us to do so.

However, using the same construct, voltage pulses of different durations or potential can be used to interrogate different transitions of the voltage sensor, and the kinetics in the same construct can then be compared. For example, the deactivation kinetics of the fluorescence change produced by R1C-qBBr:W454A:T326W are more rapid than its activation kinetics, suggesting that the interaction of R1C-qBBr with T326W is different during activation than during deactivation. This in turn informs us that the deactivation pathway of R1C-qBBr must be different from its activation pathway, an important conclusion that would be difficult to obtain with any other method. Another example is the slow R1C-qBBr:W454A:F290W fluorescence change upon hyperpolarization the kinetics of this interaction are markedly different from the kinetics of the main motion of the voltage sensor upon activation. This result, together with the fact that there is no fluorescence signal when a depolarization is started from a more positive potential gives direct evidence that R1 can populate a region of the sensor closer to the intracellular side when the membrane is strongly hyperpolarized and providing a molecular basis of the Cole-Moore shift.

Our data indicates that in the normal resting state, it appears that R1 does not come into close contact with F290 or I294 in the S2 segment, while R2 does come into close contact with I294. In the normal active state, R1 comes into close contact with W454 and Y415, while R2 comes into close contact with Y415, but does not interact with W454. One potentially related

observation is that two of our tested constructs were lethal: R1C:W454A;I287W and R2C:F290W. Whether the lethality of these constructs stems from a disruption of the normal resting state interactions of the gating pore remains to be investigated. However, R1 closely interacting with I287 in the resting state is in good agreement with earlier findings using disulfide bonding (Campos et al., 2007), fluorimetry (Pathak et al., 2007), and modeling (Henrion et al., 2012; Vargas et al., 2011).

The ability to optically track a gating charge in real time is a powerful technique, despite its limitations. It allows for the combination of crystallographic studies and functional data to understand the movement of the VSD. In general, our data with R1 and R2 supports a sliding helix model of movement of the gating charges; each discrete gating charge undergoes both a vertical translation and a rotation. Interestingly, the rotation of the R1 appears greater than the rotation of the R2, suggesting that some of the movement may be coming from the movement of the side chain, rather than from the movement of the voltage sensor backbone. We expect that this work can be expanded with molecular modeling. We may be able to test whether the charges move independently of each other, with the first and second gating charge moving first and then tugging the rest of the VSD along via the backbone of the S4 segment (Horng et al., 2017). Alternatively, the observed differences between the charges may stem from a spring-like behavior of the voltage sensor, transitioning from an α helix to a 3_{10} helix (Chakrapani et al., 2010; Henrion et al., 2012; Schwaiger et al., 2011).

The qBBr fluorescence data constrains the normal resting state of R1 to a position extracellular to F290 and indicate that interactions between this residue and R1 may be responsible for the Cole-Moore shift by moving the first charge deeper into the intracellular side. This result is consistent with the shallow QV curve recorded at very negative potentials and also

with the fact that the 'closed state' is in fact a collection of closed states in agreement with the increase in entropy when evolving from the open to the closed state.

Furthermore, qBBr fluorescence acts as a functional readout of different states of the voltage sensor. This information supports the hypothesis that the movements of both R1 and R2 are involved in the activation, deactivation, and derelaxation of the voltage sensor. Our data agrees with earlier kinetics models of activation and deactivation which preserve the accelerated kinetics of activation over deactivation (Lacroix 2011). Specifically, we observe that the QV and FVs of deactivation have a leftward shift to that of activation, thus demonstrating that the path of deactivation is different than that of activation. Intriguingly, the resolution of qBBr to look at discrete gating charges suggests that individual gating charges interact with residues of the voltage sensor differently during deactivation as opposed to during derelaxation. Future studies could use qBBr optical mapping to investigate gating during conductive events as to correlate features of gating with ion conductance.

A present limitation of the technique, as presented here, is that qBBr mapping of gating charges is limited by labeling accessibility to gating charges residues (changed to cysteine). In Shaker, for example, we were unable to link qBBr to the third most extracellular gating charge (R368, or R3). Future experiments using unnatural amino acid versions of qBBr or other fluorescent amino acids (Leisle et al., 2015) may allow for the expansion of this technique to additional charges in the voltage sensor.

Extension to other voltage sensors.

Numerous voltage sensors have been examined with site-directed fluorimetry, and these experiments have uncovered unique properties of a diverse array of sensors ranging from Shaker (Cha and Bezanilla, 1997; Mannuzzu et al., 1996) and other Kv1 type channels (Peters et al.,

2009; Vaid et al., 2008) to KCNQ/Kv7 channels (Kim et al., 2017; Osteen et al., 2010), Kv10 and Kv11 channels (Schönherr et al., 2002; Smith and Yellen, 2002), voltage-gated sodium channels (Cha et al., 1999; Wang et al., 2016), a voltage-gated calcium channel (Pantazis et al., 2014), a BK channel (Savalli et al., 2006), HCN channels (Bruening-Wright and Larsson, 2007), Catsper channels (Arima et al., 2018), and a voltage-sensitive phosphatase (Kohout et al., 2008). Extension of the qBBr WY-induced quenching technique to other voltage sensors is expected to provide new findings because this technique traces the charge trajectories during voltage sensing. As a proof-of-principle, we demonstrated qBBr can be extended to CiVSP, an evolutionarily distant voltage sensor that has previously proven tractable to fluorometric techniques that provide less spatial resolution than qBBr. Interestingly, we uncovered an interaction between R1 of CiVSP and a tyrosine residue in the S3-S4 linker that is in good agreement with a reported crystal structure of the voltage-sensing domain in the active state (Li et al., 2014). Being able to compare the VSD of a voltage sensitive phosphatase to that of an ion channel could lead to insights such as where the electric field is focused, which side charges interact with the VSD, and what are the differences in gating charge trajectory. Further mapping of additional voltage sensor pathways with the qBBr method described here should improve our understanding of how voltage sensors move and provide unprecedented insight into the characteristics of their discrete gating charges.

Methods

Generation of *Shaker* constructs

Mutations of the *Shaker* DNA were made on the *Shaker* Δ6-46 W434F background(Perozo et al., 1993) using the QuikChange II site directed mutagenesis kit (Agilent) with primers purchased from Integrated DNA Technologies. DNA was linearized using NotI (New England Biolabs) and

cleaned up with a NucleoSpin Gel and PCR Clean-up kit (Macherey-Nagel). *Shaker* cRNA was then synthesized from linearized DNA using the mMESSAGE mMACHINE T7 transcription kit (Life Technologies).

Mutations of the CiVSP DNA were made in CiVSP S363X background using the QuickChange II site directed mutagenesis kit (Agilent) with primers purchased from Integrated DNA Technologies (Iowa City, IA). DNA was linearized using XbaI (New England Biolabs) and tidied up with a PCR Clean-up kit (Lacherey-Nagel). *CiVSP* cRNA was synthesized from linearized DNA using the mMESSAGE mMACHINE SP6 transcription kit (Life Technologies).

Oocyte preparation

Oocytes were harvested from *Xenopus laevis* in accordance with experimental protocols approved by the University of Chicago Animal Care and Use Committee. Following collagenase digestion of the follicular membrane, oocytes were maintained in standard oocyte solution containing 96 mM NaCl, 2 mM KCl, 1 mM $MgCl_2$, 1.8 mM $CaCl_2$, 10 mM HEPES, and 50 μg/ml of gentamicin, set with NaOH to pH 7.4, for up to 36 hours prior to injection with 50 ng of cRNA. Following cRNA injection, oocytes were incubated at 16°C in standard oocyte solution for three to six days prior to recording.

Labeling with qBBr

The labeling solution consisted of depolarizing solution comprised of 120 mM KCl, 2 mM $CaCl_2$ and 10 mM HEPES at pH 7.4 with 1-2 mM qBBr (Sigma-Aldrich or Toronto Research Chemicals) added fresh to the solution upon each preparation. Oocytes were maintained in the solution for at least fifteen minutes and removed and washed in standard oocyte solution 5-20 minutes before recordings on them were performed. At the longest, oocytes were maintained in labeling solution for 120 minutes; however, due to the positive charge and impermeability of

qBBr, no differences were observed between oocytes labeled for long durations versus short durations.

Simultaneous fluorescence and electrophysiological recordings

Simultaneous electrophysiological and fluorescence recordings were performed at room temperature using the cut-open oocyte voltage-clamp technique, similar to prior descriptions (Cha and Bezanilla, 1997; Lacroix et al., 2012; Villalba-Galea et al., 2008) (Asamoah et al., 2003). External solution contained 115 mM N-methyl-D-glucamine, 2 mM $Ca(OH)_2$, and 20 mM HEPES taken to a pH between 7.4 and 7.5 with methanesulfonic acid. Internal solution was like external solution, but with 2 mM EGTA in place of $Ca(OH)_2$. Pipettes were pulled at a resistance of 0.2 to 1.0 MΩ and filled with 3M KCl. Excitation was performed with a mounted 420 nm LED (ThorLabs) reflected by a 455 nm long-pass dichroic (Chroma) through a 40X water-immersion objective (LUMPlan FL N, Olympus); emission was collected through the dichroic and a 475 nm long-pass filter (Chroma). Emission was integrated over each sampling period through a home-built integrator, collected by a PIN-020A photodiode (UDT Technologies), and amplified by a patch-clamp amplifier (L/M-EPC-7, LIST Medical Electronics). Voltage-clamp and electrical measurements were performed with a CA-1B amplifier (Dagan). The LED and voltage-clamp were controlled through Gpatch, an in-house acquisition program, and an SB6711-A4D4 board (Innovative Integration). Recordings were an average of four traces and filtered offline in MATLAB at 500 Hz or 1 kHz.

Data analysis

Data was analyzed using custom scripts in Matlab.

Chapter 5 - Applications of Unnatural Amino Acids in Voltage Sensors

Note: Parts of the following section is summarized from Infield, D.T., Lee, E.E.L., Galpin, J.D., Galles, G.D., Bezanilla, F., and Ahern, C.A. (2018). Replacing voltage sensor arginines with citrulline provides mechanistic insight into charge versus shape. J Gen Physio. *150*, 1017 with figure renumbering, reference reformatting, and combining of supplemental information

Abstract

The incorporation of unnatural amino acids into proteins is a versatile technique that allows for selective targeting of specific residues. We have demonstrated that we can incorporate unnatural amino acids into Shaker, a voltage-gated potassium channel, at several locations to answer a variety of questions. Here, we describe three projects that involve use of unnatural amino acids: single molecule movement of the voltage sensor, optical tracking of gating charge, and isomeric replacement of arginine with citrulline in the voltage sensor.

Introduction

The technique of unnatural amino acid (UAA) incorporation, while no longer new, is continuing to answer new questions. In combination with site-specific mutagenesis, UAA incorporation is a powerful tool to investigate conformational movements in voltage-gated ion channels (Beene et al., 2003; Noren et al., 1989). This *in vivo* nonsense suppression method relies on repurposing the amber stop codon (TAG) as an amino acid insertion site, using molecular machinery that is orthogonal to that of the host. A tRNA is chemically altered to be acylated with an UAA of choice. Simply put, a synthesized dinucleotide-AA substrate is

transcribed and refolded into a truncated tRNA. Following the refolding, the UAA is ligated to the tRNA (Pless and Ahern, 2013).

Incorporation of UAAs in *Xenopus laevis* oocytes requires the co-injection of mRNA for the gene of interest containing a TAG stop codon mutation at the amino acid position of interest, and the corresponding CUA anticodon tRNA with an attached UAA (Figure 5.1). This combination allows for targeted insertion of a specific UAA within the protein. These injections can result in three possible outcomes: the UAA will be incorporated at the TAG position, the UAA will not be incorporated resulting in a truncated protein, or the UAA will not be incorporated due to "read through" at the level of the cRNA or as a reacylation of the tRNA thus creating unlabeled protein or "bleed through" (Leisle et al., 2015).

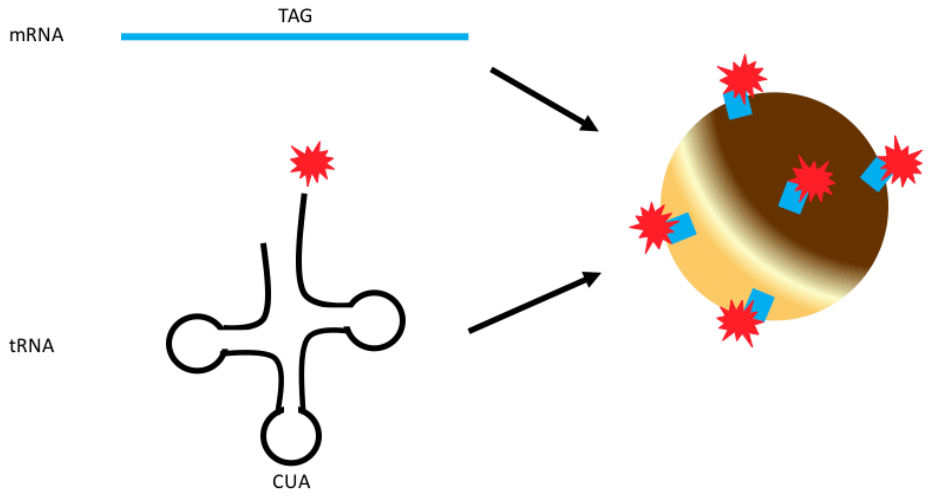

Figure 5.1 - Cartoon Schematic for UAA incorporation in Xenopus laevis oocyte Co-injection of mRNA with a TAG mutation at the site of interest and an acylated tRNA with the CUA anti-codon and an UAA (red star burst) of choice, allows for the expression of a UAA in a protein at a specifically selected site. Adapted from Pless and Ahern, 2013.

This is a very powerful tool that allows for an unprecedented amount of specificity in placement of an amino acid. This is especially useful when using a fluorescent unnatural amino acid (fUAA) as it allows for specific labeling of only the site of interest, thus decreasing the nonspecific labeling that is seen with traditional dye-labeling methods (Kalstrup and Blunck,

2013; Leisle et al., 2015; Pantoja et al., 2001). I applied fUAA incorporation in several projects with varying degrees of success: optical tracking of gating charges, single molecule movement of the voltage sensor, and citrulline replacement of arginine in the voltage sensor.

Single molecule movement of the voltage sensor

The ability to record cleanly from single channels revolutionized the field (Hamill et al., 1981). These studies allowed for the discovery of latent kinetic states of voltage-gated and ligand gated ion channels (Miller, 1978; Neher and Sakmann, 1976; Sakmann and Neher, 1984). Similar advances could be made through the ability to observe single voltage sensor movement. While, we cannot currently electrically resolve the movement of a single VSD (Bezanilla, 2005), single molecule studies have been accomplished using fUAA (Leisle et al., 2015; Pantoja et al., 2001). Single molecule studies of voltage sensor have been achieved. However, problems with intrinsic flickering in GFP prevented a fuller kinetic model from being developed (Dickson et al., 1997; Moerner et al., 1999; Sonnleitner et al., 2002; Treger et al., 2015).

I hypothesized that there are latent kinetic states of the voltage sensing domain (VSD) that are not detected during macroscopic movements but can be uncovered with single molecule fluorescence. I further hypothesized that we should see at least three states, since the sensor enters the relaxed state after prolonged depolarization (Lacroix et al., 2011; Villalba-Galea et al., 2008).

I generated a conductive Shaker mutation with a A359TAG mutation. This construct has high expression levels (Figure 5.3A) above bleed-through amounts of current (Figure 5.3B). Thus, for the rest of the experiments, I used Shaker-based constructs. Before fUAA experiments, we confirmed that Cy3 gives a voltage-dependent signal at A359C when labeled through

cysteine malemide labeling methods (Figure 5.3C). Therefore, we hypothesized that fUAA-Cy3 should also give a voltage-dependent signal at A359TAG.

To address these initial hypotheses, I co-injected *Xenopus laevis* oocytes with a fluorescent unnatural amino acid (fUAA-Cy3) at position A359TAG in Shaker, a voltage-gated potassium channel, and used two electrode voltage clamp to manipulate the membrane potential in fUAA-expressing oocytes. To visualize the movement of the potential single molecules in the membranes I used total internal reflection fluorescence microscopy (TIRFM). TIRFM gives us the advantage of selectively exciting fluorophores near a surface without exciting fluorophores in deeper regions (Axelrod, 2001). This in turn will decrease the background fluorescence and increase our signal. To achieve successful TIRFM in oocytes, I prepared acid etched glass coverslips to provide a clean, smooth surface. Next, these coverslips were coated with

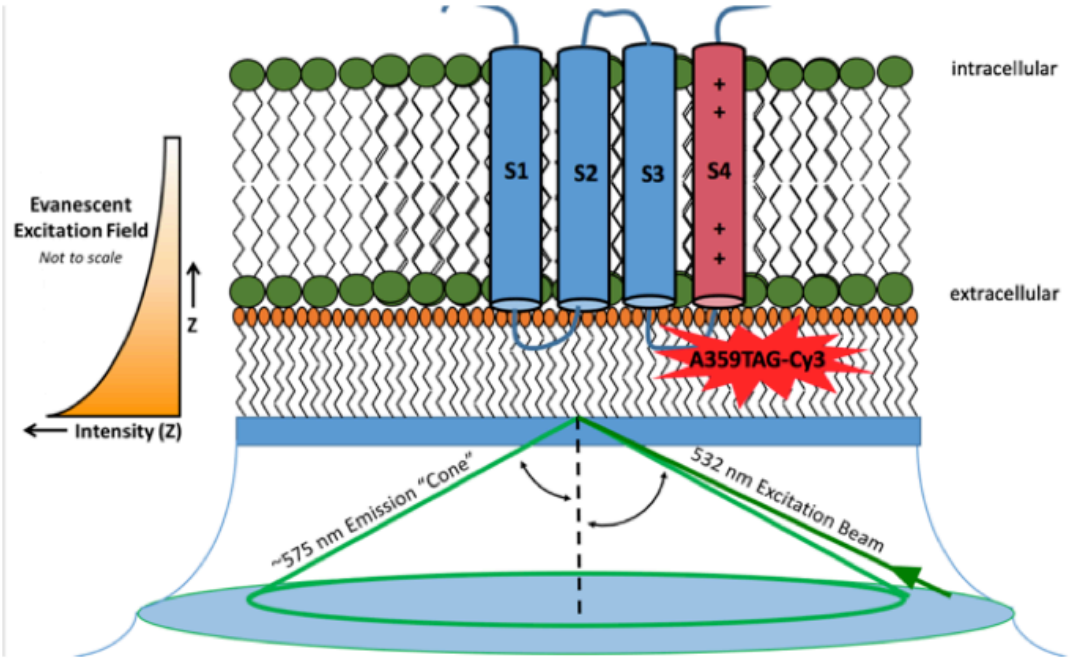

Figure 5.2 - Single molecule experimental set up
This is a representative schematic for investigating single molecule movement of a voltage sensor. A peeled *Xenopus laevis* oocyte animal-side down co-injected with Shaker A359TAG mRNA and tRNA for fUAA-Cy3 sits on a polymer cushion on Piranha etched glass. The Cy3 is excited with a 532 laser through a R405/488/561/635/800 excitation filter, a 560nm dichroic and a 550nm long pass emission filter.

polyethylenimine (PEI) to provide a polymer cushion that prevents sealing of the oocyte to the glass. This makes the voltage clamp effective and allows the voltage sensor to move (Treger et al., 2015). Individual chambers were created with Sylgard, which forms a watertight seal with the coverslip. The oocytes were peeled and mounted with the animal pole contacting the PEI-coated coverslip (Figure 5.2).

Utilizing these methods, I attempted to isolate single voltage sensor domain movements and generate single molecule fluorescence recordings which will give different fluorescence levels that can be interpreted as different kinetic states. Using two-electrode voltage clamp (TEV), I pulsed to 40 mV to in order to see the VSD in an activated state. I was unable to collect single molecules and often saw clumps (Figure 5.3E). However, as I searched for single molecules, I did observe macroscopic fluorescence signals indicating that the fUAA incorporated as expected at A359TAG in the Shaker channel. These fluorescence signals corresponded to previous experiments investigating macroscopic fluorescence currents in a similar construct (Shaker A359C) using cut-open voltage clamp (COVC) fluorimetry (Figure 5.3F). This is a promising first step to investigating the movement of a single voltage sensor. Future experiments should include titrating down the concentration of the Shaker channel, which would allow for more isolated single voltage sensors. Furthermore, since voltage-gated potassium channels are homotetramers, mutations that allow for fluorescence labeling result in a channel that has up to four fluorescent tags, which would limit resolution. A fully labeled Shaker channel could provide multiple steps from resting to active positions, complicating the final analysis. An alternative method could include using a monomer such as Ci-VSP or using Shaker with linked subunits and only incorporating one fUAA per channel (Yang et al., 1997).

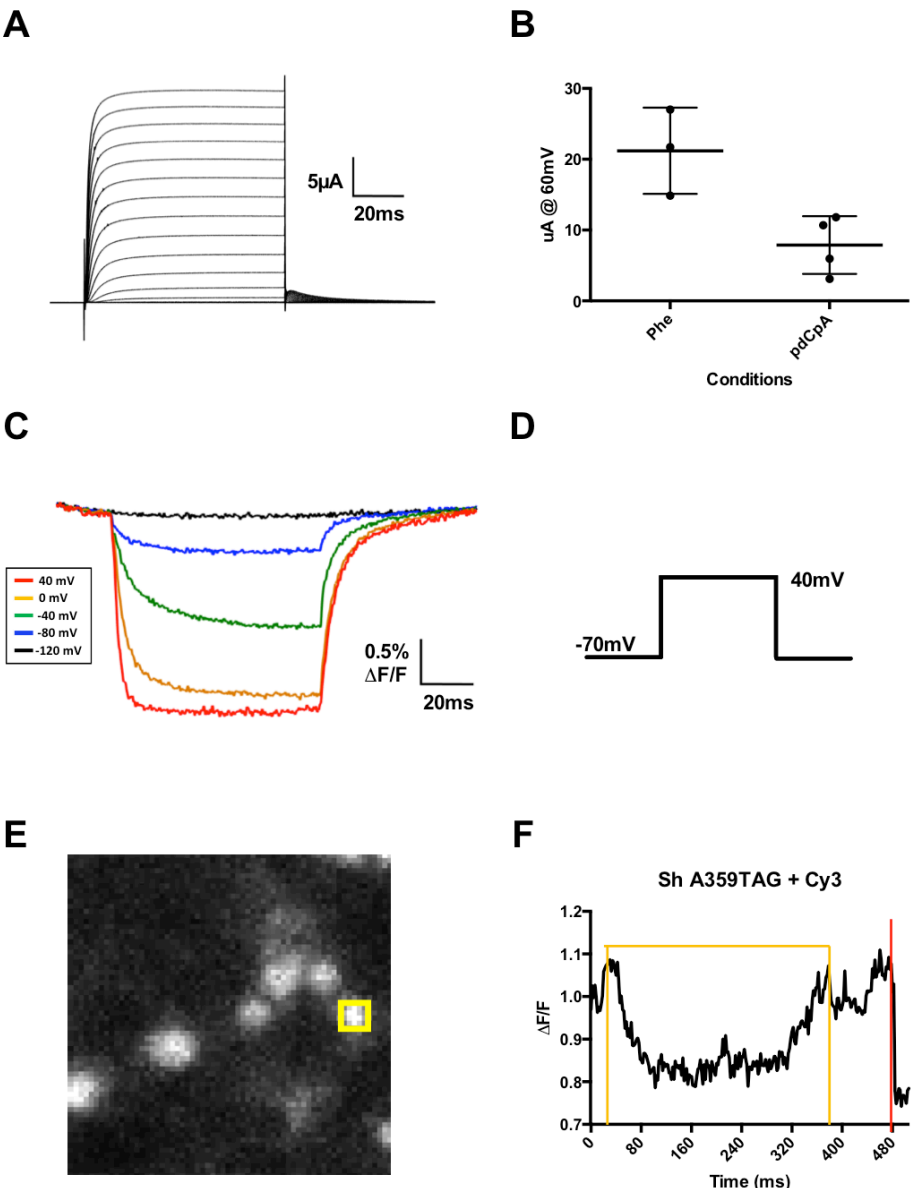

Figure 5.3 – fUAA Cy5 as a dye and single molecule incorporation in Shaker A359TAG
A) Representative voltage-dependent ionic currents from oocytes expressing Shaker A359TAG UAA Phe. **B)** A summary of Shaker A359TAG expression as current at a voltage of 60 mV with different injected tRNA of UAA, phenylalanine (Phe) n=3, dinucleotide constituted deoxycytidine and adenosine (pdCpA) n=4 **C)** Representative fluorescence family of traces of a traditional dye labelled oocyte expressing Shaker W434F A359C **D)** A pulse protocol for the TEV where the oocyte was held at -70 mV, pulsed to 40 mV for 350 ms and then returned to -70mV. **E)** A representative field of Cy3-fUAA fluorescence spots in oocyte at 40x magnification. These spots are more than a single molecule which may correspond to clustering. The yellow box is of a 3x3 pixel region to read fluorescence signals. **F)** Macroscopic signal of an oocyte expressing UAA Cy3 at residue 359 in Shaker collected using TIRF, n=10 spots. This is the result of a co-injection of fUAA tRNA with Cy3 as the fluorophore and cRNA of Shaker A359TAG construct. The red vertical line indicates when the laser turns off. The orange lines represent the voltage step to from a holding potential of -80 mV to 20 mV.

Optical tracking of the voltage sensor

As a continuation of my work with monobromobimane (qBBr) (Chapter 4), we explored the possibility of a fUAA with an attached bimane. Previous studies of the first two gating charges (R362 and R365) in Shaker have determined a movement from the intracellular to extracellular side of the membrane with a rotation. Each gating charge contributes non-additively to a total of ~12-13 elementary charges per channel and the deeper charges, R368 and R371, contribute to this total (Aggarwal and MacKinnon, 1996; Seoh et al., 1996). The motivation for investigating gating charges R368 and R371 was to determine their paths and model the interactions of the full voltage sensor. The UAA technique allows access to transmembrane portions of the protein that could not be approached with traditional dye labeling methods (Pless and Ahern, 2013). The Ahern lab synthesized a fUAA with the qBBr dye attached to the CUA tRNA. I attempted to incorporate my fluorescence source, qBBr, via UAA to specifically label gating charges R368 and R371 (R3 and R4, respectively).

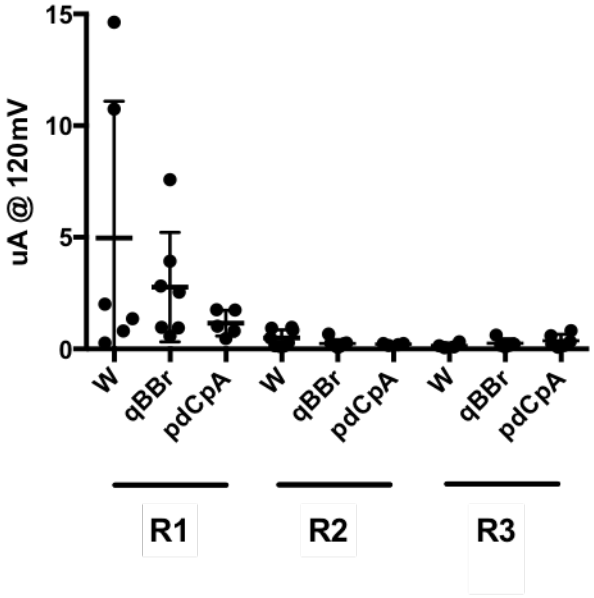

Figure 5.4 – fUAA qBBr poorly incorporates with Shaker gating charges
A summary of Shaker R1TAG, R2TAG, and R3TAG expression as current at a voltage of 60mV with different injected tRNA of UAA, tryptophan (W) n=3, UAA qBBr (qBBr), and dinucleotide constituted deoxycytidine and adenosine (pdCpA) n=4.

Since we knew we see qBBr signal at R362 and R365 (R1C and R2C, respectively), as a control, we tested the new fUAA there. However, while we observed large potassium currents

that indicated that we had a good tRNA incorporation at R1TAG and not just bleed through, we did not see qBBr fluorescence signal (Figure 5.4). Moreover, when we attempted R3 mutants with the fUAA-qBBr, we did not observe conductive currents. (Figure 5.4). Several potential future experiments exist here. Utilizing altered tRNA synthesis techniques may allow for production of improved fUAA-qBBr with stronger fluorescence. Additionally, using an alternate fluorophore may have better success incorporating at these deeper VSD positions. With further experimentation, optical tracking of more intracellularly positioned gating charges can be possible employing UAAs.

Citrulline replacement of gating charge

The final project in which I incorporated UAA was for the replacement of arginines for citrulline in the Shaker VSD as a collaboration with the Ahern lab. This work has been published in the Journal of General Physiology (Infield et al., 2018).

When studying voltage sensitive channels, a major focus of many experiments has been the charge and polarity of specific amino acids within the sensor domains. However, the shape of the amino acid has not been well accounted for in many studies. The goal of this project is to

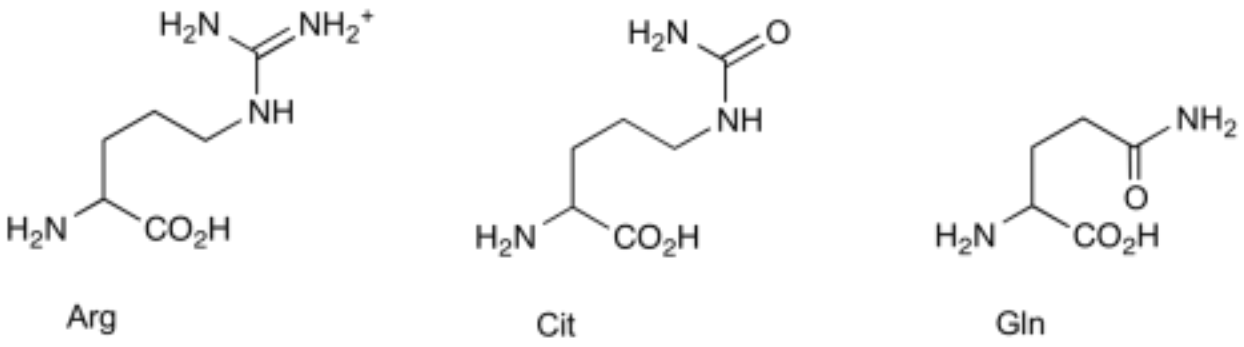

Figure 5.5 – A structural comparison between arginine and citrulline and glutamine
Similarities in chemical structure of arginine and citrulline, with a large difference being the lack of positive charge in citrulline. Adapted from Infield et al., 2018.

tease apart the importance of the shape of arginine from that of its charge by replacing it with a neutral amino acid of a similar shape, citrulline. Utilizing UAAs, we replaced arginine with citrulline in the VSD of Shaker, a voltage-gated potassium channel, and observed effects on both the voltage sensitivity and kinetics of gating.

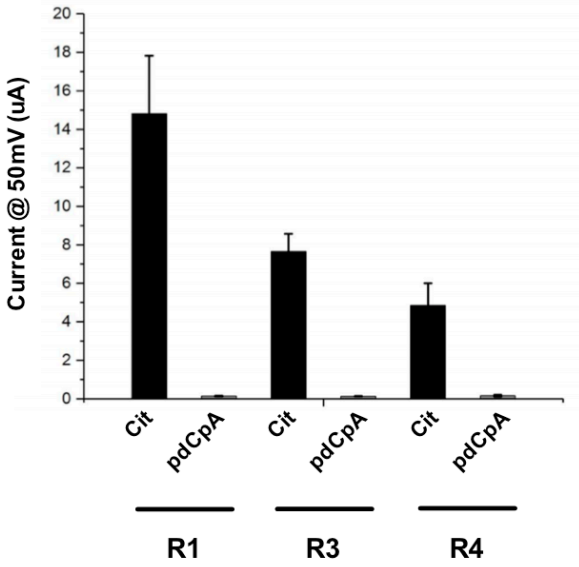

Figure 5.6 – Citrulline incorporation at different gating charges in the Shaker voltage sensor.
Two electrode voltage clamp recordings of ionic currents measured at 50mV of oocytes expressing Shaker channel with citrulline at R1, R3, and R4 in comparison to oocytes co-injected with uncharged UAA. Adapted from Infield et al., 2018.

Using TEV, we observed incorporation of citrulline occurs at R1, R3, and R4 (Figure 5.6). At position R2, we observe no ionic currents, indicating that R2 does not incorporate citrulline. The rescue of R2Cit may not have occurred in enough channels to see ionic currents. Thus, we focused on the other three gating charges and their movements.

As the voltage sensor is moved to an activated position, the outermost facing gating charge, R1, moves upward and rotates out (Bezanilla, 2002). This movement is thought to traverse the membrane through a focused electric field, moving from below F290 (the hydrophobic plug) toward the extracellular membrane (Ahern and Horn, 2005; Bezanilla, 2000; Yang et al., 1996). Mutations at R1 conventionally generate a 30-40 mV rightward shift of the GV curve, by either neutralizing or altering the side chain (Chowdhury et al., 2014; Papazian et al., 1991). As a comparison, we also mutated gating charge arginines into glutamines, which

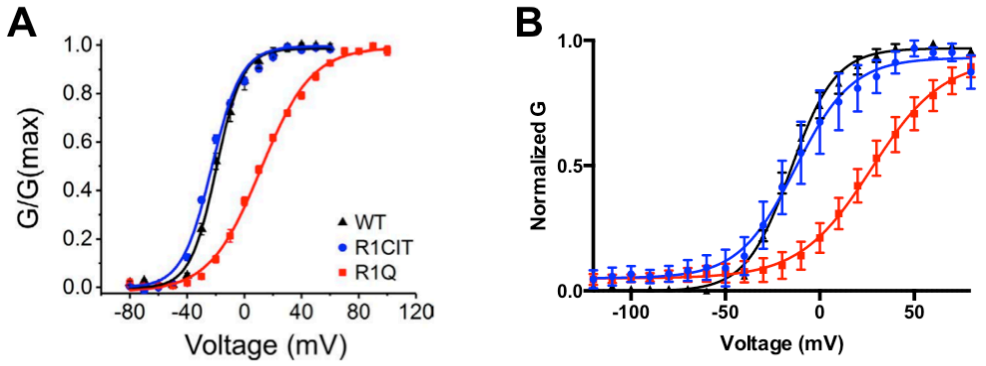

Figure 5.7 – Citrulline incorporation at R1 in the Shaker voltage sensor.
Normalized G-V values of oocytes expressing wild-type Shaker (black), Shaker R1Cit (blue), R1Q (red) in **A)** TEV and **B)** COVC. Error bars represent ±SEM. Adapted from Infield et al., 2018.

have well-documented effects on the conductance of Shaker. We also find a similar 30 mV shift when we replace R1 with a glutamine (Figure 5.7A and 5.7B).

When we incorporated citrulline at R1, we found very little difference from wild type and have demonstrated this in both TEV and COVC recordings (Figure 5.7A and 5.7B). We found a small leftward shift of $V_{1/2}$ -19.4±3.5 mV and -25±1.7 mV of wild type and R1Cit, respectively. Our results demonstrate that the charge at R1 does not play a large role in channel function, as long as the amino acid shape remains unaltered.

As one of the deeper-set gating charges, R3 passes through the electric field in the membrane as it is activated and has been modeled to be electrostatically bound to E247 in the active state (Khalili-Araghi et al., 2010). When mutated to glutamine, we observe an expected large rightward shift in the GV (Figure 5.8). When we incorporate citrulline, we observe a $V_{1/2}$ of -1.4±5.3 mV, resulting in a 18 mV rightward shift when compared to wild type Shaker. Together, the data from encoding citrulline at R1 and R3 demonstrate the importance of arginine's shape versus its charge in channel function.

The R4 is the most intracellular arginine to move across the hydrophobic plug during activation. When mutated to a glutamine, there is a small leftward shift of the GV curve. When incorporating citrulline at R4, in TEV, we observed at large hyperpolarizing shift in the resting membrane potential, indicating a standing potassium conductance (Figure 5.8). To further investigate this phenomenon, we recorded these constructs using cut-open voltage clamp (Stefani and Bezanilla, 1998) which has a faster clamp and allows for control of intracellular solutions. We used this other methodology to determine the effect citrulline incorporation at R4 has on the kinetics of activation and deactivation (Figure 5.9E and 5.9F).

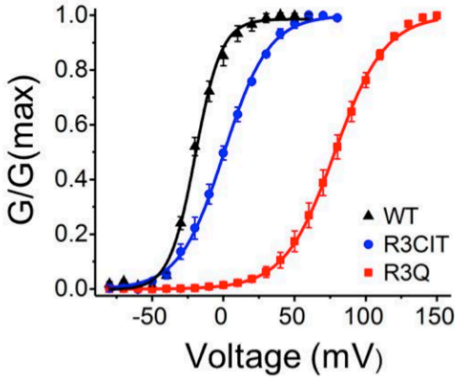

Figure 5.8 – Citrulline incorporation at R3 in the Shaker voltage sensor. Normalized GV values of oocytes expressing wild type Shaker (black), Shaker R3Cit (blue), and R3Q (red) in TEV. Error bars represent ±SEM. Adapted from Infield et al., 2018.

Using this method, we still found a leftward shift from recordings of R4Q. With the encoding of citrulline at R4, we saw an even more pronounced leftward shift of the GV curve (Figure 5.9D). As shown in the representative traces, the tails of the R4Cit mutant are grossly different from those of wild type and R4Q (Figure 5.9A-C). Both the activation and deactivation kinetics were greatly slowed in the R4Cit mutant (Figure 5.9E and 5.9F). The large change to channel function when encoding citrulline at R4 could be due to its interaction with the highly conserved hydrophobic plug F290 (Lacroix and Bezanilla, 2011). Others have also shown that mutations at R4 dramatically alter channel function. Mutation of R4 to alanine creates a large leftward shift (Chowdhury et al., 2014), whereas mutation to glutamine results in a small

leftward shift (Seoh et al., 1996). Mechanistically, the change in the kinetics of activation and deactivation could be due to the altered polarity of the R4 residue. When in the inactive state, R4 is intracellular to the electric field as demonstrated via cross linking, molecular dynamic and spectroscopy studies (Henrion et al., 2012). Due to the lack of charge at R4Cit, this residue no longer senses changes in voltage and its movement through the electric field would be slowed through the hydrophobic plug. Thus, when the voltage sensor is activated and R4 moves past F290 determining the state of the voltage sensor (Lacroix and Bezanilla, 2011), ionic conductances would be slowed due to the lack of charge at R4. For deactivation, we would also

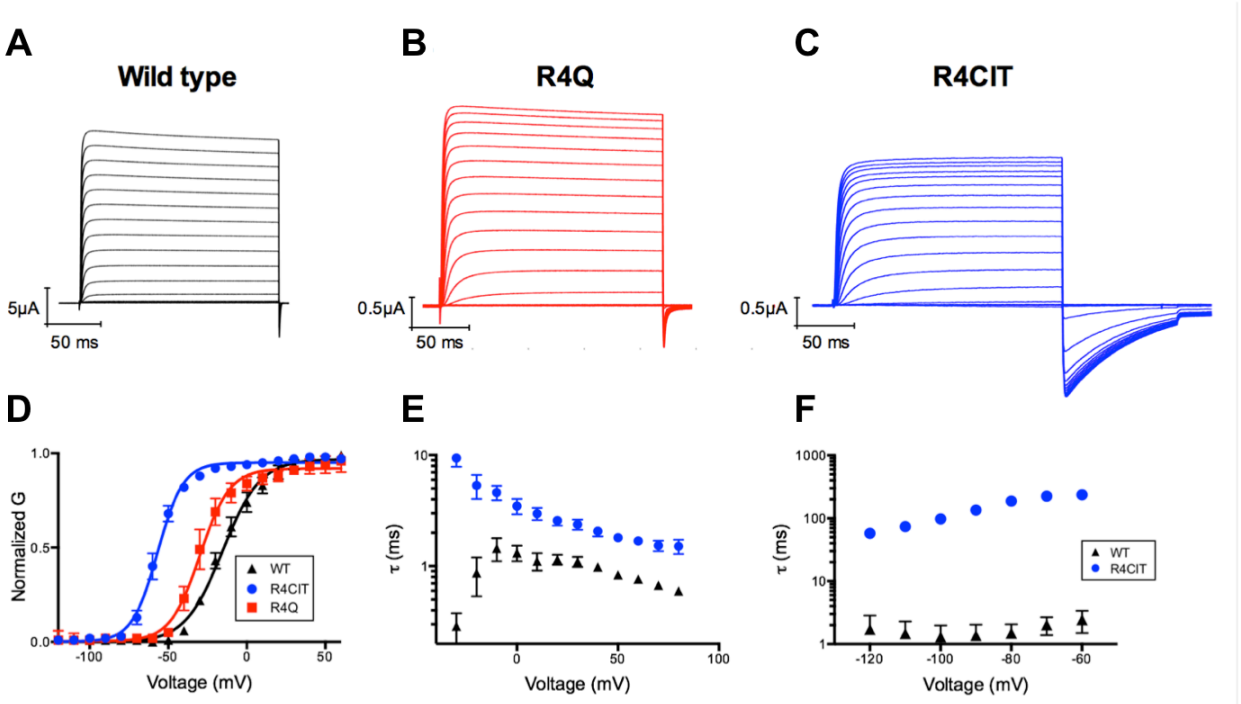

Figure 5.9 – Citrulline incorporation at R4 in the Shaker voltage sensor.
(A–C) Normalized G-V curves from COVC of WT-, R371Q-, and R371Cit-Shaker. Oocytes were held at -80 mV, then prepulsed to -120 mV for 200 ms, before a variable pulse ranging from 80 mV to -120 mV, followed by a postpulse to -120 mV, before returning to the original holding potential. **D)** Normalized GV values. Error bars represent ±SEM. **E)** A comparison of the activation rate (τ) between WT- and R371Cit-Shaker as derived from the same data used for the GV curves. **F)** Deactivation rate for WT- and R317Cit-Shaker. For these data, oocytes were held at -80 mV, prepulsed to -120 mV for 200 ms, then pulsed to 80 mV for 50 ms, followed by a variable pulse ranging from 80 mV to -120 mV for 350 ms, before returning to the original holding potential. Adapted from Infield et al., 2018.

expect a slowing of conductance kinetics because in the active state, R4 is positioned within the electric field (Long et al., 2007). Therefore, our data is consistent with the idea that during deactivation, the loss of a charge at R4 via citrullination slows kinetics more than during activation. Furthermore, our results suggest that the loss of electrostatic interaction between R4 and the hydrophobic plug is due to charge neutralization. This result demonstrates the large importance of charge at position R4, independent of amino acid shape.

In conclusion, our study demonstrates the importance of both the charge and shape of arginine at different locations within the voltage sensor. At R4, the positively charged arginine plays a large role, whereas its shape is more important at R1 and R3. This study gives further insight on the importance of both charge and shape in arginine in the voltage sensor.

Discussion

UAA incorporation is a newer approach that can answer many questions in the fields of neuroscience and biophysics. We have applied this tool to begin deciphering how the voltage sensor moves at the single molecule level. Moreover, we attempted to follow the movement of deeper gating charges (R3 and R4) using fUAA. While we encountered difficulties in performing fUAA-qBBr incorporation experiments, they provide valuable proof-of principle for employing fUAAs to answer biophysical questions. Importantly, these experiments have allowed us to identify areas where our methodology requires further optimization. Future experiments will be needed to improve incorporation, or to determine whether other fluorophores will translate better at these positions.

Methods

Oocyte Preparation

Oocytes were harvested from *Xenopus laevis* in accordance with experimental protocols approved by the University of Chicago Animal Care and Use Committee. Following collagenase digestion of the follicular membrane, oocytes are stored at 18°C in standard oocyte solution (SOS), 96 NaCl, 2 KCl, 1.8 $CaCl_2$, 1 $MgCl_2$, 10 HEPES, at pH 7.4 with 10 mg/L of gentamicin. Oocytes were typically injected 1-2 days post digestion. For single molecule experiments oocytes were placed in a sucrose solution for 15 minutes to shrink before being rinsed in SOS and being peeled with #5 forceps and mounted in a homemade Slygard chamber.

For cut-open voltage clamp, the labeling solution consisted of depolarizing solution comprised of 120 mM KCl, 2 mM $CaCl_2$ and 10 mM HEPES at pH 7.4 with 20 μM Cy3 maleimide (Lumiprobe, Hunt Valley, Maryland) . Oocytes were maintained in the solution for at least fifteen minutes and removed and washed in standard oocyte solution 5-20 minutes before recordings were performed.

Molecular Biology

Shaker cRNA that had been previously synthesized using the mMESSAGE mMACHINE T7 transcription kit (Life Technologies). Shaker W434F M356C was mad e on the Shaker Δ6-46 W434F background (Perozo et al., 1993) using the QuikChange II site directed mutagenesis kit (Agilent) with primers purchased from Integrated DNA Technologies. DNA was linearized using NotI (New England Biolabs).

For oocyte expression, DNA was prepared using the NucleoSpin Plasmid kit (Macherey-Nagel, Bethlehem, PA) and linearized with XbaI (New England Biolabs, Ipswich, MA). Linearized cDNA was transcribed to RNA with the mMESSAGE mMACHINE SP6 kit (Life Technologies, Carlsbad, CA). Oocytes were injected with 50 ng of RNA and incubated at 18°C in solution containing (in mM) 96 NaCl, 2 KCl, 1.8 $CaCl_2$, 1 $MgCl_2$, 10 HEPES, at pH 7.4 with 10 mg/L of gentamicin. Recordings were made 1-2 days following injection.

Unnatural amino acid preparation

UAA were prepared as described in (Leisle et al., 2016) and (Infield et al., 2018)

Creation of the Sylgard Chamber

Glass slides were incubated in piranha solution (70% H_2SO_4 at 18M / 30% H_2O_2 at 30% w/w, both from Sigma-Aldrich, St. Louis, MO) followed by rinsing with water and storage under water. When used to prepare a chamber, a slide was removed and dried under a stream of nitrogen. Then a chamber cut from cured Sylgard 184 (Dow Corning, Midland, MI) was placed on the dry slide. Sylgard 184 was mixed as directed and poured into a round mold on a sheet of very clean, dry borosilicate glass to form a layer ≈ 2 mm high. The sylgard was then cured in an oven at 80°C for one hour. A piece was formed with a 1 cm round chamber and transferred to the surface of an acid etched glass coverslip. If the bottom surface of the sylgard was extremely clean, and the glass was well-dried, the sylgard adhered to the chip and formed a water-tight seal. A solution of 200 mM polyethylenimine (Mw ≈ 750,000, Sigma-Aldrich) in SOS (96 mM NaCl, 2 mM KCl, 1 mM $MgCl_2$, 1.8 mM $CaCl_2$, 20 mM HEPES) was placed into the chamber and left for 30 minutes, followed by extensive rinsing with fresh SOS. This recording chamber was filled

with SOS for recording. To allow TIRF microscopy, oocytes were placed in a high osmolality 'shrinking' solution prior to recording and the vitelline membranes were mechanically removed (Sonnleitner et al., 2002). Oocytes were then placed into the recording chamber and mounted on the microscope.

Electrophysiology and Microscopy

Simultaneous recordings of gating currents and fluorescence responses were performed using the cut-open oocyte voltage-clamp technique (Stefani and Bezanilla, 1998) in combination with a photodiode to measure temporal changes in fluorescence emission (Cha and Bezanilla, 1998). Gpatch, an in-house program, controlled an SB6711 digital signal processor-based board (Innovative Integration, Simi Valley, CA) with an A4D4 board (Innovative Integration, Simi Valley, CA). Oocytes were held under voltage-clamp with a Dagan CA-1B amplifier (Minneapolis, MN) and current was filtered at 5 kHz.

Sh A359TAG fUAA Cy3 was sampled at 50 kHz and fluorescence emissions were collected through an Olympus LUMPlan FL N 40X/0.8 NA water-immersion objective by a PIN-020A photodiode (UDT Technologies, Torrance, CA), amplified by a patch clamp amplifier L/M-EPC-7 by LIST Medical Electronic (Darmstadt, West Germany) with a filter of 10 kHz, and then integrated over each sampling period using a home-built integrator circuit. Cy3 was excited via a ThorLabs LED controller powering a 535 nm LED (ThorLabs, Newton, New Jersey) that was passed through a filter cube housing a 540/25x, a 565 long pass dichroic and a 605/55nm emission filter (Chroma Inc., Bellows Falls, Vermont) through a 40X water-immersion objective (LUMPlan FL N, Olympus); emission was collected through the dichroic and a 475 nm long-pass filter (Chroma). All recordings were performed at around 18°C, with an external solution

containing (in mM) 12 KCl, 108 N-methyl-D-glucamine neutralized with methanesulfonic acid (NMG/MES), 10 HEPES, and 2 $Ca(OH)_2$ and an internal solution containing (in mM) 120 NMG-MES, 10 HEPES, and 2 EGTA. Both solutions were set to pH 7.4. Microelectrodes were pulled on a Flaming/Brown micropipette puller (Sutter Instruments, Novato, CA, model P-87) and were filled with 3 M $CsCl_2$ and had a resistance of ~0.2–0.8 MΩ.

Single Molecule

Two-electrode voltage clamp was performed in a two-electrode configuration with a Warner Instruments OC-725A amplifier (Hamden, Connecticut). Both the electrophysiological and optical equipment were controlled using in-house software. Cy3 fluorescence from potential single molecules was recorded by an Evolve 128 EMCCD camera (Photometrics, Tucson, Arizona) attached to a home-built TIRF setup based on an Olympus IX71 inverted microscope (Center Valley, Pennsylvania) with a 60X/1.45 NA microscope objective (Olympus). Excitation was provided by a 532 nm DPSS laser (Laserglow Technology Inc., Toronto, Canada) Typical excitation intensities were around 150 W/cm^2. Fluorescence was observed through a R405/488/561/635/800 excitation filter (Semrock, Rochester, New York), a 560nm dichroic (Semrock) and a 550nm long pass emission filter (Chroma Inc., Bellows Falls, Vermont)

Iowa two-electrode voltage clamp recordings

Two-electrode voltage-clamp (TEVC) recordings were made in standard Ringer's solution containing (in mM) 116 NaCl, 2 KCl, 1.8 $CaCl_2$, 2 $MgCl_2$, and 5 HEPES. The holding potential was -80 mV. G-V values were derived from isochronal tail currents from cells expressing at least 1 μA of tail current, for all variants except R368Q-Shaker, which closed too quickly to reliably

quantify tail currents. In this case, we derived G-V values from ionic currents, assuming a reversal potential for potassium of -80 mV. The data we derived from R368Q were in good agreement with those published previously.

Chapter 6 – Discussion

The work presented in this dissertation aimed to develop methods to understand the movement of voltage sensors in voltage sensitive proteins and the creation of new methodologies. We focused on techniques that may have future applications for biophysicists and neurobiologists. First, we characterized the genetically encoded voltage indicator (GEVI) ASAP1, accelerated sensor of action potential 1. Besides being able to track action potentials with sub-millisecond fluorescence lag and a large signal, this GEVI has a plateau in the fluorescence response in the physiological voltage range. Applying a rational design method, I improved this GEVI and created ASAP-Y by adding a tryptophan mutation at the top of the S4. This improvement slightly increased kinetics and signal size, but most importantly generated a much more robust response in the physiological range (Chapter 2).

As a method to improve recording fluorescence signals *in Xenopus laevis* oocytes, I have designed novel methods for darkening oocytes. The first method is pharmacologically-based and decreases the endogenous fluorescence of *Xenopus laevis* oocytes (Chapter 3). Through the injection of a SIK-inhibitor, we decreased the endogenous fluorescence of the oocyte. The second is more directly applied by injecting synthetic melanin into an oocyte. Both of these methods allow for improved optical recordings in oocytes and can be applied to any experiment requiring improved background fluorescence conditions. It is possible for this method to be applied to other experimental systems wherein background fluorescence is a systematic problem such as total internal reflection microscopy, single-molecule tracking, and fluorescence resonance energy transfer studies.

Next, we demonstrated that a small positively charged dye, qBBr, can be used to optically track the movement of the gating charges of the voltage sensor. In these trajectories, we

detected a difference in the path of activation and deactivation. Moreover, we uncovered the physical basis for the Cole-Moore shift, which has puzzled biophysicists for decades. This shift occurs when the voltage sensor is hyperpolarized before activation which leads to a lag in ionic and gating currents. In the future, this methodology can be used to describe the movement of other VSDs and help investigate other voltage-dependent states of VSDs (Chapter 4).

Finally, I demonstrated several applications of UAAs with varying degrees of success. Although some UAA incorporation still needs to be optimized, it is a viable method to investigate traditionally inaccessible amino acid residues as well as optically track voltage sensor movement at the single molecule level. I was able to successfully incorporate UAAs when replacing arginines with citrullines in the VSD. This was the first example of *in vivo* site-directed encoding of citrulline employed via UAA. Here we demonstrated the importance of the shape of the amino acid independent of its polarity in VSD movement (Chapter 5).

Though I largely focused on basic science questions and methods, the new techniques presented here show great potential for use in translational applications. Ion channel dysfunction is responsible for many genetic and sporadic cardiac (Amin et al., 2010), neurological (Maljevic and Lerche, 2013), and skeletal muscle (Davies and Hanna, 2003) pathologies. Using GEVIs to obtain an optical readout of voltage changes has many translational applications. For diseases that involve neuronal networks, such as epilepsy, studies could be improved by having high expressing, low toxicity GEVI which would allow an optical output of seizure with better time resolution than current methods (Grosenick et al., 2015). Other potential applications include investigating cardiac disease and symptoms such as arrhythmias, where using a GEVI to probe electrical function could streamline pharmacology studies (Liao et al., 2015). With the encoding of UAAs, being able to specifically place an amino acid of our choosing could be a promising

technique to understand the effects of post-translational modifications. Specifically, citrulline is a factor in several cardiac disorders and the citrullination of myofilament proteins is implicated in heart failure (Fert-Bober et al., 2015). Being able to direct placement of citrulline in myofilament proteins could help identify sites of interest for drugs combating heart failure. Additionally, the melanin injection studies have translational aspects as well. With respect to synthetic melanin, persons with vitiligo suffer from depigmentation of skin and could benefit from some form of treatment (Yaghoobi et al., 2011).

Overall, these techniques have many promising applications to translational questions that they are specifically tailored to answer.

References

Abdelfattah, A.S., Kawashima, T., Singh, A., Novak, O., Liu, H., Shuai, Y., Huang, Y.-C., Grimm, J.B., Patel, R., Friedrich, J., et al. (2018). Bright and photostable chemigenetic indicators for extended in vivo voltage imaging. BioRxiv 436840.

Aggarwal, S.K., and MacKinnon, R. (1996). Contribution of the S4 Segment to Gating Charge in the Shaker K+ Channel. Neuron *16*, 1169–1177.

Agnew, W.S., Levinson, S.R., Brabson, J.S., and Raftery, M.A. (1978). Purification of the tetrodotoxin-binding component associated with the voltage-sensitive sodium channel from Electrophorus electricus electroplax membranes. Proc. Natl. Acad. Sci. U. S. A. *75*, 2606–2610.

Ahern, C.A., and Horn, R. (2004). Specificity of charge-carrying residues in the voltage sensor of potassium channels. J. Gen. Physiol. *123*, 205–216.

Ahern, C.A., and Horn, R. (2005). Focused electric field across the voltage sensor of potassium channels. Neuron *48*, 25–29.

Amin, A.S., Tan, H.L., and Wilde, A.A.M. (2010). Cardiac ion channels in health and disease. Heart Rhythm *7*, 117–126.

Arima, H., Tsutsui, H., and Okamura, Y. (2018). Conservation of the Ca2+-permeability through the voltage sensor domain of mammalian CatSper subunit. Channels Austin Tex.

Armstrong, C.M., and Bezanilla, F. (1973). Currents related to movement of the gating particles of the sodium channels. Nature *242*, 459.

Armstrong, C.M., and Binstock, L. (1965). Anomalous Rectification in the Squid Giant Axon Injected with Tetraethylammonium Chloride. J. Gen. Physiol. *48*, 859–872.

Axelrod, D. (2001). Total Internal Reflection Fluorescence Microscopy in Cell Biology. Traffic *2*, 764–774.

Baker, B.J., Kosmidis, E.K., Vucinic, D., Falk, C.X., Cohen, L.B., Djurisic, M., and Zecevic, D. (2005). Imaging Brain Activity With Voltage- and Calcium-Sensitive Dyes. Cell. Mol. Neurobiol. *25*, 245–282.

Baker, B.J., Lee, H., Pieribone, V.A., Cohen, L.B., Isacoff, E.Y., Knopfel, T., and Kosmidis, E.K. (2007). Three fluorescent protein voltage sensors exhibit low plasma membrane expression in mammalian cells. J. Neurosci. Methods *161*, 32–38.

Baker, B.J., Mutoh, H., Dimitrov, D., Akemann, W., Perron, A., Iwamoto, Y., Jin, L., Cohen, L.B., Isacoff, E.Y., Pieribone, V.A., et al. (2008). Genetically encoded fluorescent sensors of membrane potential. Brain Cell Biol. *36*, 53.

Baker, O.S., Larsson, H.P., Mannuzzu, L.M., and Isacoff, E.Y. (1998). Three Transmembrane Conformations and Sequence-Dependent Displacement of the S4 Domain in Shaker K+ Channel Gating. Neuron *20*, 1283–1294.

Baumgartner, W., Islas, L., and Sigworth, F.J. (1999). Two-Microelectrode Voltage Clamp of Xenopus Oocytes: Voltage Errors and Compensation for Local Current Flow. Biophys. J. *77*, 1980–1991.

Bedlack, R.S., Wei, M., Fox, S.H., Gross, E., and Loew, L.M. (1994). Distinct electric potentials in soma and neurite membranes. Neuron *13*, 1187–1193.

Beene, D.L., Dougherty, D.A., and Lester, H.A. (2003). Unnatural amino acid mutagenesis in mapping ion channel function. Curr. Opin. Neurobiol. *13*, 264–270.

Bezanilla, F. (2000). The Voltage Sensor in Voltage-Dependent Ion Channels. Physiol. Rev. *80*, 555–592.

Bezanilla, F. (2002). Voltage Sensor Movements. J. Gen. Physiol. *120*, 465–473.

Bezanilla, F. (2005). Voltage-gated ion channels. IEEE Trans. Nanobioscience *4*, 34–48.

Bezanilla, F. (2008). How membrane proteins sense voltage. Nat. Rev. Mol. Cell Biol. *9*, 323–332.

Bezanilla, F. (2018). Gating currents. J. Gen. Physiol. *150*, 911–932.

Bezanilla, F., Taylor, R.E., and Fernández, J.M. (1982a). Distribution and kinetics of membrane dielectric polarization. 1. Long-term inactivation of gating currents. J. Gen. Physiol. *79*, 21–40.

Bezanilla, F., White, M.M., and Taylor, R.E. (1982b). Gating currents associated with potassium channel activation. Nature *296*, 657–659.

Bezanilla, F., Perozo, E., and Stefani, E. (1994). Gating of Shaker K+ channels: II. The components of gating currents and a model of channel activation. Biophys. J. *66*, 1011–1021.

Broomand, A., Männikkö, R., Larsson, H.P., and Elinder, F. (2003). Molecular movement of the voltage sensor in a K channel. J. Gen. Physiol. *122*, 741–748.

Bruening-Wright, A., and Larsson, H.P. (2007). Slow Conformational Changes of the Voltage Sensor during the Mode Shift in Hyperpolarization-Activated Cyclic-Nucleotide-Gated Channels. J. Neurosci. *27*, 270–278.

Brunette, A.M.J., and Farrens, D.L. (2014). Distance Mapping in Proteins Using Fluorescence Spectroscopy: Tyrosine, like Tryptophan, Quenches Bimane Fluorescence in a Distance-Dependent Manner.

Campos, F.V., Chanda, B., Roux, B., and Bezanilla, F. (2007). Two atomic constraints unambiguously position the S4 segment relative to S1 and S2 segments in the closed state of Shaker K channel. Proc. Natl. Acad. Sci. U. S. A. *104*, 7904–7909.

Cannon, S.C. (1996). Ion-channel defects and aberrant excitability in myotonia and periodic paralysis. Trends Neurosci. *19*, 3–10.

Carvalho-de-Souza, J.L., and Bezanilla, F. (2017). Voltage Dependence and Non-Sensor Residues. Biophys. J. *112*, 246a.

Catterall, W.A. (1986). Molecular Properties of Voltage-Sensitive Sodium Channels. Annu. Rev. Biochem. *55*, 953–985.

Catterall, W.A. (2010). Ion Channel Voltage Sensors: Structure, Function, and Pathophysiology. Neuron *67*, 915–928.

Cha, A., and Bezanilla, F. (1997). Characterizing Voltage-Dependent Conformational Changes in the ShakerK+ Channel with Fluorescence. Neuron *19*, 1127–1140.

Cha, A., and Bezanilla, F. (1998). Structural Implications of Fluorescence Quenching in the Shaker K+ Channel. J. Gen. Physiol. *112*, 391–408.

Cha, A., Ruben, P.C., George Jr., A.L., Fujimoto, E., and Bezanilla, F. (1999). Voltage Sensors in Domains III and IV, but Not I and II, Are Immobilized by Na+ Channel Fast Inactivation. Neuron *22*, 73–87.

Chakrapani, S., Sompornpisut, P., Intharathep, P., Roux, B., and Perozo, E. (2010). The activated state of a sodium channel voltage sensor in a membrane environment. Proc. Natl. Acad. Sci. U. S. A. *107*, 5435.

Chen, X., Wang, Q., Ni, F., and Ma, J. (2010). Structure of the full-length Shaker potassium channel Kv1.2 by normal-mode-based X-ray crystallographic refinement. Proc. Natl. Acad. Sci. *107*, 11352–11357.

Chowdhury, S., Jarecki, B.W., and Chanda, B. (2014). A Molecular Framework for Temperature-Dependent Gating of Ion Channels. Cell *158*, 1148–1158.

Cobb, M. (2002). Exorcizing the animal spirits: Jan Swammerdam on nerve function. Nat. Rev. Neurosci. *3*, 395.

Cole, K.S. (1949). Dynamic electrical characteristics of the squid axon membrane. Arch. Sci. Physiol. (Paris) *3*, 253–258.

Cole, K.S., and Curtis, H.J. (1939). Electric Impedance of the Squid Giant Axon During Activity. J. Gen. Physiol. *22*, 649–670.

Cole, K.S., and Moore, J.W. (1960). Potassium Ion Current in the Squid Giant Axon: Dynamic Characteristic. Biophys. J. *1*, 1–14.

Conti, F., and Stühmer, W. (1989). Quantal charge redistributions accompanying the structural transitions of sodium channels. Eur. Biophys. J. *17*, 53–59.

Conti, L., Renhorn, J., Gabrielsson, A., Turesson, F., Liin, S.I., Lindahl, E., and Elinder, F. (2016). Reciprocal voltage sensor-to-pore coupling leads to potassium channel C-type inactivation. Sci. Rep. *6*, 27562.

Costin, G.-E., and Hearing, V.J. (2007). Human skin pigmentation: melanocytes modulate skin color in response to stress. FASEB J. *21*, 976–994.

Davies, N.P., and Hanna, M.G. (2003). The skeletal muscle channelopathies: distinct entities and overlapping syndromes. Curr. Opin. Neurol. *16*, 559–568.

Davila, H.V., Salzberg, B.M., Cohen, L.B., and Waggoner, A.S. (1973). A Large Change in Axon Fluorescence that Provides a Promising Method for Measuring Membrane Potential. Nature. New Biol. *241*, 159–160.

Díaz-Bello, B., Rangel-García, C.I., Salvador, C., Carrisoza-Gaytán, R., and Escobar, L.I. (2013). The Polarization of the G-Protein Activated Potassium Channel GIRK5 to the Vegetal Pole of Xenopus laevis Oocytes Is Driven by a Di-Leucine Motif. PLOS ONE *8*, e64096.

Dickson, R.M., Cubitt, A.B., Tsien, R.Y., and Moerner, W.E. (1997). On/off blinking and switching behaviour of single molecules of green fluorescent protein. Nature *388*, 355–358.

Doyle, J.L., and Stubbs, L. (1998). Ataxia, arrhythmia and ion-channel gene defects. Trends Genet. *14*, 92–98.

Doyle, D.A., Cabral, J.M., Pfuetzner, R.A., Kuo, A., Gulbis, J.M., Cohen, S.L., Chait, B.T., and MacKinnon, R. (1998). The Structure of the Potassium Channel: Molecular Basis of K^+ Conduction and Selectivity. Science *280*, 69.

Fert-Bober, J., Giles, J.T., Holewinski, R.J., Kirk, J.A., Uhrigshardt, H., Crowgey, E.L., Andrade, F., Bingham, C.O., 3rd, Park, J.K., Halushka, M.K., et al. (2015). Citrullination of myofilament proteins in heart failure. Cardiovasc. Res. *108*, 232–242.

Findlay, I. (1984). A patch-clamp study of potassium channels and whole-cell currents in acinar cells of the mouse lacrimal gland. J. Physiol. *350*, 179–195.

Fisher, J.A.N., Barchi, J.R., Welle, C.G., Kim, G.-H., Kosterin, P., Obaid, A.L., Yodh, A.G., Contreras, D., and Salzberg, B.M. (2008). Two-Photon Excitation of Potentiometric Probes Enables Optical Recording of Action Potentials From Mammalian Nerve Terminals In Situ. J. Neurophysiol. *99*, 1545–1553.

Fox, A.P., Nowycky, M.C., and Tsien, R.W. (1987). Single-channel recordings of three types of calcium channels in chick sensory neurones. J. Physiol. *394*, 173–200.

Gong, Y. (2015). The Evolving Capabilities of Rhodopsin-based Genetically Encoded Voltage Indicators. Curr. Opin. Chem. Biol. *27*, 84–89.

Grabe, M., Lai, H.C., Jain, M., Nung Jan, Y., and Yeh Jan, L. (2006). Structure prediction for the down state of a potassium channel voltage sensor. Nature *445*, 550.

Green, M.B., translated by Stephanie (2018). How Meghan Markle has made freckles the hottest new beauty trend.

Grinvald, A., and Hildesheim, R. (2004). VSDI: a new era in functional imaging of cortical dynamics. Nat. Rev. Neurosci. *5*, 874–885.

Grosenick, L., Marshel, J.H., and Deisseroth, K. (2015). Closed-Loop and Activity-Guided Optogenetic Control. Neuron *86*, 106–139.

Gurdon, J.B., Lane, C.D., Woodland, H.R., and Marbaix, G. (1971). Use of Frog Eggs and Oocytes for the Study of Messenger RNA and its Translation in Living Cells. Nature *233*, 177–182.

Guy, H.R., and Seetharamulu, P. (1986). Molecular model of the action potential sodium channel. Proc. Natl. Acad. Sci. *83*, 508.

Hamill, O.P., Marty, A., Neher, E., Sakmann, B., and Sigworth, F.J. (1981). Improved patch-clamp techniques for high-resolution current recording from cells and cell-free membrane patches. Pflugers Arch. *391*, 85–100.

Hartshorne, R.P., and Catterall, W.A. (1981). Purification of the saxitoxin receptor of the sodium channel from rat brain. Proc. Natl. Acad. Sci. U. S. A. *78*, 4620–4624.

Henrion, U., Renhorn, J., Börjesson, S.I., Nelson, E.M., Schwaiger, C.S., Bjelkmar, P., Wallner, B., Lindahl, E., and Elinder, F. (2012). Tracking a complete voltage-sensor cycle with metal-ion bridges. Proc. Natl. Acad. Sci. *109*, 8552–8557.

Hess, P., Lansman, J.B., and Tsien, R.W. (1986). Calcium channel selectivity for divalent and monovalent cations. Voltage and concentration dependence of single channel current in ventricular heart cells. J. Gen. Physiol. *88*, 293–319.

Hille, B. (1970). Ionic channels in nerve membranes. Prog. Biophys. Mol. Biol. *21*, 1–32.

Hochbaum, D.R., Zhao, Y., Farhi, S.L., Klapoetke, N., Werley, C.A., Kapoor, V., Zou, P., Kralj, J.M., Maclaurin, D., Smedemark-Margulies, N., et al. (2014). All-optical electrophysiology in mammalian neurons using engineered microbial rhodopsins. Nat. Methods *11*, 825–833.

Hodgkin, A.L., and Huxley, A.F. (1939). Action Potentials Recorded from Inside a Nerve Fibre. Nature *144*, 710.

Hodgkin, A.L., and Huxley, A.F. (1952). A quantitative description of membrane current and its application to conduction and excitation in nerve. J. Physiol. *117*, 500–544.

Hodgkin, A.L., and Katz, B. (1949). The effect of sodium ions on the electrical activity of the giant axon of the squid. J. Physiol. *108*, 37–77.

Hodgkin, A.L., Huxley, A.F., and Katz, B. (1952). Measurement of current-voltage relations in the membrane of the giant axon of Loligo. J. Physiol. *116*, 424–448.

Holmgren, M., Shin, K.S., and Yellen, G. (1998). The Activation Gate of a Voltage-Gated K+ Channel Can Be Trapped in the Open State by an Intersubunit Metal Bridge. Neuron *21*, 617–621.

Hong, K.H., and Miller, C. (2000). The Lipid–Protein Interface of aShaker K+ Channel. J. Gen. Physiol. *115*, 51–58.

Horng, T.-L., Eisenberg, R.S., Liu, C., and Bezanilla, F. (2017). Continuum gating current models computed with consistent interactions.

Hoshi, T., and Armstrong, C.M. (2015). The Cole-Moore Effect: Still Unexplained? Biophys. J. *109*, 1312–1316.

Hughes, L.D., Rawle, R.J., and Boxer, S.G. (2014). Choose Your Label Wisely: Water-Soluble Fluorophores Often Interact with Lipid Bilayers. PLOS ONE *9*, e87649.

Infield, D.T., Lee, E.E.L., Galpin, J.D., Galles, G.D., Bezanilla, F., and Ahern, C.A. (2018). Replacing voltage sensor arginines with citrulline provides mechanistic insight into charge versus shape. J. Gen. Physiol. jgp.201812075.

Ingber, D.E. (1997). TENSEGRITY: THE ARCHITECTURAL BASIS OF CELLULAR MECHANOTRANSDUCTION. Annu. Rev. Physiol. *59*, 575–599.

Islas, L.D., and Zagotta, W.N. (2006). Short-range molecular rearrangements in ion channels detected by tryptophan quenching of bimane fluorescence. J. Gen. Physiol. *128*, 337–346.

Jiang, X., Wang, G., Lee, A.J., Stornetta, R.L., and Zhu, J.J. (2013). The organization of two new cortical interneuronal circuits. Nat. Neurosci. *16*, 210–218.

Jiang, Y., Ruta, V., Chen, J., Lee, A., and MacKinnon, R. (2003a). The principle of gating charge movement in a voltage-dependent K+ channel. Nature *423*, 42–48.

Jiang, Y., Lee, A., Chen, J., Ruta, V., Cadene, M., Chait, B.T., and MacKinnon, R. (2003b). X-ray structure of a voltage-dependent K+ channel. Nature *423*, 33–41.

Jin, L., Han, Z., Platisa, J., Wooltorton, J.R.A., Cohen, L.B., and Pieribone, V.A. (2012). Single action potentials and subthreshold electrical events imaged in neurons with a novel fluorescent protein voltage probe. Neuron *75*, 779–785.

Kalstrup, T., and Blunck, R. (2013). Dynamics of internal pore opening in KV channels probed by a fluorescent unnatural amino acid. Proc. Natl. Acad. Sci. *110*, 8272–8277.

Keynes, R.D. (1951). The ionic movements during nervous activity. J. Physiol. *114*, 119–150.

Keynes, R.D., and Elinder, F. (1999). The screw-helical voltage gating of ion channels. Proc. R. Soc. B Biol. Sci. *266*, 843–852.

Khalili-Araghi, F., Jogini, V., Yarov-Yarovoy, V., Tajkhorshid, E., Roux, B., and Schulten, K. (2010). Calculation of the Gating Charge for the Kv1.2 Voltage-Activated Potassium Channel. Biophys. J. *98*, 2189–2198.

Kim, R.Y., Pless, S.A., and Kurata, H.T. (2017). PIP2 mediates functional coupling and pharmacology of neuronal KCNQ channels. Proc. Natl. Acad. Sci. U. S. A. *114*, E9702–E9711.

Kohout, S.C., Ulbrich, M.H., Bell, S.C., and Isacoff, E.Y. (2008). Subunit organization and functional transitions in Ci-VSP. Nat. Struct. Mol. Biol. *15*, 106–108.

Konnerth, A., Obaid, A.L., and Salzberg, B.M. (1987). Optical recording of electrical activity from parallel fibres and other cell types in skate cerebellar slices in vitro. J. Physiol. *393*, 681–702.

Kralj, J.M., Douglass, A.D., Hochbaum, D.R., Maclaurin, D., and Cohen, A.E. (2011). Optical recording of action potentials in mammalian neurons using a microbial rhodopsin. Nat. Methods *9*, 90–95.

Kubota, T., Lacroix, J.J., Bezanilla, F., and Correa, A.M. (2014). Probing α-310 Transitions in a Voltage-Sensing S4 Helix. Biophys. J. *107*, 1117–1128.

Kubota, T., Durek, T., Dang, B., Finol-Urdaneta, R.K., Craik, D.J., Kent, S.B.H., French, R.J., Bezanilla, F., and Correa, A.M. (2017). Mapping of voltage sensor positions in resting and inactivated mammalian sodium channels by LRET. Proc. Natl. Acad. Sci. *114*, E1857–E1865.

Kuhn, B., Denk, W., and Bruno, R.M. (2008). In vivo two-photon voltage-sensitive dye imaging reveals top-down control of cortical layers 1 and 2 during wakefulness. Proc. Natl. Acad. Sci. *105*, 7588–7593.

Kume, S., Muto, A., Aruga, J., Nakagawa, T., Michikawa, T., Furuichi, T., Nakade, S., Okano, H., and Mikoshiba, K. (1993). The Xenopus IP3 receptor: Structure, function, and localization in oocytes and eggs. Cell *73*, 555–570.

Kusano, K., Miledi, R., and Stinnakre, J. (1977). Acetylcholine receptors in the oocyte membrane. Nature *270*, 739–741.

Labro, A.J., Lacroix, J.J., Villalba-Galea, C.A., Snyders, D.J., and Bezanilla, F. (2012). Molecular mechanism for depolarization-induced modulation of Kv channel closure. J. Gen. Physiol. *140*, 481–493.

Lacroix, J.J., and Bezanilla, F. (2011). Control of a final gating charge transition by a hydrophobic residue in the S2 segment of a K+ channel voltage sensor. Proc. Natl. Acad. Sci. U. S. A. *108*, 6444–6449.

Lacroix, J.J., and Bezanilla, F. (2012). Tuning the Voltage-Sensor Motion with a Single Residue. Biophys. J. *103*, L23–L25.

Lacroix, J.J., Labro, A.J., and Bezanilla, F. (2011). Properties of deactivation gating currents in Shaker channels. Biophys. J. *100*, L28–L30.

Lacroix, J.J., Pless, S.A., Maragliano, L., Campos, F.V., Galpin, J.D., Ahern, C.A., Roux, B., and Bezanilla, F. (2012). Intermediate state trapping of a voltage sensor. J. Gen. Physiol. *140*, 635–652.

Lacroix, J.J., Hyde, H.C., Campos, F.V., and Bezanilla, F. (2014). Moving gating charges through the gating pore in a Kv channel voltage sensor. Proc. Natl. Acad. Sci. *111*, E1950–E1959.

Lainé, M., Lin, M.A., Bannister, J.P.A., Silverman, W.R., Mock, A.F., Roux, B., and Papazian, D.M. (2003). Atomic proximity between S4 segment and pore domain in Shaker potassium channels. Neuron *39*, 467–481.

Larsson, H.P., Baker, O.S., Dhillon, D.S., and Isacoff, E.Y. (1996). Transmembrane movement of the Shaker K+ channel S4. Neuron *16*, 387–397.

Latorre, R., Ehrenstein, G., and Lecar, H. (1972). Ion Transport Through Excitability-Inducing Material (EIM) Channels in Lipid Bilayer Membranes. J. Gen. Physiol. *60*, 72.

Lecar, H., Larsson, H.P., and Grabe, M. (2003). Electrostatic Model of S4 Motion in Voltage-Gated Ion Channels. Biophys. J. *85*, 2854–2864.

Lee, E.E.L., and Bezanilla, F. (2017). Biophysical Characterization of Genetically Encoded Voltage Sensor ASAP1: Dynamic Range Improvement. Biophys. J. *113*, 2178–2181.

Leisle, L., Valiyaveetil, F., Mehl, R.A., and Ahern, C.A. (2015). Incorporation of Non-Canonical Amino Acids. In Novel Chemical Tools to Study Ion Channel Biology, C. Ahern, and S. Pless, eds. (New York, NY: Springer New York), pp. 119–151.

Leisle, L., Chadda, R., Lueck, J.D., Infield, D.T., Galpin, J.D., Krishnamani, V., Robertson, J.L., and Ahern, C.A. (2016). Cellular encoding of Cy dyes for single-molecule imaging. ELife *5*, e19088.

Lerche, H., Shah, M., Beck, H., Noebels, J., Johnston, D., and Vincent, A. (2013). Ion channels in genetic and acquired forms of epilepsy. J. Physiol. *591*, 753–764.

Li, Q., Wanderling, S., Paduch, M., Medovoy, D., Singharoy, A., McGreevy, R., Villalba-Galea, C.A., Hulse, R.E., Roux, B., Schulten, K., et al. (2014). Structural mechanism of voltage-dependent gating in an isolated voltage-sensing domain. Nat. Struct. Mol. Biol. *21*, 244–252.

Liao, M.-L.C., Boer, T.P. de, Mutoh, H., Raad, N., Richter, C., Wagner, E., Downie, B.R., Unsöld, B., Arooj, I., Streckfuss-Bömeke, K., et al. (2015). Sensing Cardiac Electrical Activity With a Cardiac Myocyte–Targeted Optogenetic Voltage Indicator. Circ. Res.

Lin, M.Z., and Schnitzer, M.J. (2016). Genetically encoded indicators of neuronal activity. Nat. Neurosci. *19*, 1142–1153.

Liu Yanlan, Ai Kelong, Liu Jianhua, Deng Mo, He Yangyang, and Lu Lehui (2012). Dopamine-Melanin Colloidal Nanospheres: An Efficient Near-Infrared Photothermal Therapeutic Agent for In Vivo Cancer Therapy. Adv. Mater. *25*, 1353–1359.

Lock, J.T., Parker, I., and Smith, I.F. (2015). A comparison of fluorescent Ca2+ indicators for imaging local Ca2+ signals in cultured cells. Cell Calcium *58*, 638–648.

Long, S.B., Campbell, E.B., and MacKinnon, R. (2005). Crystal Structure of a Mammalian Voltage-Dependent Shaker Family K+ Channel. Science *309*, 897–903.

Long, S.B., Tao, X., Campbell, E.B., and MacKinnon, R. (2007). Atomic structure of a voltage-dependent K+ channel in a lipid membrane-like environment. Nature *450*, 376.

Lundby, A., Akemann, W., and Knöpfel, T. (2010). Biophysical characterization of the fluorescent protein voltage probe VSFP2.3 based on the voltage-sensing domain of Ci-VSP. Eur. Biophys. J. *39*, 1625–1635.

Maljevic, S., and Lerche, H. (2013). Potassium channels: a review of broadening therapeutic possibilities for neurological diseases. J. Neurol. *260*, 2201–2211.

Mannuzzu, L.M., Moronne, M.M., and Isacoff, E.Y. (1996). Direct Physical Measure of Conformational Rearrangement Underlying Potassium Channel Gating. Science *271*, 213.

Mansoor, S.E., Mchaourab, H.S., and Farrens, D.L. (1999). Determination of Protein Secondary Structure and Solvent Accessibility Using Site-Directed Fluorescence Labeling. Studies of T4 Lysozyme Using the Fluorescent Probe Monobromobimane. Biochemistry *38*, 16383–16393.

Mansoor, S.E., Mchaourab, H.S., and Farrens, D.L. (2002). Mapping Proximity within Proteins Using Fluorescence Spectroscopy. A Study of T4 Lysozyme Showing That Tryptophan Residues Quench Bimane Fluorescence. Biochemistry *41*, 2475–2484.

Mansoor, S.E., DeWitt, M.A., and Farrens, D.L. (2010). Distance Mapping in Proteins Using Fluorescence Spectroscopy: The Tryptophan-Induced Quenching (TrIQ) Method. Biochemistry *49*, 9722–9731.

Marmont, G. (1949). Studies on the axon membrane. I. A new method. J. Cell. Comp. Physiol. *34*, 351–382.

Martinez-Pinna, J., Tolhurst, G., Gurung, I.S., Vandenberg, J.I., and Mahaut-Smith, M.P. (2004). Sensitivity limits for voltage control of P2Y receptor-evoked Ca2+ mobilization in the rat megakaryocyte. J. Physiol. *555*, 61–70.

McCormack, K., Joiner, W.I., and Heinemann, S.H. (1994). A characterization of the activating structural rearrangements in voltage-dependent Shaker K+ channels. Neuron *12*, 301–315.

Menny, A., Lefebvre, S.N., Schmidpeter, P.A., Drège, E., Fourati, Z., Delarue, M., Edelstein, S.J., Nimigean, C.M., Joseph, D., and Corringer, P.-J. (2017). Identification of a pre-active conformation of a pentameric channel receptor. ELife *6*, e23955.

Miller, C. (1978). Voltage-gated cation conductance channel from fragmented sarcoplasmic reticulum: steady-state electrical properties. J. Membr. Biol. *40*, 1–23.

Moerner, W. e., Peterman, E. j. g., Brasselet, S., Kummer, S., and Dickson, R. m. (1999). Optical methods for exploring dynamics of single copies of green fluorescent protein. Cytometry *36*, 232–238.

Mujahid, N., Liang, Y., Murakami, R., Choi, H.G., Dobry, A.S., Wang, J., Suita, Y., Weng, Q.Y., Allouche, J., Kemeny, L.V., et al. (2017). A UV-Independent Topical Small-Molecule Approach for Melanin Production in Human Skin. Cell Rep. *19*, 2177–2184.

Murata, Y., Iwasaki, H., Sasaki, M., Inaba, K., and Okamura, Y. (2005). Phosphoinositide phosphatase activity coupled to an intrinsic voltage sensor. Nature *435*, 1239–1243.

Narahashi, T., Moore, J.W., and Scott, W.R. (1964). Tetrodotoxin Blockage of Sodium Conductance Increase in Lobster Giant Axons. J. Gen. Physiol. *47*, 965–974.

Neher, E. (1982). Unit conductance studies in biological membranes (Elsevier/North Holland Scientific Publishers).

Neher, E., and Sakmann, B. (1976). Single-channel currents recorded from membrane of denervated frog muscle fibres. Nature *260*, 799.

Noda, M., Shimizu, S., Tanabe, T., Takai, T., Kayano, T., Ikeda, T., Takahashi, H., Nakayama, H., Kanaoka, Y., Minamino, N., et al. (1984). Primary structure of Electrophorus electricus sodium channel deduced from cDNA sequence. Nature *312*, 121.

Noren, C., Anthony-Cahill, S., Griffith, M., and Schultz, P. (1989). A general method for site-specific incorporation of unnatural amino acids into proteins. Science *244*, 182.

Okamura, Y., Nishino, A., Murata, Y., Nakajo, K., Iwasaki, H., Ohtsuka, Y., Tanaka-Kunishima, M., Takahashi, N., Hara, Y., Yoshida, T., et al. (2005). Comprehensive analysis of the ascidian genome reveals novel insights into the molecular evolution of ion channel genes. Physiol. Genomics *22*, 269–282.

Osteen, J.D., Gonzalez, C., Sampson, K.J., Iyer, V., Rebolledo, S., Larsson, H.P., and Kass, R.S. (2010). KCNE1 alters the voltage sensor movements necessary to open the KCNQ1 channel gate. Proc. Natl. Acad. Sci. *107*, 22710–22715.

Ozawa, S., Kimura, T., Nozaki, T., Harada, H., Shimada, I., and Osawa, M. (2015). Structural basis for the inhibition of voltage-dependent K+ channel by gating modifier toxin. Sci. Rep. *5*.

Pan, X., Li, Z., Zhou, Q., Shen, H., Wu, K., Huang, X., Chen, J., Zhang, J., Zhu, X., Lei, J., et al. (2018). Structure of the human voltage-gated sodium channel Nav1.4 in complex with β1. Science eaau2486.

Pantazis, A., Savalli, N., Sigg, D., Neely, A., and Olcese, R. (2014). Functional heterogeneity of the four voltage sensors of a human L-type calcium channel. Proc. Natl. Acad. Sci. U. S. A. *111*, 18381–18386.

Pantoja, R., Sigg, D., Blunck, R., Bezanilla, F., and Heath, J.R. (2001). Bilayer Reconstitution of Voltage-Dependent Ion Channels using a Microfabricated Silicon Chip. Biophys. J. *81*, 2389–2394.

Papazian, D., Schwarz, T., Tempel, B., Jan, Y., and Jan, L. (1987). Cloning of genomic and complementary DNA from Shaker, a putative potassium channel gene from Drosophila. Science *237*, 749.

Papazian, D.M., Timpe, L.C., Jan, Y.N., and Jan, L.Y. (1991). Alteration of voltage-dependence of Shaker potassium channel by mutations in the S4 sequence. Nature *349*, 305.

Pathak, M.M., Yarov-Yarovoy, V., Agarwal, G., Roux, B., Barth, P., Kohout, S., Tombola, F., and Isacoff, E.Y. (2007). Closing in on the resting state of the Shaker K+ channel. Neuron *56*, 124–140.

Pédelacq, J.-D., Cabantous, S., Tran, T., Terwilliger, T.C., and Waldo, G.S. (2006). Engineering and characterization of a superfolder green fluorescent protein. Nat. Biotechnol. *24*, 79–88.

Perin, R., Berger, T.K., and Markram, H. (2011). A synaptic organizing principle for cortical neuronal groups. Proc. Natl. Acad. Sci. *108*, 5419.

Perozo, E., MacKinnon, R., Bezanilla, F., and Stefani, E. (1993). Gating currents from a nonconducting mutant reveal open-closed conformations in Shaker K+ channels. Neuron *11*, 353–358.

Peters, C.J., Vaid, M., Horne, A.J., Fedida, D., and Accili, E.A. (2009). The molecular basis for the actions of KVβ1.2 on the opening and closing of the KV1.2 delayed rectifier channel. Channels *3*, 314–322.

Pettersen, E.F., Goddard, T.D., Huang, C.C., Couch, G.S., Greenblatt, D.M., Meng, E.C., and Ferrin, T.E. (2004). UCSF Chimera--a visualization system for exploratory research and analysis. J. Comput. Chem. *25*, 1605–1612.

Phillips, L.R., and Swartz, K.J. (2010). Position and motions of the S4 helix during opening of the Shaker potassium channel. J. Gen. Physiol. *136*, 629–644.

Pless, S.A., and Ahern, C.A. (2013). Unnatural Amino Acids as Probes of Ligand-Receptor Interactions and Their Conformational Consequences. Annu. Rev. Pharmacol. Toxicol. *53*, 211–229.

Pless, S.A., Galpin, J.D., Frankel, A., and Ahern, C.A. (2011). Molecular basis for class Ib anti-arrhythmic inhibition of cardiac sodium channels. Nat. Commun. *2*, 351.

Preuss, S., and Stein, W. (2013). Comparison of Two Voltage-Sensitive Dyes and Their Suitability for Long-Term Imaging of Neuronal Activity. PLOS ONE *8*, e75678.

Priest, M., and Bezanilla, F. (2015). Functional Site-Directed Fluorometry. In Novel Chemical Tools to Study Ion Channel Biology, C. Ahern, and S. Pless, eds. (Springer New York), pp. 55–76.

Pucihar, G., Kotnik, T., and Miklavcic, D. (2009). Measuring the induced membrane voltage with Di-8-ANEPPS. J. Vis. Exp. JoVE 1659.

Rohr, S., and Salzberg, B.M. (1994). Multiple site optical recording of transmembrane voltage (MSORTV) in patterned growth heart cell cultures: assessing electrical behavior, with microsecond resolution, on a cellular and subcellular scale. Biophys. J. *67*, 1301–1315.

Rojas, E., and Armstrong, C. (1971). Sodium conductance activation without inactivation in pronase-perfused axons. Nature. New Biol. *229*, 177.

Ryu, Y., and Schultz, P.G. (2006). Efficient incorporation of unnatural amino acids into proteins in Escherichia coli. Nat. Methods *3*, 263.

Sakai, R., Repunte-Canonigo, V., Raj, C.D., and Knöpfel, T. (2001). Design and characterization of a DNA-encoded, voltage-sensitive fluorescent protein. Eur. J. Neurosci. *13*, 2314–2318.

Sakmann, B., and Neher, E. (1984). Patch Clamp Techniques for Studying Ionic Channels in Excitable Membranes. Annu. Rev. Physiol. *46*, 455–472.

Salzberg, B., Obaid, A., and Bezanilla, F. (1993). Microsecond response of a voltage-sensitive merocyanine dye: fast voltage-clamp measurements on squid giant axon. Jpn. J. Physiol. *43*, S37-41.

Savalli, N., Kondratiev, A., Toro, L., and Olcese, R. (2006). Voltage-dependent conformational changes in human Ca2+- and voltage-activated K+ channel, revealed by voltage-clamp fluorometry. Proc. Natl. Acad. Sci. *103*, 12619–12624.

Schönherr, R., Mannuzzu, L.M., Isacoff, E.Y., and Heinemann, S.H. (2002). Conformational Switch between Slow and Fast Gating Modes: Allosteric Regulation of Voltage Sensor Mobility in the EAG K+ Channel. Neuron *35*, 935–949.

Schwaiger, C.S., Bjelkmar, P., Hess, B., and Lindahl, E. (2011). 310-Helix Conformation Facilitates the Transition of a Voltage Sensor S4 Segment toward the Down State. Biophys. J. *100*, 1446–1454.

Semenova, N.P., Abarca-Heidemann, K., Loranc, E., and Rothberg, B.S. (2009). Bimane Fluorescence Scanning Suggests Secondary Structure near the S3-S4 Linker of BK Channels. J. Biol. Chem. *284*, 10684–10693.

Seoh, S.-A., Sigg, D., Papazian, D.M., and Bezanilla, F. (1996). Voltage-Sensing Residues in the S2 and S4 Segments of the Shaker K+ Channel. Neuron *16*, 1159–1167.

Siegel, M.S., and Isacoff, E.Y. (1997). A Genetically Encoded Optical Probe of Membrane Voltage. Neuron *19*, 735–741.

Sigg, D., Stefani, E., and Bezanilla, F. (1994). Gating current noise produced by elementary transitions in Shaker potassium channels. Science *264*, 578.

Sigworth, F.J., and Neher, E. (1980). Single Na+ channel currents observed in cultured rat muscle cells. Nature *287*, 447.

Sindelka, R., Abaffy, P., Qu, Y., Tomankova, S., Sidova, M., Naraine, R., Kolar, M., Peuchen, E., Sun, L., Dovichi, N., et al. (2018). Asymmetric distribution of biomolecules of maternal origin in the Xenopus laevis egg and their impact on the developmental plan. Sci. Rep. *8*, 8315.

Skou, J.C. (1957). The influence of some cations on an adenosine triphosphatase from peripheral nerves. Biochim. Biophys. Acta *23*, 394–401.

Smirnova, I., Kasho, V., and Kaback, H.R. (2014). Real-time conformational changes in LacY. Proc. Natl. Acad. Sci. *111*, 8440–8445.

Smith, P.L., and Yellen, G. (2002). Fast and Slow Voltage Sensor Movements in HERG Potassium Channels. J. Gen. Physiol. *119*, 275–293.

Sonnleitner, A., Mannuzzu, L.M., Terakawa, S., and Isacoff, E.Y. (2002). Structural rearrangements in single ion channels detected optically in living cells. Proc. Natl. Acad. Sci. *99*, 12759–12764.

Starace, D.M., and Bezanilla, F. (2001). Histidine Scanning Mutagenesis of Basic Residues of the S4 Segment of the Shaker K+ Channel. J. Gen. Physiol. *117*, 469–490.

Stefani, E., and Bezanilla, F. (1998). [17] Cut-open oocyte voltage-clamp technique. B.-M. in Enzymology, ed. (Academic Press), pp. 300–318.

St-Pierre, F., Marshall, J.D., Yang, Y., Gong, Y., Schnitzer, M.J., and Lin, M.Z. (2014). High-fidelity optical reporting of neuronal electrical activity with an ultrafast fluorescent voltage sensor. Nat. Neurosci. *17*, 884–889.

Stühmer, W., and Parekh, A.B. (1995). Electrophysiological Recordings from Xenopus Oocytes. In Single-Channel Recording, B. Sakmann, and E. Neher, eds. (Boston, MA: Springer US), pp. 341–356.

Stühmer, W., Conti, F., Suzuki, H., Wang, X., Noda, M., Yahagi, N., Kubo, H., and Numa, S. (1989). Structural parts involved in activation and inactivation of the sodium channel. Nature *339*, 597.

Tao, X., Lee, A., Limapichat, W., Dougherty, D.A., and MacKinnon, R. (2010a). A Gating Charge Transfer Center in Voltage Sensors. Science *328*, 67–73.

Tao, X., Lee, A., Limapichat, W., Dougherty, D.A., and MacKinnon, R. (2010b). A gating charge transfer center in voltage sensors. Science *328*, 67–73.

Tasaki, I., and Hagiwara, A.S. (1957). Demonstration of two stable potential states in the squid giant axon under tetraethylammonium chloride. J. Gen. Physiol. *40*, 859–885.

Timpe, L.C., Schwarz, T.L., Tempel, B.L., Papazian, D.M., Jan, Y.N., and Jan, L.Y. (1988). Expression of functional potassium channels from Shaker cDNA in Xenopus oocytes. Nature *331*, 143.

Tombola, F., Pathak, M.M., Gorostiza, P., and Isacoff, E.Y. (2006). The twisted ion-permeation pathway of a resting voltage-sensing domain. Nature *445*, 546.

Toseland, C.P. (2013). Fluorescent labeling and modification of proteins. J. Chem. Biol. *6*, 85–95.

Treger, J.S., Priest, M.F., and Bezanilla, F. (2015). Single-molecule fluorimetry and gating currents inspire an improved optical voltage indicator. ELife *4*, e10482.

Vaid, M., Claydon, T.W., Rezazadeh, S., and Fedida, D. (2008). Voltage Clamp Fluorimetry Reveals a Novel Outer Pore Instability in a Mammalian Voltage-gated Potassium Channel. J. Gen. Physiol. *132*, 209–222.

Vargas, E., Bezanilla, F., and Roux, B. (2011). In search of a consensus model of the resting state of a voltage-sensing domain. Neuron *72*, 713–720.

Vargas, E., Yarov-Yarovoy, V., Khalili-Araghi, F., Catterall, W.A., Klein, M.L., Tarek, M., Lindahl, E., Schulten, K., Perozo, E., Bezanilla, F., et al. (2012). An emerging consensus on voltage-dependent gating from computational modeling and molecular dynamics simulations. J. Gen. Physiol. *140*, 587–594.

Verkhratsky, A., Krishtal, O.A., and Petersen, O.H. (2006). From Galvani to patch clamp: the development of electrophysiology. Pflüg. Arch. *453*, 233–247.

Vernino, S., Amador, M., Luetje, C.W., Patrick, J., and Dani, J.A. (1992). Calcium modulation and high calcium permeability of neuronal nicotinic acetylcholine receptors. Neuron *8*, 127–134.

Villalba-Galea, C.A., Sandtner, W., Starace, D.M., and Bezanilla, F. (2008). S4-based voltage sensors have three major conformations. Proc. Natl. Acad. Sci. U. S. A. *105*, 17600–17607.

Villalba-Galea, C.A., Sandtner, W., Dimitrov, D., Mutoh, H., Knöpfel, T., and Bezanilla, F. (2009). Charge Movement of a Voltage-Sensitive Fluorescent Protein. Biophys. J. *96*, L19–L21.

Wang, H.-W., and Wang, J.-W. (2016). How cryo-electron microscopy and X-ray crystallography complement each other. Protein Sci. *26*, 32–39.

Wang, H.-G., Zhu, W., Kanter, R.J., Silva, J.R., Honeywell, C., Gow, R.M., and Pitt, G.S. (2016). A novel NaV1.5 voltage sensor mutation associated with severe atrial and ventricular arrhythmias. J. Mol. Cell. Cardiol. *92*, 52–62.

Yaghoobi, R., Omidian, M., and Bagherani, N. (2011). Vitiligo: A review of the published work. J. Dermatol. *38*, 419–431.

Yang, H.H., and St-Pierre, F. (2016). Genetically Encoded Voltage Indicators: Opportunities and Challenges. J. Neurosci. *36*, 9977–9989.

Yang, H.H., St-Pierre, F., Sun, X., Ding, X., Lin, M.Z., and Clandinin, T.R. (2016). Subcellular Imaging of Voltage and Calcium Signals Reveals Neural Processing In Vivo. Cell *166*, 245–257.

Yang, N., George, A.L., Jr., and Horn, R. (1996). Molecular Basis of Charge Movement in Voltage-Gated Sodium Channels. Neuron *16*, 113–122.

Yang, Y., Yan, Y., and Sigworth, F.J. (1997). How Does the W434F Mutation Block Current in Shaker Potassium Channels? J. Gen. Physiol. *109*, 779–789.

Yao, X., Parnot, C., Deupi, X., Ratnala, V.R.P., Swaminath, G., Farrens, D., and Kobilka, B. (2006). Coupling ligand structure to specific conformational switches in the β2-adrenoceptor. Nat. Chem. Biol. *2*, 417–422.

Young, J.Z. (1938). The Functioning of the Giant Nerve Fibres of the Squid. J. Exp. Biol. *15*, 170–185.

Zeise, L., Murr, B.L., and Chedekel, M.R. (1992). Melanin standard method: particle description. Pigment Cell Res. *5*, 132–142.

Zhang, X., Ren, W., DeCaen, P., Yan, C., Tao, X., Tang, L., Wang, J., Hasegawa, K., Kumasaka, T., He, J., et al. (2012). Crystal structure of NavAP, an orthologue of the NaChBac voltage-gated sodium channel. Nature *486*, 130–134.

Zheng, J., and Zagotta, W.N. (2000). Gating Rearrangements in Cyclic Nucleotide-Gated Channels Revealed by Patch-Clamp Fluorometry. Neuron *28*, 369–374.

Appendix

Mutations	ASAP1 mutation	Intended effect	Actual effect
I162F (CiVSP)	**I66F**	**Accelerate deactivation kinetics**	**No QV split, slower kinetic**
F290X (Shaker)	**F101X**	**Hydrophobic plug, general acceleration**	**Mostly reduced signal size**
R217X (CiVSP)	**Q153X**	**Tune the voltage dependence**	**Split QVs, small QV shifts**
V363T (Shaker)	**V160S**	**Accelerate activation kinetics**	**Slight speed up in kinetics, still split QV**
L361X (Shaker)	**L158X**	**Tune the voltage dependence**	**No QV split, faster kinetics**
S240L (Shaker)	**D69A**	**Alters charge movement**	**Flipped signal, but much smaller signal**
V358X (Shaker)	**V155X**	**Tune the voltage dependence**	**No QV split, much smaller signal**

Table 2.2 - Attempted mutations to improve ASAP1

Table 3.1 A- Figure 1B

One-way ANOVA	
DoF	7,92
F	75.36
P	< 0.0001
Statistical Significance	****

Tukey's multiple comparisons test	Mean Diff.	95% CI of diff.	Summary
1 vs. 2	8.946	-10.33 to 28.22	ns
1 vs. 3	7.143	-13.47 to 27.75	ns
1 vs. 4	19.46	-2.151 to 41.08	ns
1 vs. 5	34.65	14.80 to 54.51	****
1 vs. 6	34.93	11.89 to 57.97	***
1 vs. 7	42.71	19.67 to 65.76	****
1 vs. 8	43.52	23.66 to 63.38	****
2 vs. 3	-1.803	-21.08 to 17.47	ns
2 vs. 4	10.52	-9.832 to 30.87	ns
2 vs. 5	25.71	7.234 to 44.18	**

2 vs. 6	25.98	4.125 to 47.84	*
2 vs. 7	33.77	11.91 to 55.63	***
2 vs. 8	34.57	16.10 to 53.05	****
3 vs. 4	12.32	-9.294 to 33.94	ns
3 vs. 5	27.51	7.652 to 47.37	**
3 vs. 6	27.79	4.745 to 50.83	**
3 vs. 7	35.57	12.53 to 58.61	***
3 vs. 8	36.37	16.52 to 56.23	****
4 vs. 5	15.19	-5.711 to 36.09	ns
4 vs. 6	15.47	-8.479 to 39.41	ns
4 vs. 7	23.25	-0.6952 to 47.20	ns
4 vs. 8	24.05	3.153 to 44.96	*
5 vs. 6	0.2757	-22.10 to 22.65	ns
5 vs. 7	8.06	-14.31 to 30.43	ns
5 vs. 8	8.864	-10.22 to 27.94	ns
6 vs. 7	7.784	-17.46 to 33.02	ns
6 vs. 8	8.588	-13.79 to 30.96	ns
7 vs. 8	0.8041	-21.57 to 23.18	ns

Table 3.2 B - Figure 1C

One-way ANOVA	
DoF	7,39
F	14.18
P	< 0.0001
Statistical significance	****

Tukey's multiple comparisons test	**Mean Diff.**	**95% CI of diff.**	**Summary**
1 vs. 2	277.2	184.5 to 369.8	****
1 vs. 3	292.3	206.6 to 378.1	****
1 vs. 4	299.5	222.0 to 377.0	****
1 vs. 5	404.8	309.1 to 500.5	****
1 vs. 6	439.9	336.3 to 543.4	****
1 vs. 7	566.5	462.9 to 670.1	****
1 vs. 8	601	492.1 to 709.9	****
2 vs. 3	15.17	-85.92 to 116.3	ns
2 vs. 4	22.3	-71.88 to 116.5	ns
2 vs. 5	127.6	17.95 to 237.2	*

2 vs. 6	162.7	46.09 to 279.3	***
2 vs. 7	289.3	172.7 to 405.9	****
2 vs. 8	323.8	202.5 to 445.1	****
3 vs. 4	7.131	-80.30 to 94.56	ns
3 vs. 5	112.4	8.526 to 216.3	*
3 vs. 6	147.5	36.30 to 258.7	**
3 vs. 7	274.1	162.9 to 385.3	****
3 vs. 8	308.6	192.5 to 424.8	****
4 vs. 5	105.3	8.105 to 202.5	*
4 vs. 6	140.4	35.41 to 245.3	**
4 vs. 7	267	162.0 to 372.0	****
4 vs. 8	301.5	191.3 to 411.7	****
5 vs. 6	35.09	-83.92 to 154.1	ns
5 vs. 7	161.7	42.69 to 280.7	**
5 vs. 8	196.2	72.57 to 319.9	****
6 vs. 7	126.6	1.157 to 252.1	*
6 vs. 8	161.1	31.27 to 291.0	**
7 vs. 8	34.52	-95.34 to 164.4	ns

Table 3.3 C - Figure 2B

One-way ANOVA	
DoF	5,74
F	20.35
P	< 0.0001
Statistical Significance	****

Holm- Sidak's multiple comparisons test	**Mean Diff.**	**95% CI of diff.**	**Summary**
Uninjected vs. DMSO injected	-1.454	-137.0 to 134.1	ns
Uninjected vs. DMSO injected	-66.43	-168.5 to 35.61	ns
Uninjected vs. DMSO injected	20.74	-111.5 to 153.0	ns

Table 3.4 D - Figure 2C

One-way ANOVA	
DoF	4,87
F	11.17
P	< 0.0001
Statistical Significance	****

Holm-Sidak' multiple comparisons test - Compared to DMSO injected	Uninjected	10µM HG bath	10µM HG injected	100µM HG injected
n	14	23	21	21
t	2.183	4.319	5.679	5.598
Statistical Significance	*	****	****	****

Table 3.5 E - Figure 2B

Ordinary Two-way ANOVA			
Alpha	0.05		
Source of Variation	% of total variation	P value	P value summary
Interaction	6.148	0.0141	*
Row Factor	7.061	< 0.0001	****
Column Factor	12.82	< 0.0001	****

Dunnett's multiple comparisons test	**Mean Diff.**	**95% CI of diff.**	**Summary**
Row 1			
uninjected vs. DMSO injected	20.74	-11.26 to 52.75	ns
uninjected vs. 10µM HG bath	26.73	-2.670 to 56.13	ns
uninjected vs. 10µM HG injected	19.4	-9.642 to 48.45	ns
uninjected vs. 100µM HG injected	30.16	-1.169 to 61.50	ns
Row 2			
uninjected vs. DMSO injected	16.16	-14.09 to 46.40	ns
uninjected vs. 10µM HG bath	3.837	-21.83 to 29.50	ns
uninjected vs. 10µM HG injected	16.16	-9.741 to 42.06	ns
uninjected vs. 100µM HG injected	33.6	7.705 to 59.50	**
Row 3			
uninjected vs. DMSO injected	-11.75	-43.08 to 19.59	ns
uninjected vs. 10µM HG bath	13.88	-13.06 to 40.82	ns
uninjected vs. 10µM HG injected	31.76	4.592 to 58.92	*
uninjected vs. 100µM HG injected	35.41	8.246 to 62.57	**
Row 4			
uninjected vs. DMSO injected	-20.06	-52.14 to 12.01	ns

uninjected vs. 10µM HG bath	18.67	-6.998 to 44.33	ns
uninjected vs. 10µM HG injected	33	7.102 to 58.90	**
uninjected vs. 100µM HG injected	32.19	6.286 to 58.09	**

Table 3.6 F - Figure 3A

Unpaired two-tailed t test

P value	< 0.0001
Summary	****
One- or two-tailed P value?	Two-tailed
t, df	t=4.847 df=34.94

Table 3.7 G - Figure 3B

Unpaired two-tailed t test

P value	< 0.0001
Summary	****
One- or two-tailed P value?	Two-tailed
t, df	t=8.731 df=24.89

Table 3.8 H - Figure 3E

Ordinary One-way ANOVA	
DoF	3,51
F	17.6
P	<0.0001
Statistical Significance	****

Bonferroni's multiple comparisons test

	Uninjected vs 100µM HG 9-91-01	Sh WF M356C vs Sh WF M356C + 100µM HG
n1, n2	16,21	8,10
P	<0.0001	<0.0001
Stat sig	****	****

Table 3.9 I - Figure 3F

Unpaired two-tailed t test	
P value	0.5414
Summary	ns
One- or two-tailed P value?	Two-tailed
t, df	t=0.6395 df=7.561

Table 3.10 J- Figure 3G

Unpaired two-tailed t test	
P value	0.0324
Summary	*
One- or two-tailed P value?	Two-tailed
t, df	t=3.637 df=3.183

Table 3.11 K - Figure 3H

Unpaired two-tailed t test	
P value	0.0085
Summary	**
One- or two-tailed P value?	Two-tailed
t, df	t=3.318 df=9.379

Table 3.12 L - Figure 3I

Unpaired two-tailed t test	
P value	0.0011
Summary	**
One- or two-tailed P value?	Two-tailed
t, df	t=4.830 df=8.400

Table 3.13 M - Figure 4B

Ordinary Two-way ANOVA			
Alpha	0.05		
Source of Variation	% of total variation	P value	P value summary
Interaction	3.398	0.0171	*
Row Factor	3.763	0.0009	***
Column Factor	82.38	< 0.0001	****

Tukey's multiple comparisons test	Mean Diff.	95% CI of diff.	Summary
1			
Vegetal vs. Animal	132.2	94.55 to 169.9	****
Vegetal vs. Melanin	133.1	95.45 to 170.8	****
Animal vs. Melanin	0.9	-36.78 to 38.58	ns
2			
Vegetal vs. Animal	98.44	67.67 to 129.2	****
Vegetal vs. Melanin	143.7	112.9 to 174.5	****
Animal vs. Melanin	45.25	14.49 to 76.02	**
3			
Vegetal vs. Animal	98.42	74.59 to 122.2	****
Vegetal vs. Melanin	105.7	70.63 to 140.8	****
Animal vs. Melanin	7.291	-27.79 to 42.37	ns
4			
Vegetal vs. Animal	114.6	76.88 to 152.2	****
Vegetal vs. Melanin	171.7	134.0 to 209.4	****
Animal vs. Melanin	57.15	19.47 to 94.83	**

Table 3.14 N - Figure 5C

Ordinary one-way ANOVA	
DoF	(2,9)
F	74.64
P	<0.0001
Statistical Significance	****

Tukey's multiple comparisons test	Mean Diff.	95% CI of diff.	Summary
Vegetal vs. Animal	132.2	97.21 to 167.2	****
Vegetal vs. Melanin	133.1	98.11 to 168.1	****
Animal vs. Melanin	0.9	-34.11 to 35.91	ns

Table 3.15 O - Figure 5D

Ordinary one-way ANOVA	
DoF	(2,9)
F	47.55
P	<0.0001

Statistical Significance	****

Tukey's multiple comparisons test	Mean Diff.	95% CI of diff.	Summary
Vegetal vs. Animal	114.6	64.48 to 164.6	****
Vegetal vs. Melanin	171.7	121.6 to 221.8	****
Animal vs. Melanin	57.15	7.081 to 107.2	*

Table 3.16 P - Figure 6C

Unpaired two-tailed t test		
P	0.7365	
Summary	ns	
Significantly different? (P < 0.05)	No	
One- or two-tailed P value?	Two-tailed	
t, df	t=0.3444 df=12	

Table 3.17 Q - Figure 6D

Ordinary one-way ANOVA

DoF	(2,11)
F	1.718
P	0.2243
Statistical Significance	ns

Tukey's multiple comparisons test	Mean Diff.	95% CI of diff.	Significant?	Summary
Vegetal vs. Animal	109.5	-353.9 to 572.9	No	ns
Vegetal vs. Melanin	296.9	-140.0 to 733.8	No	ns
Animal vs. Melanin	187.4	-276.0 to 650.9	No	ns

Table 3.18 R - Figure 6E

Ordinary one-way ANOVA	
DoF	(2,11)
F	1.414
P	0.2879
Statistical Significance	ns

Tukey's multiple comparisons test	Mean Diff.	95% CI of diff.	Significant?	Summary
Vegetal vs. Animal	-12.56	-56.63 to 31.51	No	ns
Vegetal vs. Melanin	-25.58	-67.39 to 16.23	No	ns
Animal vs. Melanin	-13.02	-54.83 to 28.79	No	ns

Table 3.19 S - Figure 6F

Ordinary one-way ANOVA	
DoF	(2,11)
F	55.36
P	<0.0001
Statistical Significance	****

Tukey's multiple comparisons test	Mean Diff.	95% CI of diff.	Significant?	Summary
Vegetal vs. Animal	-2.732	-8.677 to 3.213	No	ns
Vegetal vs. Melanin	17.91	12.30 to 23.51	Yes	****
Animal vs. Melanin	20.64	14.70 to 26.59	Yes	****